Analysis, Modeling and Control of Doubly-Fed Induction Generators for Wind Turbines

Andreas Petersson

Department of Electric Power Engineering
CHALMERS UNIVERSITY OF TECHNOLOGY
Göteborg, Sweden 2003

THESIS FOR THE DEGREE OF LICENTIATE OF ENGINEERING

Analysis, Modeling and Control of Doubly-Fed Induction Generators for Wind Turbines

Andreas Petersson

Department of Electric Power Engineering
CHALMERS UNIVERSITY OF TECHNOLOGY
Göteborg, Sweden 2003

Analysis, Modeling and Control of Doubly-Fed Induction Generators for Wind Turbines

Andreas Petersson

Technical report no. 464L
School of Electrical Engineering
Chalmers University of Technology. L
ISSN 1651-4998

Chalmers Bibliotek, Reproservice
Göteborg, Sweden 2003

Analysis, Modeling and Control of Doubly-Fed Induction Generators for Wind Turbines

Andreas Petersson
Department of Electric Power Engineering
Chalmers University of Technology

Abstract

This thesis deals with the analysis, modeling, and control of the doubly-fed induction machine used as a wind turbine generator. The energy efficiency of wind turbine systems equipped with doubly-fed induction generators are compared to other wind turbine generator systems. Moreover, the current control of the doubly-fed induction generator is analyzed and finally the sensitivity of different current controllers with respect to grid disturbances are investigated.

The energy efficiency of a variable-speed wind turbine system using a doubly-fed induction generator is approximately as for a fixed-speed wind turbine equipped with an induction generator. In comparison to a direct-driven permanent-magnet synchronous generator there might be a small gain in the energy efficiency, depending on the average wind-speed at the site. For a variable-speed wind turbine with an induction generator equipped with a full-power inverter, the energy efficiency can be a few percentage units smaller than for a system with a doubly-fed induction generator.

The flux dynamics of the doubly-fed induction machine consist of two poorly damped poles which influence the current controller. These will cause oscillations, with a frequency close to the line frequency, in the flux and in the rotor currents. It has been found that by utilizing a suggested method combining feed-forward compensation and "active resistance", the low-frequency disturbances as well as the oscillations are suppressed better than the other methods evaluated.

The maximum value of the rotor voltage will increase with the size of a voltage dip. This means that it is necessary to design the inverter so it can handle a desired value of a voltage dip. For the investigated systems the maximum rotor voltage and current, due to a voltage dip, can be reduced if the doubly-fed induction machine is magnetized from the stator circuit instead of the rotor circuit. Further, it has been found that the choice of current control method is of greater importance if the bandwidth of the current control loop is low.

Acknowledgements

This work has been carried out at the Department of Electric Power Engineering at Chalmers University of Technology. The financial support provided by the Swedish National Energy Agency is gratefully acknowledged.

I would like thank my supervisor Dr. Torbjörn Thiringer, for help, inspiration, and encouragement, and my main supervisor Prof. Lennart Harnefors, for theoretical help and discussions. Without their help, this work would not be what it is. I would also like to thank my fellow Ph.D. students: Stefan Lundberg, Rolf Ottersten, and Tomáš Petrů for help and discussions regarding my project.

Finally, I would like to thank all the colleagues at the Department of Electric Power Engineering.

Contents

Chapter 1

Introduction

1.1 Background

The Swedish Parliament adopted new energy guidelines in 1997 following the trend of moving towards an ecologically sustainable society. The energy policy decision, states that the objective is to facilitate a change to an ecologically sustainable energy production system. The decision also confirmed that the 1980 and 1991 guidelines still applies, i.e., that the nuclear power production is to be phased out at a slow rate so that the need for electrical energy can be met without risking employment and welfare. The first nuclear reactor of Barsebäck was shut down 30th of November 1999. Nuclear power production shall be replaced by improving the efficiency of electricity use, conversion to renewable forms of energy and other environmentally acceptable electricity production technologies [15]. According to [15] wind power can contribute to fulfilling several of the national environmental quality objectives decided by Parliament in 1991. Continued expansion of wind power is therefore of strategic importance. The Swedish National Energy Agency suggest that the planning objectives for the expansion of wind power should be 10 TWh/year within the next 10–15 years [15]. In Sweden, by end of 2002, there were 328 MW of installed wind power, corresponding to 1 % of the total installed electric power in the Swedish grid [13]. These wind turbines produced 0.6 TWh, corresponding to 0.4 % of the total production of electrical energy in 2002 [17]. In Denmark there were 2.49 TW of installed wind power in 2001, corresponding to 20 % of the total installed electric power in the Danish grid. These Danish wind turbines produced 4 TWh of electrical energy in 2001 [16].

Wind turbines can either operate at fixed speed or variable speed. For a fixed-speed wind turbine the generator is directly connected to the electrical grid. For a variable-speed wind turbine the generator is controlled by power electronic equipment. There are several reasons for using variable-speed operation of wind turbines, among those are possibilities to reduce stresses of the mechanical structure, acoustic noise reduction and the possibility to control active and reactive power [4]. Most of the major wind

turbine manufactures are developing new larger wind turbines in the 3-to-6-MW range [2]. These large wind turbines are all based on variable-speed operation with pitch control using a direct-driven synchronous generator (without gear box) or a doubly-fed induction generator. Fixed-speed induction generators with stall control are regarded as unfeasible [2] for these large wind turbines. Today, variable-slip, i.e., the slip of the induction machine is controlled with external rotor resistances, or doubly-fed induction generators are most commonly used by the wind turbine industry (year 2002) for larger wind turbines [2].

The major advantage of the doubly-fed induction generator, which has made it popular, is that the power electronic equipment only has to handle a fraction (20–30 %) of the total system power [23, 44, 76]. This means that the losses in the power electronic equipment can be reduced in comparison to power electronic equipment that has to handle the total system power as for a direct-driven synchronous generator, apart from the cost saving of using a smaller converter.

1.2 Review of Related Research

According to [5] the energy production can be increased by 2–6 % for a variable-speed wind turbine in comparison to a fixed-speed wind turbine, while in [77] it is stated that the increase in energy can be 39 %. In [45] it is shown that the gain in energy generation of the variable-speed wind turbine compared to the most simple fixed-speed wind turbine can vary between 3–28 % depending on the site conditions and design parameters.

Calculations of the energy efficiency of the doubly-fed induction generator system, has been presented in several papers, for instance [35, 53, 63]. A comparison to other electrical systems for wind turbines are, however, harder to find. One exception is in [9], where Datta et al. have made a comparison of the energy capture for different schemes of the electrical configuration, i.e., fixed-speed wind turbine using an induction generator, full variable-speed wind turbine using an inverter-fed induction generator, and a variable-speed wind turbine using an doubly-fed induction generator. According to [9] the energy capture can be significantly enhanced by using a doubly-fed induction machine as a generator and the increased energy capture of a doubly-fed induction generator by over 20 % with respect to a variable-speed system using a cage rotor induction machine and by over 60 % in comparison to a fixed-speed system. Aspects such as the wind distribution, electrical and mechanical losses of the systems were neglected in that study.

Control of the doubly-fed induction machine is more complicated than the control of a standard induction machine and has all the limitations that the line-fed synchronous generator has, e.g., starting problem, synchronization and oscillatory transients [42].

Wang et al. [72] have by simulations found that the flux is influenced both by load changes and stator power supply variations. The flux response is a damped oscillation and the flux and rotor current oscillate more severely when the speed is increasing compared to when the speed is decreasing. Heller et al. [29] have investigated the stability of the doubly-fed induction machine mathematically. They have shown that the dynamics of the doubly-fed induction machine have poorly damped eigenvalues with a corresponding natural frequency near the line frequency and that the system is unstable for certain operation conditions. These poorly damped poles will influence the current through the back emf. However, it has not been found in the literature any evaluation of the performance of different current control laws with respect to eliminating the influence of the back emf in the rotor current.

The flux oscillations can be damped in some different ways. One method is to reduce the bandwidth of the current controllers [29]. Wang et al. [72] have introduced a flux differentiation compensation that improves the damping of the flux. Kelber et al. [38] have used another possibility; to use an extra inverter that substitutes the star point of the stator winding, i.e., an extra degree of freedom is introduced that can be used to actively damp out the flux oscillations. Kelber has in [37] made a comparison of different methods of damping the flux oscillations. It was found, in the reference, that the methods with a flux differentiation compensation and the method with an extra inverter manage to damp out the oscillations best.

The response of the doubly-fed induction machine to grid disturbances, is a subject rarely treated in the literature. One exception is Kelber in [37]. Kelber concluded that it is necessary to actively damp the flux oscillations either with a flux differentiation compensation or use an extra inverter in the star point of the stator winding. However, Kelber has mainly focused on the "quality" of the damping and how fast a grid disturbance is damped out for different types of flux dampers. But, how the magnitude of the currents in the rotor circuit depends on aspects such as the bandwidth of the current control loop and the size of the grid disturbances was not presented. The magnitude of the rotor current due to a grid disturbance is of importance since the magnitude must not exceed the rated value of the inverter. If the magnitude of the rotor current reaches the rated value, a "crow-bar" must short-circuit the rotor circuit in order to protect the inverter.

1.3 Contributions

The contribution of this thesis are:

- An energy efficiency comparison of electrical systems for wind turbines is presented in Chapter 3. The investigated systems are one fixed-speed induction generator system and three variable-speed systems. The variable-speed systems are: a doubly-fed induction generator, an induction generator (with a full-power

inverter) and a direct-driven permanent-magnet synchronous generator system. Important electrical and mechanical losses of the systems are included in the study.

- Analysis of the performance of different current controllers for the doubly-fed induction generator, is presented in Section 6.1. Further, the influence of the back emf on the rotor current for the different current controllers are investigated. Finally, the obtained results are verified by measurements.

- Investigation of the ability of the doubly-fed induction machine to withstand disturbances in the electrical grid, i.e., the maximum rotor current and voltage due to a voltage dip are simulated. Aspects such as the current control method, the bandwidth of the current control loop and the dip are included in the investigation. This is presented in Section 6.4.

1.4 Outline

This thesis is organized as follows:

Chapter 2 Description of properties of the wind and how the wind is transformed to mechanical power. Finally, different wind turbine concepts are described.

Chapter 3 A theoretical investigation of the energy efficiency for the electrical systems of a wind turbine with a doubly-fed induction generator compared others is presented.

Chapter 4 Presentation of steady-state induction machine models. Further, the operational profile (speed–torque characteristics) of the induction machine and how it is possible to affect its characteristic is presented.

Chapter 5 In this chapter, dynamic model and control aspects of the induction machine is presented. Vector control of the doubly-fed induction machine is more thoroughly described.

Chapter 6 Analysis of the performance of different current controllers for the doubly-fed induction generator. Further, investigation of the response of the doubly-fed induction machine to grid disturbances.

Chapter 7 The conclusion is presented.

Chapter 8 The proposed future work is presented.

Chapter 2

Wind Turbines

This chapter serves as a tutorial, where properties of the wind, aerodynamic conversion and different wind turbine concepts are described. The purpose is to describe the theory and concepts that will be used later on and to introduce the reader not acquainted with the subject. The interested reader can find more information in, for example, [4, 36].

2.1 Properties of the Wind

In this section the properties of the wind, which are of interest in this thesis, will be described. First the wind distribution, i.e., the probability of a certain average wind speed, will be presented. The wind distribution can be used to determine the expected value of certain quantities, e.g. produced power. In order to simulate the rapid continuous changes in the wind speed, i.e., turbulence, a model employing power spectral density will be used.

2.1.1 Wind Distribution

The annual average wind speed is an extremely important factor for the output power of a wind turbine. The average wind speed on a shorter time basis is, apart from the annual wind speed, also dependent on the distribution. It has been found that the wind distribution can be described by the Weibull probability density function [36]. The Weibull distribution is described by the following probability density function

$$f(w) = \frac{k}{c}\Big(\frac{w}{c}\Big)^{k-1} \mathrm{e}^{-(w/c)^k} \tag{2.1}$$

where k is a shape parameter, c is a scale parameter, and w is the wind speed. Thus, the average wind speed (or the expected wind speed) can be calculated from

$$w_{\text{ave}} = \int_0^\infty w f(w) \mathrm{d}w = \frac{c}{k}\Gamma\Big(\frac{1}{k}\Big) \tag{2.2}$$

where Γ is Euler's gamma function, i.e.,

$$\Gamma(z) = \int_0^\infty t^{z-1}\mathrm{e}^{-t}\mathrm{d}t. \tag{2.3}$$

If the shape parameter equals 2 in the Weibull distribution it is known as the Rayleigh distribution. (The advantage of using the Rayleigh distribution is that it only depends on the average wind speed.) In Figure 2.1 the wind speed probability density function of the Rayleigh distribution is plotted. The average wind speeds in Figure 2.1 are

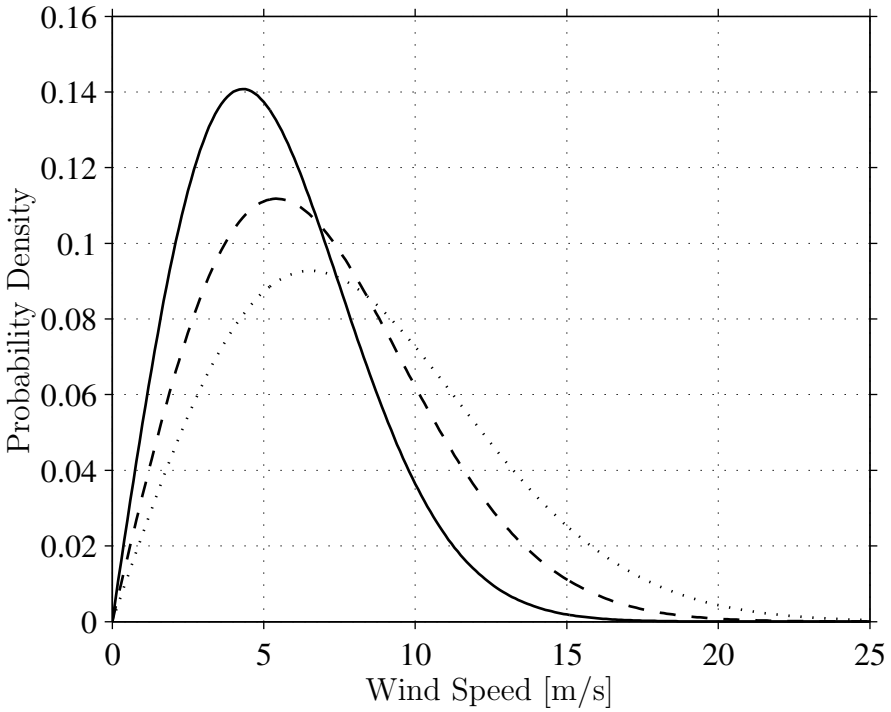

Figure 2.1: Probability density of the Rayleigh distribution. The average wind speeds are 5.4 m/s (solid), 6.8 m/s (dashed) and 8.2 m/s (dotted).

5.4 m/s, 6.8 m/s, and 8.2 m/s. A wind speed of 5.4 m/s corresponds to a medium wind site in Sweden, according to [64], while 8–9 m/s are wind speeds available at sites located outside the Danish west coast [34]. For the Rayleigh distribution, the scale factor, c, given the average wind speed can be found from (k=2, and $\Gamma(\frac{1}{2}) = \sqrt{\pi}$)

$$c = \frac{2}{\sqrt{\pi}} w_{\text{ave}}. \tag{2.4}$$

2.1.2 Wind Simulation

On a very short time basis, from minutes down to fraction of seconds, the wind varies continuously, which is called turbulence. To be able to calculate the wind speed at the wind turbine, a model of the turbulence power spectral density is thus needed. One commonly used spectral density function is the Kaimal spectral density function [69]

$$S(f) = \left(\frac{0.4}{\ln(z/z_0)}\right)^2 \frac{105 z w_0}{\left(1 + \frac{33fz}{w_0}\right)^{5/3}} \tag{2.5}$$

where S is the single-sided longitudinal velocity component spectrum, f is the frequency, z is height above ground, z_0 is the surface roughness coefficient, and w_0 is

the average wind velocity at hub height. It is possible to use other turbulence power spectral densities as well, such as the Frost and the von Karman Spectrum [69]. The wind speed also varies in space, so different blades and blade segments are passed by slightly different wind speeds at each time instant. In [69] a method (the "Sandia" method) for calculating a 3D wind field, suitable for horizontal axis wind turbines, is presented and in [74] it is described how to generate the wind field with a minimum of computation.

2.2 Aerodynamic Conversion

The air flow over a stationary airfoil causes a lift force, F_L, and a drag force, F_D. The lift force is perpendicular to the direction of the air flow and the drag force is in the direction of the air flow. If the airfoil moves in the direction of the lift force, the relative wind direction (or the effective direction of the air flow) has to be taken into account. The pitch angle, β, is the angle between the chord line of the blade and the plane of rotation. The angle of attack, κ, is the angle between the chord line of the blade and the relative wind direction [36]. See Figure 2.2 for an illustration of the angles. If

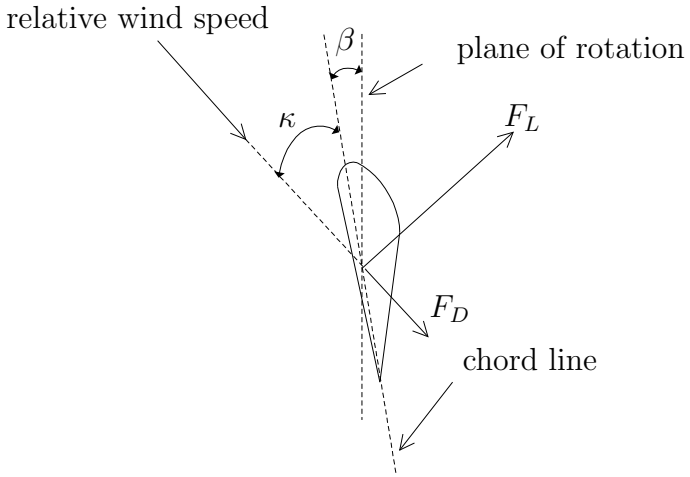

Figure 2.2: Definition of the pitch angle, β, and angle of attack, κ.

the angle of attack exceeds a certain value, a wake is created above the airfoil which reduces the lift force and increases the drag force. Then the air flow around the airfoil has stalled [4]. The incremental lift and drag force can be found from [61]

$$dF_L = \frac{1}{2}\rho C_L c w_{\text{rel}}^2 d\chi \tag{2.6}$$

$$dF_D = \frac{1}{2}\rho C_D c w_{\text{rel}}^2 d\chi \tag{2.7}$$

where ρ is density of the air, C_L is the lift coefficient, C_D is the drag coefficient, c is the chord length of the airfoil section, w_{rel} is the relative wind speed and $d\chi$ is the

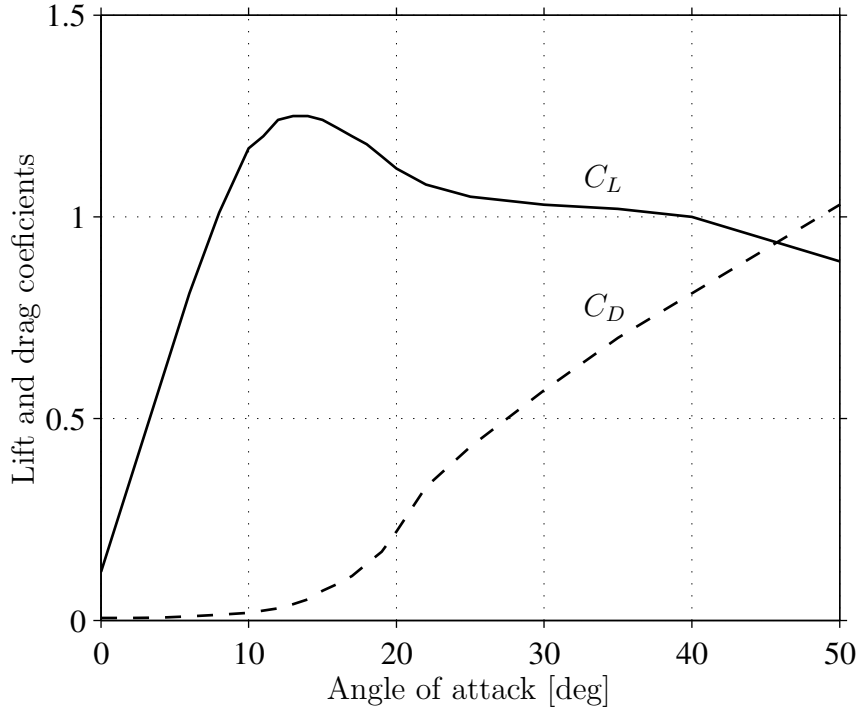

Figure 2.3: Lift, C_L, and drag coefficient, C_D, as a function of the angle of attack, κ.

increment of the span length. The lift and drag coefficients are given as functions of the angle of attack. See Figure 2.3 for an example of typical lift and drag coefficients.

Normally the power extracted from the wind is given as a fraction of the total power in the wind. The fraction is described by a coefficient of performance, C_p, [36]. This method will be described in a following section. The coefficient of performance can either be determined theoretically using blade element momentum theory or C_p can also be determined from measurements [4].

2.2.1 Aerodynamic Power Control

At high wind speeds it is necessary to limit the input power to the turbine, i.e., aerodynamic power control. There are three major ways of performing the aerodynamic power control, i.e., by stall, pitch or active stall control. Stall control implies that the blades are designed to stall in high wind speeds and no pitch mechanism is thus required [4].

Pitch control is the most common method of controlling the aerodynamic power generated by a turbine rotor, for newer larger wind turbines. Pitch control is used by almost all variable-speed wind turbines. Below rated wind speed the turbine should produce as much power as possible, i.e., using a pitch angle that maximizes the energy capture. Above rated wind speed the pitch angle is controlled in such a way that the aerodynamic power is at its rated [4]. In order to limit the aerodynamic power, at high wind speeds, the pitch angle is controlled to decrease the angle of attack. See Figure 2.2 for an illustration of the angle of attack. It is also possible to increase the

angle of attack towards stall in order to limit the aerodynamic power. This method can be used to fine tune the power level at high wind speeds for fixed-speed turbines. This control method is known as *active stall* or *combi stall* [4].

2.2.2 $C_p(\lambda)$ Curve

A method that is often used for steady-state calculations of the mechanical power from a wind turbine is the so-called $C_p(\lambda)$ curve. Then the mechanical power, P_{mech}, can be determined by [36]

$$P_{\text{mech}} = \frac{1}{2}\rho A_r C_p(\lambda, \beta) w^3 \tag{2.8}$$

$$\lambda = \frac{\Omega_{rT} r_r}{w} \tag{2.9}$$

where C_p is the coefficient of performance, β is the pitch angle, λ is the tip-speed ratio, w is the wind speed, Ω_{rT} is the rotor speed (on the low-speed side of the gear box), r_r is the rotor plane radius, ρ is the air density and A_r is the area swept by the rotor. In Figure 2.4 an example of a $C_p(\lambda)$ curve and the shaft power as a function of the wind speed for rated rotor speed can be seen.

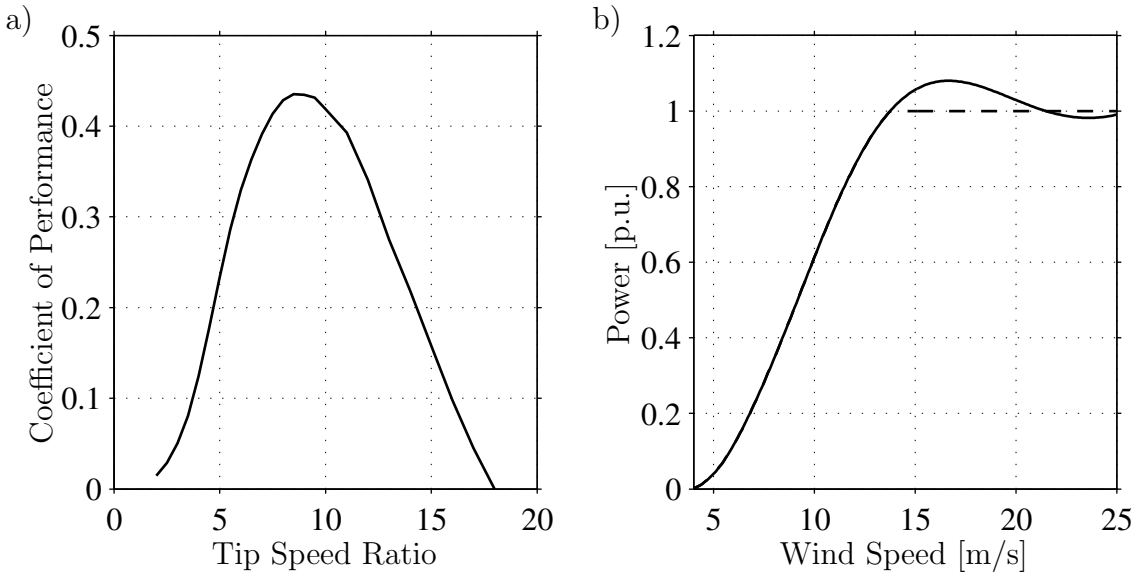

Figure 2.4: a) The coefficient of performance, C_p, as a function of the tip speed ratio, λ. b) Mechanical power as a function of wind speed at rated rotor speed (solid line is fixed pitch angle, i.e., stall control and dashed line is active stall).

Figure 2.5 shows an example of how the mechanical power, derived from the $C_p(\lambda)$ curve, and the rotor speed vary with the wind speed for a variable-speed wind turbine. The rotor speed in the variable-speed area is controlled in order to keep the optimal tip speed ratio, λ, i.e., C_p is kept at maximum as long as the power or rotor speed is below its rated values. As mentioned before, the pitch angle is at higher wind speeds

controlled in order to limit the input power to the wind turbine, when the turbine has reached the rated power. As can be seen in Figure 2.5b) the turbine, in this example,

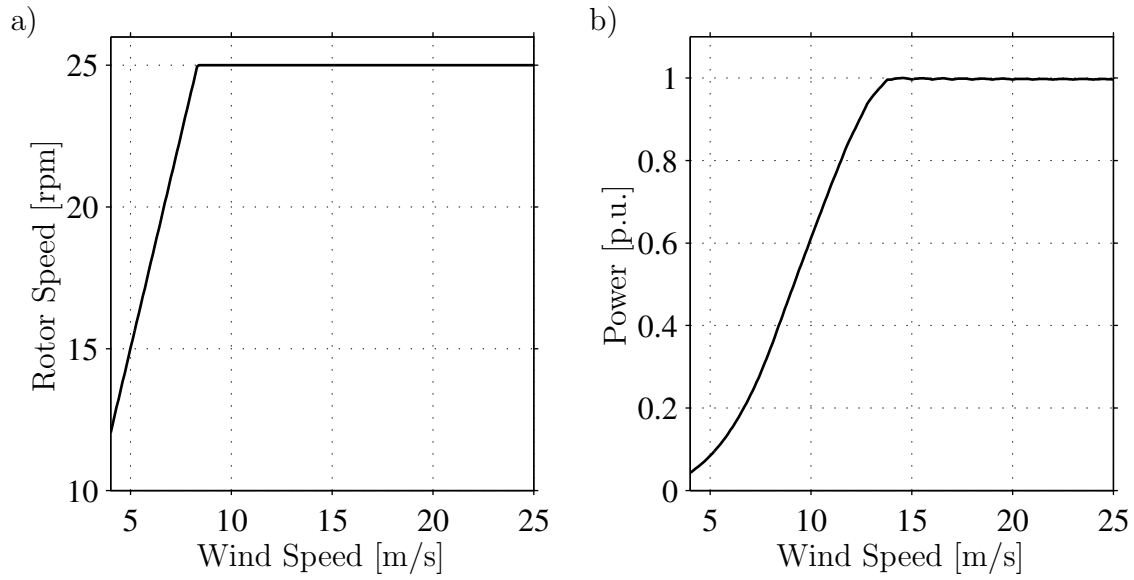

Figure 2.5: Typical characteristic for a variable-speed wind turbine. a) Rotor speed as a function of wind speed. b) Mechanical power as a function of wind speed.

reaches the rated power, 1 p.u., at a wind speed of approximately 13 m/s. It is possible to optimize the radius of the wind turbines rotor to suit sites with different average wind speeds. For example, if the rotor radius, r_r, is increased, the output power of the turbine is also increased, according to (2.8). This implies that the nominal power, 1 p.u., will be reached for a lower wind speed, referred to Figure 2.5b). However, increasing the rotor radius implies that for higher wind speed the output power must be even more limited, e.g., by pitch control, so that the nominal power of the generator is not exceeded. Therefore, there is a trade-off between the rotor radius and the nominal power of the generator. This choice is to a high extent dependent on the average wind speed of the site.

2.3 Wind Turbine Concepts

Wind turbines can operate with either fixed speed (actually within a speed range about 1 %) or variable speed. For fixed-speed wind turbines, the generator (induction generator) is directly connected to the grid. Since the speed is almost fixed to the grid frequency, and most certainly not controllable, it is not possible to store the turbulence of the wind in form of rotational energy. Therefore, for a fixed-speed system the turbulence of the wind will result in power variations, and thus affect the power quality of the grid [48]. For a variable-speed wind turbine the generator is controlled by power electronic equipment, which makes it possible to control the rotor speed. In this way the power fluctuations caused by wind variations can be more or less absorbed

by changing the rotor speed [52] and thus power variations originating from the wind conversion and the drive train can be reduced. Hence, the power quality impact caused by the wind turbine can be improved compared to a fixed-speed turbine [41].

The rotational speed, Ω_{rT}, of a wind turbine is fairly low and must therefore be adjusted to the electrical frequency. This can be done in two ways, i.e., with a gear box or with the number of poles, n_p, of the generator. The number of poles sets the mechanical speed, ω_m, of the generator with respect to the electrical frequency. If the gear ratio equals gr, the rotor speed of the wind turbine is adjusted to the electrical frequency as

$$\omega_{rT} = \frac{\Omega_{rT}}{n_p gr} \tag{2.10}$$

where ω_{rT} is referred to the electrical frequency of the grid. The dynamics of the drive train can be expressed as

$$J_T \frac{\mathrm{d}\Omega_{rT}}{\mathrm{d}t} = T_s - T_T \tag{2.11}$$

$$J \frac{\mathrm{d}\omega_m}{\mathrm{d}t} = T_e - T_s \tag{2.12}$$

where J_T is the wind-turbine inertia, J is the generator inertia, T_s is the shaft torque, T_T is the torque produced by the wind turbine rotor and T_e is the electromechanical torque produced by the generator. It is most often convenient to have the rotational speeds referred to same side of the gear box as

$$J_T \frac{\mathrm{d}\Omega_{rT}}{\mathrm{d}t} = \frac{J_T}{n_p gr} \frac{\mathrm{d}\omega_{rT}}{\mathrm{d}t} = \xi(\theta_r - \theta_{rT}) + \zeta(\omega_r - \omega_{rT}) - T_T \tag{2.13}$$

$$J \frac{\mathrm{d}\omega_m}{\mathrm{d}t} = \frac{J}{n_p} \frac{\mathrm{d}\omega_r}{\mathrm{d}t} = T_e - \xi(\theta_r - \theta_{rT}) - \zeta(\omega_r - \omega_{rT}) \tag{2.14}$$

where ω_r is the rotational speed of the generator referred to the electrical frequency and the shaft torque has been set to $T_s = \xi(\theta_r - \theta_{rT}) + \zeta(\omega_r - \omega_{rT})$, where ξ is the shaft stiffness and ζ is the shaft dampening. The angles θ_{rT} and θ_r can be found from

$$\frac{\mathrm{d}\theta_{rT}}{\mathrm{d}t} = \omega_{rT} \qquad \frac{\mathrm{d}\theta_r}{\mathrm{d}t} = \omega_r. \tag{2.15}$$

In this section the following wind turbine concepts will be presented:

1. Fixed-speed wind turbine with an induction generator.
2. Variable-speed wind turbine equipped with a cage-bar induction generator or synchronous generator.
3. Variable-speed wind turbine equipped with multiple-pole synchronous machine or multiple-pole permanent-magnet synchronous generator.
4. Variable-speed wind turbine equipped with an doubly-fed induction generator.

There are also some other concepts, a description of these can be found in [23].

2.3.1 Fixed-Speed System

For the fixed-speed wind turbine the induction generator is directly connected to the electrical grid according to Figure 2.6. The rotor speed of the fixed-speed wind turbine

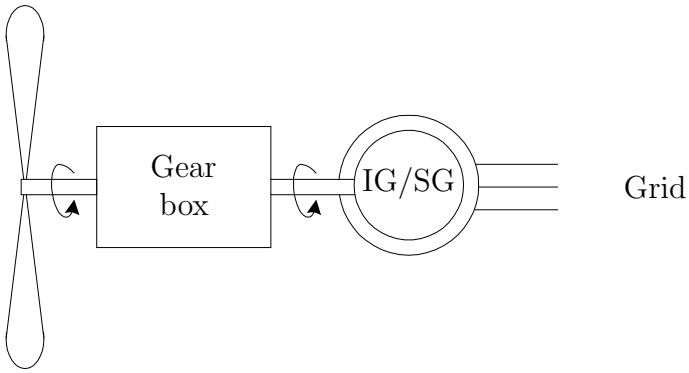

Figure 2.6: Fixed-speed generator system.

is adjusted by a gear box and the pole-pair number of the generator. The fixed-speed wind turbine system is often equipped with two induction generators, one for low wind speeds (with lower synchronous speed) and one for high wind speeds. This was the "conventional" concept used by many Danish manufacturers in the 1980s and 1990s [23].

2.3.2 Full Variable-Speed System

The system presented in Figure 2.7 consists of a wind turbine equipped with an inverter connected to the stator of the generator. The generator could either be a singly-fed induction generator or a synchronous generator. The gear box is designed so that maximum rotor speed corresponds to rated speed of the generator. Since this full-

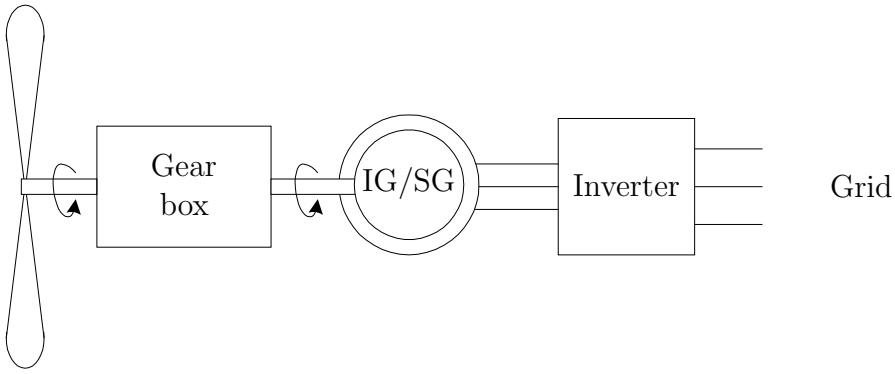

Figure 2.7: Variable-speed generator system.

power converter system is commonly used for other applications, one advantage with this system is its well-developed and robust control [3, 25, 42].

2.3.3 Full Variable-Speed System with a Multiple-Pole Generator

Synchronous generators or permanent-magnet synchronous generators can be designed with multiple poles which implies that there is no need for a gear box, see Figure 2.8. For the permanent-magnet synchronous generator a major advantage is its

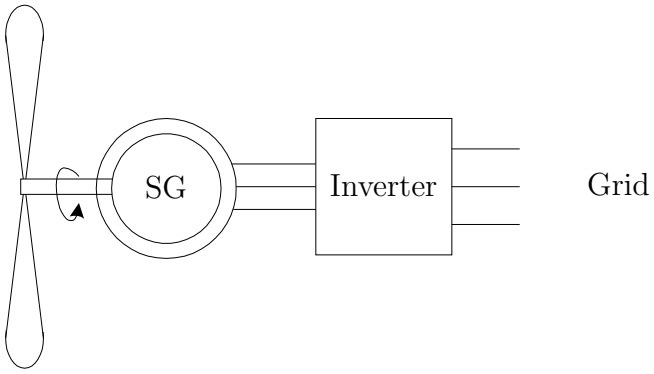

Figure 2.8: Variable-speed multiple-pole generator system.

well-developed and robust control [3, 25, 42]. A synchronous generator with multiple poles as a wind turbine generator is successfully manufactured by Enercon [14].

2.3.4 Limited Variable-Speed System

This system, see Figure 2.9, consists of a wind turbine with a variable-speed constant-frequency induction generator (doubly-fed induction generator). This means that the stator is directly connected to the grid while the rotor winding is connected via slip rings to an inverter. The inverter is designed so that the induction generator can operate

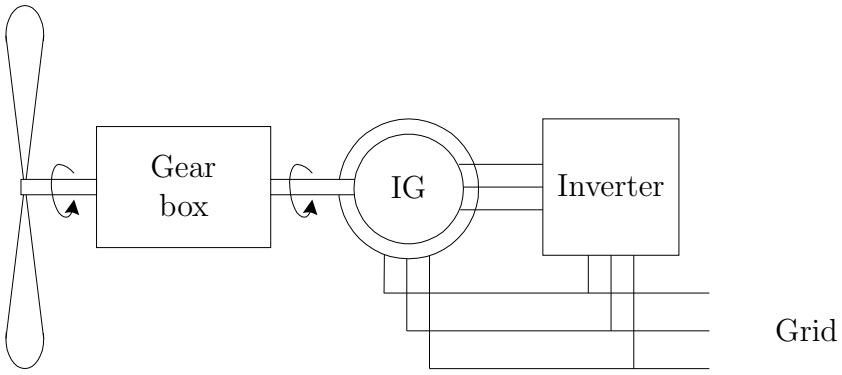

Figure 2.9: Variable-speed doubly-fed induction generator system.

in a limited variable-speed range. The gear-box ratio is set so that the nominal speed of the induction generator corresponds to the middle value of the rotor-speed range of the wind turbine. This is done in order to minimize the size of the inverter, which will vary with the rotor-speed range. With this inverter it is possible to control the

speed (or the torque) and also the reactive power on the stator side of the induction generator.

The transformer between the inverter and rotor circuit in Figure 2.10 is to indicate and highlight the stator-to-rotor turns ratio. The stator-to-rotor turns ratio can be designed so that maximum voltage of the inverter corresponds to the desired maximum rotor voltage which in principle appear as the highest desirable slip (with a safety margin). The reason is that it is possible to use a smaller converter and in this way the converter losses can be reduced, in addition to the investment cost. The transformer can be treated as ideal since it is actually a part of the induction generator itself. For

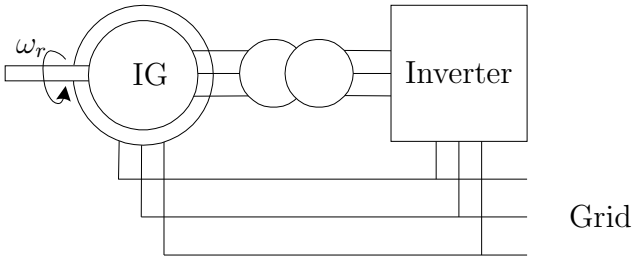

Figure 2.10: Doubly-fed induction generator system.

this system the speed range, i.e., the slip, is approximately determined by the ratio between the windings of the stator and the rotor. Another possibility is to use a higher stator voltage compared to the rotor to gain the same effect as the stator-to-rotor turns ratio. For example, a stator voltage of 2.8 kV and a maximum rotor voltage of 690 V corresponds to a stator voltage of 690 V and a stator-to-rotor turns ratio of 1:4, see Figure 2.11.

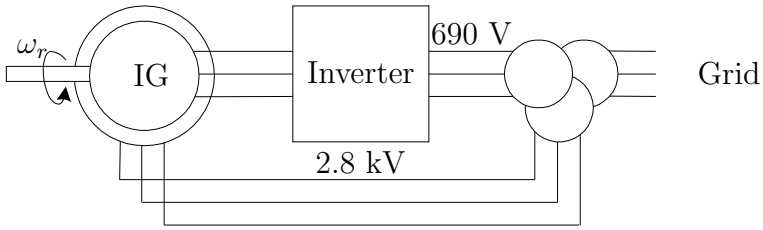

Figure 2.11: Example of increased stator voltage.

There is a variant of the doubly-fed induction generator method which uses external rotor resistances, which can be controlled. Some of the drawbacks of this method are that it is not possible to decrease the rotor speed below synchronous speed, energy is unnecessary dissipated in the external rotor resistances and that there is no possibility to control the reactive power.

Manufacturers, that produces wind turbines with the doubly-fed induction machine as generator are, for example, DeWind, GE Wind Energy, Nordex, and Vestas [12, 19, 46, 70].

Chapter 3

Energy Efficiency Comparison of Electrical Systems for Wind Turbines

In the energy efficiency comparison, in this chapter, the following systems described in Chapter 2 will be investigated.

- Fixed-speed wind turbine equipped with one or two induction generators (IG). For the fixed-speed system using two generators, one generator is used for low wind speeds (with lower synchronous speed) and the other is used for medium and high wind speeds. This system is referred to as the *fixed-speed system*.
- Variable-speed wind turbine equipped with a doubly-fed induction generator (DFIG). The gear-box ratio is set so that the nominal speed of the induction generator corresponds to the middle value of the rotor-speed range of the wind turbine. This system is referred to as the *DFIG system*.
- Variable-speed wind turbine equipped with an full-power inverter connected to the stator of the induction generator (IG). For this system the gear-box ratio is designed so that the synchronous speed of the generator corresponds to the maximum speed of the turbine. This system is referred to as the *variable-speed IG system*.
- Variable-speed wind turbine equipped with an inverter connected to the stator of a multiple-pole permanent-magnet synchronous generator (PMSG). Since this system is equipped multiple-pole generator, there is no need for a gear box. This system is referred to as the *PMSG system*.

It is assumed that there exists a pitch mechanism in all of the wind-turbine systems.

Datta et al. [9] have made a comparison of the produced electrical energy for different schemes of the electrical configuration, i.e., fixed-speed system, variable-speed

IG system, and a DFIG system. In [9], the mechanical and electrical losses of the system are neglected, but will not be neglected in this chapter. The calculated produced electrical energy in [9] is based on a 10-minute-long constructed wind speed (with an average value of 10 m/s), while here the losses of the system are calculated for all wind speeds and then normalized using the wind-speed distribution. According to [9], the produced energy can be significantly enhanced by using a DFIG system, i.e., by over 20 % with respect to a variable speed IG system. Most probably, the reason for this is the fact that the generator in the variable-speed IG system is running in the field-weakening region for high wind speeds. Since the mechanical and electrical losses of the system are neglected in [9], a proper design of the gear-box ratio would (most probably) strongly have reduced this large amount of increase of produced electrical energy.

In [22], Grauers thoroughly described and analyzed the losses of permanent-magnet synchronous generators for a wind-turbine application. This will be used later on in this section.

The rotor-speed range and the stator-to-rotor turns ratio of the induction generator are important aspects that will be studied. As described in Chapter 2 the same effect as the stator-to-rotor turns ratio can be accomplished with having a higher stator voltage than the maximum rotor voltage. However, in this section, only the stator-to-rotor turns ratio will be used and not the possibility to having a higher stator voltage than the rotor voltage. As pointed out in Chapter 2 it is possible to optimize the rotor radius of the wind turbine with respect to the size of the generator and the average wind speed. Since the main objective, in this study, is to study the drive train and energy capture given the same rotor, such an optimization is not performed here. If the rotor size with respect to the generator size would be maximized, this would affect all three wind turbines in almost the same way. Another possibility to increase the energy capture is to increase the rotational speed of the wind turbine [45]. This requires, off course that the blades are re-designed. Moreover, this would lead to increased noise emission. The turbulence has a small influence on the result [45]. The influence of the turbulence has been neglected in this study.

Some of the material presented in this section has been published in [51].

3.1 Losses of the System Components

This section describes how the losses of the different components of the wind turbine systems are calculated.

3.1.1 Induction Generator

For the static modeling of the induction generator, the equivalent circuit has been used, as described in Section 4.1. The losses of the induction generator can be found from (4.6). Variations in the magnetizing resistance, R_m, due to applied stator voltage and frequency have been neglected.

For the induction generators used in this section, operated at 690 V, 50 Hz, the parameters are:

1 MW: $R_s = 3.1$ mΩ, $R_r = 4.6$ mΩ, $R_m = 85\ \Omega$, $L_{s\lambda} = 0.15$ mH, $L_{r\lambda} = 0.15$ mH, $L_m = 7$ mH, and $n_p = 2$.

0.4 MW: $R_s = 4.0$ mΩ, $R_r = 1.0$ mΩ, $R_m = 200\ \Omega$, $L_{s\lambda} = 0.41$ mH, $L_{r\lambda} = 0.14$ mH, $L_m = 12$ mH, and $n_p = 3$.

3.1.2 Inverter

In order to be able to feed the induction generator from a variable voltage and frequency source, the induction generator can be connected to a pulse-width modulated (PWM) inverter. In Figure 3.1, an equivalent circuit of the inverter is drawn, where each transistor, T1 to T6, is equipped with a reverse (free-wheeling) diode. A PWM circuit switches on and off the transistors. The duty cycle of the transistor and the diode determines whether the transistor or a diode is conducting in a transistor leg (e.g., T1 and T4).

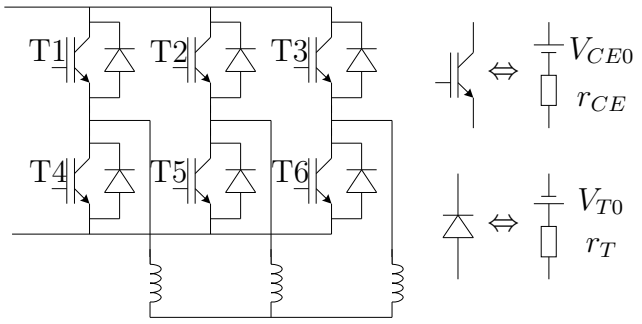

Figure 3.1: Inverter scheme.

The losses of the inverter can be divided into switching losses and conducting losses. The switching losses of the transistors are the turn-on and turn-off losses. For the diode, the switching losses mainly consist of turn-off losses [67], i.e. reverse-recovery energy. The turn-on and turn-off losses for the transistor and the reverse-recovery energy loss for a diode can be found from data sheets. The conducting losses arise from the current through the transistors and diodes. The transistor and the diode can be modeled as constant voltage drops, V_{CE0} and V_{T0}, and a resistance in series, r_{CE} and r_T, see Figure 3.1. Simplified expressions of the transistor's and diode's conducting losses, for

a transistor leg, are (with a third harmonic voltage injection) [1]

$$P_{\mathrm{c,T}} = \frac{V_{CE0} I_{\mathrm{rms}} \sqrt{2}}{\pi} + \frac{I_{\mathrm{rms}} V_{CE0} m_i \cos(\phi)}{\sqrt{6}} + \frac{r_{CE} I_{\mathrm{rms}}^2}{2} + \frac{r_{CE} I_{\mathrm{rms}}^2 m_i}{\sqrt{3}\cos(\phi) 6\pi} - \frac{4 r_{CE} I_{\mathrm{rms}}^2 m_i \cos(\phi)}{45\pi\sqrt{3}} \tag{3.1}$$

$$P_{\mathrm{c,D}} = \frac{V_{T0} I_{\mathrm{rms}} \sqrt{2}}{\pi} - \frac{I_{\mathrm{rms}} V_{T0} m_i \cos(\phi)}{\sqrt{6}} + \frac{r_T I_{\mathrm{rms}}^2}{2} - \frac{r_T I_{\mathrm{rms}}^2 m_i}{\sqrt{3}\cos(\phi) 6\pi} + \frac{4 r_T I_{\mathrm{rms}}^2 m_i \cos(\phi)}{45\pi\sqrt{3}} \tag{3.2}$$

where I_{rms} is the root mean square (RMS) value of the (sinusoidal) current to the grid or the generator, m_i is the modulation index, and ϕ is the phase shift between the voltage and the current.

Since, for the values in this paper [56, 57, 58] (see Table 3.1 for actual values), $r = r_{CE} \approx r_T$ and $V = V_{CEO} \approx V_{TO}$, it is possible to model the transistor and the diode with the same model. The conduction losses can, with the above mentioned approximation, be expressed as

$$P_{\mathrm{c}} = P_{\mathrm{c,T}} + P_{\mathrm{c,D}} = \frac{2\sqrt{2} V I_{\mathrm{rms}}}{\pi} + r I_{\mathrm{rms}}^2. \tag{3.3}$$

A reasonable assumption is that the switching losses of the transistor is proportional to the current [1]. This implies that the switching losses from the transistor and the inverse diode can be expressed as

$$P_{\mathrm{s,T}} = (E_{\mathrm{on}} + E_{\mathrm{off}}) \frac{\frac{2}{\pi}\sqrt{2} I_{\mathrm{rms}}}{I_{C,\mathrm{nom}}} f_{sw} \tag{3.4}$$

$$P_{\mathrm{s,D}} = E_{rr} f_{sw} \tag{3.5}$$

where E_{on} and E_{off} is the turn-on and turn-off energy losses respectively, for the transistor, E_{rr} is the reverse recovery energy for the diode, and $I_{C,\mathrm{nom}}$ is the nominal current through the transistor. The total losses in the three transistor legs of the inverter become

$$P_{\mathrm{loss}} = 3(P_{\mathrm{c}} + P_{\mathrm{s,T}} + P_{\mathrm{s,D}}). \tag{3.6}$$

The back-to-back inverter can be seen as two inverters which are connected together: the machine-side inverter (MSI), and the grid-side inverter (GSI). For the MSI the current through the valves, I_{rms}, are the stator current for the variable-speed IG system or the rotor current for the DFIG system. One way of calculating I_{rms} for the GSI is to use the current that produces the active power in the machine, adjusted with the ratio between machine-side voltage and the grid voltage. The reactive current is assumed to be stored in the dc-link capacitor. Thus, it is now possible to calculate the losses of the back-to-back inverter as

$$P_{\mathrm{loss,inverter}} = P_{\mathrm{loss,GSI}} + P_{\mathrm{loss,MSI}}. \tag{3.7}$$

In this section the switching frequency is set to 5 kHz.

Table 3.1: Inverter Data.

Inverter Characteristics 1 (IGBT and inverse diode)		
Nominal current	$I_{C,\text{nom}}$	1200 A
Operating dc-link voltage	V_{CC}	1000 V
	V_{CEO}	1.2 V
Lead resistance (IGBT)	r_{CE}	0.8 mΩ
Turn-on and turn-off energy (IGBT)	$E_{\text{on}} + E_{\text{off}}$	733 mJ
	V_{TO}	1.2 V
Lead resistance (diode)	r_T	0.7 mΩ
Reverse recovery energy (diode)	E_{rr}	163 mJ
Inverter Characteristics 2 (IGBT and inverse diode)		
Nominal current	$I_{C,\text{nom}}$	600 A
Operating dc-link voltage	V_{CC}	1000 V
	V_{CEO}	1.2 V
Lead resistance (IGBT)	r_{CE}	1.6 mΩ
Turn-on and turn-off energy (IGBT)	$E_{\text{on}} + E_{\text{off}}$	367 mJ
	V_{TO}	1.2 V
Lead resistance (diode)	r_T	1.3 mΩ
Reverse recovery energy (diode)	E_{rr}	81.3 mJ
Inverter Characteristics 3 (IGBT and inverse diode)		
Nominal current	$I_{C,\text{nom}}$	300 A
Operating dc-link voltage	V_{CC}	1000 V
	V_{CEO}	1.2 V
Lead resistance (IGBT)	r_{CE}	3.1 mΩ
Turn-on and turn-off energy (IGBT)	$E_{\text{on}} + E_{\text{off}}$	183 mJ
	V_{TO}	1.2 V
Lead resistance (diode)	r_T	2.7 mΩ
Reverse recovery energy (diode)	E_{rr}	40 mJ

3.1.3 Gear-Box Losses

In [21] the gear-box losses, $P_{\text{loss,GB}}$, are estimated according to

$$P_{\text{loss,GB}} = \eta P_{\text{lowspeed}} + \xi P_n \frac{\Omega_r}{\Omega_{rn}} \tag{3.8}$$

where η is the gear-mesh losses constant and ξ is a friction constant. According to [22], for a 1-MW gear box, the constants $\eta = 0.02$ and $\xi = 0.005$ are reasonable.

3.1.4 Total System Losses

When calculating the losses for the system we will take into account the IG losses, gear-box losses, as well as machine-side and grid-side inverter losses. The total system losses become

$$P_{\text{loss}} = P_{\text{loss,GB}} + P_{\text{loss,IG}} + P_{\text{loss,GSI}} + P_{\text{loss,MSI}} \tag{3.9}$$

where $P_{\text{loss,IG}}$ are the losses of the IG. The losses of the slip-rings for the DFIG-system, friction loses of the IG are neglected.

The average value (or expected value) of the produced power, during a year, for a wind turbine can be found from

$$P_{\text{ave}} = \int_0^\infty P(w) f(w) \mathrm{d}w \tag{3.10}$$

where $f(w)$ is the probability density function. The Rayleigh distribution will be used here, see also Section 2.1.1.

3.2 Fixed-Speed System

Steady-state calculations will be carried out in this section in order to determine the losses of the fixed-speed systems, according to Section 3.1. The shaft mechanical power is assumed to follow the $C_p(\lambda)$ curve shown in Figure 2.4. In Figure 3.3 the gear-box losses and the induction generator losses are plotted as a function of wind speed, for the configurations with one and two generators. In the case with two generators the break-even point of the produced power determines the switch-over from the small generator to the bigger one.

In Table 3.2 the gain in energy of the wind turbine equipped with two generators compared with the wind turbine equipped with one generator is presented. It can be seen in the table that it is beneficial to use two generators compared to one. It should be pointed out that if the rotor radius of the wind turbine has been optimized with respect to generator and the average wind speed, for the case with an average wind speed of 5.4 m/s, the gain in energy might have been lower than in the table. The average value of the produced power has been found from (3.10). The reason that

Table 3.2: Gain in energy for a two-generator system in comparison to a one-generator system.

Average wind speed m/s	Gain in energy %
5.4	8.01
6.8	3.67
8.2	2.04

the wind turbine with two generators performs better is mainly due to the fact that

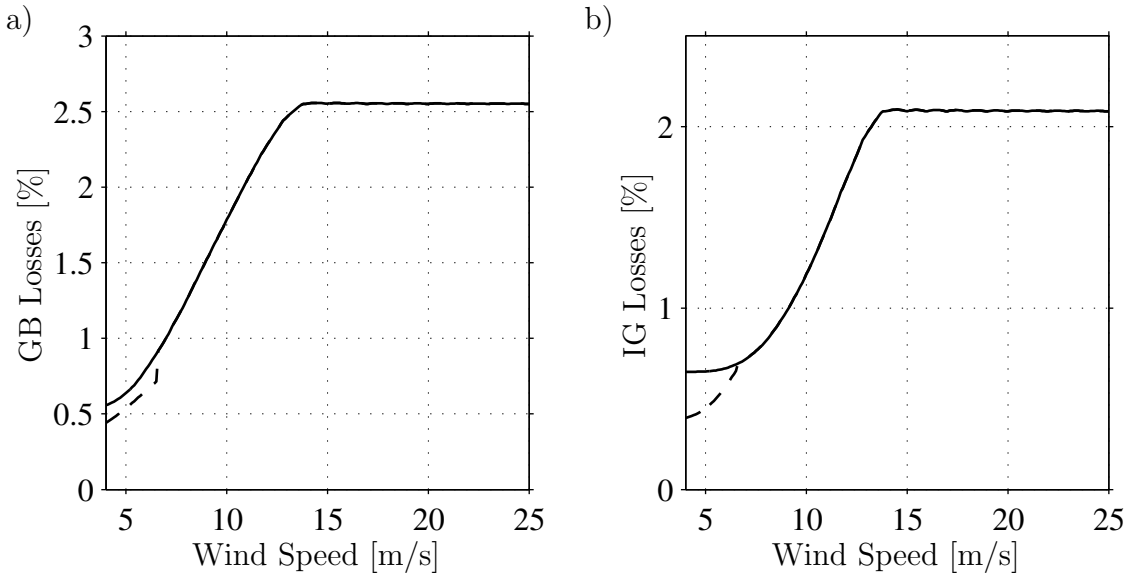

Figure 3.2: a) Gear-box losses, in percent of maximum shaft power, as a function of wind speed. One generator (solid) and two generators (dashed). b) Induction generator losses, in percent of maximum shaft power, at different wind speeds. One generator (solid) and two generators (dashed).

the smaller generator has more poles than the larger generator, i.e., the rotor speed of the smaller generator becomes closer to the rotor speed that would have given optimal tip-speed ratio, and more energy is therefore captured from the wind.

The fixed-speed system with two generators will anyway be referred to as the *fixed-speed system* and the one-generator system will not be analyzed further.

3.3 Variable-Speed Systems

For a variable-speed system where the induction generator is equipped with a stator fed inverter, i.e., the variable-speed IG system, it is possible to reduce the magnetizing losses by operating the generator on a flux that minimize the magnetizing losses of the generator. For the DFIG system there are, at least, two methods to lower the magnetizing losses of the induction generator. This can be done by:

1. By short-circuiting the stator of the induction generator at low wind speeds, and convert all power out through the inverter. Referred to as the *short-circuited DFIG*.

2. By having the stator Δ-connected at high wind speeds and Y-connected at low wind speeds; referred to as the *Y-Δ-connected DFIG*.

When the doubly-fed induction generator is Δ-connected for all wind speeds, it is referred to as the *Δ-connected DFIG*.

Steady-state calculations will be carried out in order to determine the losses of the different variable-speed systems, according to Section 3.1. For the DFIG systems the reactive power at the stator has been set to 0 VAr. It is assumed that the shaft mechanical power and the rotor speed vary according to Figure 2.5. In Figure 3.3 the gear-box losses and the losses of the induction generator are plotted. The generator losses are plotted both for the variable-speed IG system and for the DFIG systems. For the doubly-fed generators the losses are plotted for the Δ-connected, the short-circuited and the Y-Δ-connected DFIG. The break-even point of the total losses or

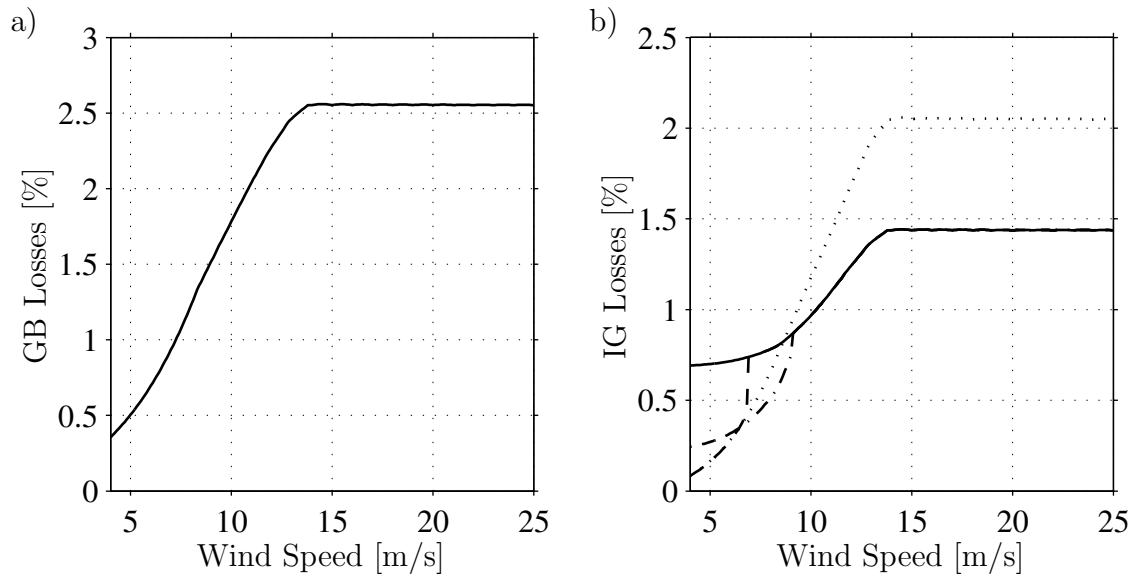

Figure 3.3: a) Gear-box losses, in percent of maximum shaft power, as a function of wind speed. b) Induction generator losses, in percent of maximum shaft power, at different wind speeds. Variable-speed IG system (dotted), Δ-connected DFIG (solid), short-circuited DFIG (dashed) and Y-Δ-connected DFIG (dash-dotted).

the rated values of the equipment determines the switch-over point, for the doubly-fed generators, i.e., the Y-Δ coupling or the synchronization of the stator voltage to the grid. It can be seen in the figure that the generator losses can be reduced for the doubly-fed generator systems with the two above mentioned methods. The inverter losses increases, see Figure 3.4a), yet the total losses will decrease as can be seen in Figure 3.4b).

In Figure 3.5 the gain in energy by reducing the magnetizing losses, by the two above-mentioned methods, is presented as a function of the rotor-speed range. The gain in energy is calculated using (3.10). It can be seen in the figure that the system with a Y-Δ-connection has approximately 0.3 percentage units lower losses than the system with short-circuited stator at low wind speeds. Since the system with a Y-Δ-connected DFIG performs better than the system with short-circuited DFIG, the system with a Y-Δ-connected DFIG will further be referred to as the *DFIG system*, and the other variants will not be subjected to any further studies.

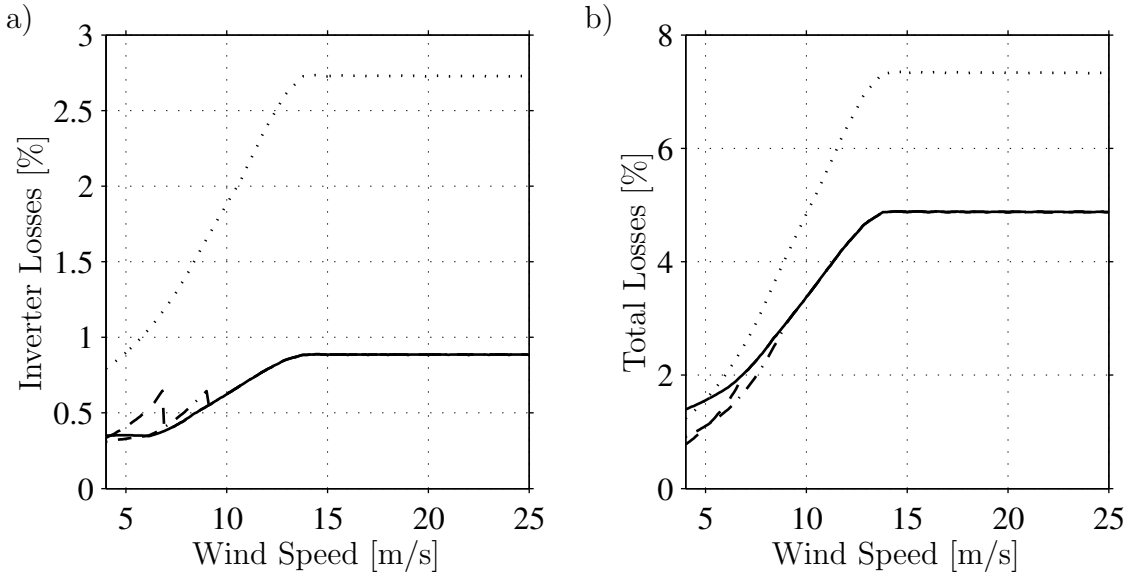

Figure 3.4: a) Inverter losses, in percent of maximum shaft power, as a function of wind speed. Variable-speed IG system (dotted), Δ-connected DFIG (solid), short-circuited DFIG (dashed) and Y-Δ-connected DFIG (dash-dotted). b) Total losses, in percent of maximum shaft power, at different wind speeds.

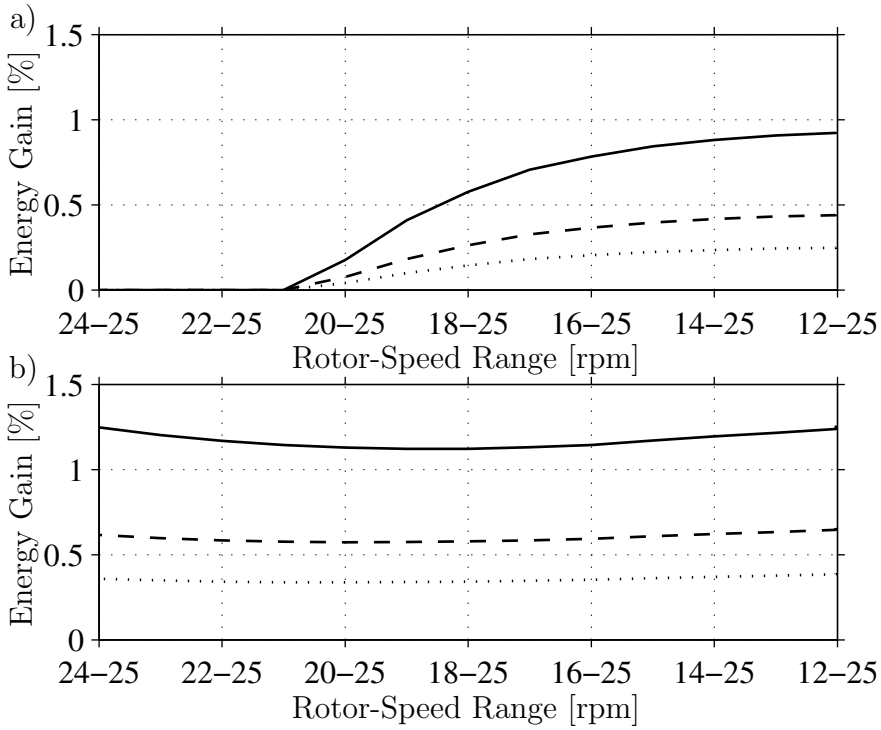

Figure 3.5: Increased gain in energy, for average wind speeds of 5.4 m/s (solid), 6.8 m/s (dashed) and 8.2 m/s (dotted), as function of the rotor speed range, for a DFIG-system when it is equipped with: a) Short-circuited DFIG. b) Y-Δ-connected DFIG.

3.3.1 Investigation of the Influence of the Stator-to-Rotor Turns Ratio

The ratings of the inverter of the doubly-fed induction generator depend on the rotor-speed range, i.e., the maximum deviation from synchronous speed. Figure 3.6a) shows the maximum power and the maximum reactive power that are fed to the doubly-fed induction generator by the inverter as a function of the rotor-speed range. Since the inverter losses depend on the current through the valves, it is important to design the stator-to-rotor turns ratio, indicated with the transformer in Figure 2.10, of the generator properly, i.e., so the rotor currents become as small as possible. In Figure 3.6a)

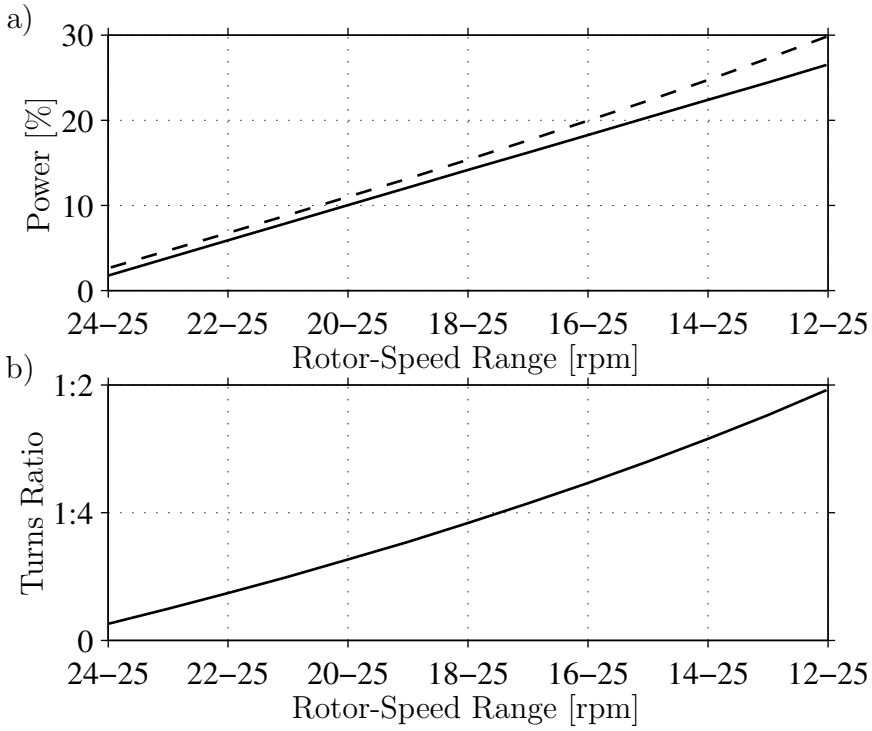

Figure 3.6: a) Maximum active power (solid) and maximum reactive power (dashed) that the inverter supply the doubly-fed induction generator. Active power is in percent of maximum active power and reactive power is in percent of maximum reactive power, respectively, that is handled by the inverter in the variable-speed IG system. b) Stator-to-rotor turns ratio.

it can be seen that the size of the inverter increases, and thereby the cost of the inverter, with the rotor-speed range. In this section the stator-to-rotor turns ratio, for the doubly-fed induction generator, is adjusted so that maximum rotor voltage is 75 % of the rated voltage, i.e., 75 % of 690 V. This is done in order to have safety margin, e.g. in case of a wind gust. Figure 3.6b) the stator-to-rotor turns ratio, to achieve the maximum desired rotor voltage, is plotted.

In Figure 3.7 the inverter losses are plotted for different designs of the rotor-speed range. It can be seen in the figure that the inverter losses become smaller for high

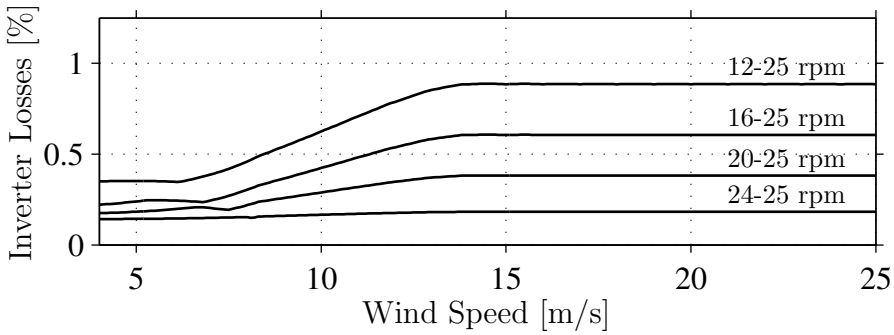

Figure 3.7: Inverter losses for some different rotor-speed ranges.

stator-to-rotor turns ratios, i.e. for a small rotor-speed range. Note that if the rotor-speed range is limited, it is not possible to obtain the optimal tip speed ratio, λ, of the wind turbine at low wind speeds.

3.4 Comparison Between Different Systems

In Figure 3.8 the gain in energy for a DFIG system compared to fixed-speed system, variable-speed IG system, and the PMSG system, for different average wind speeds, as a function of the rotor-speed range, is presented. The average efficiency, with an average wind speed of 6.8 m/s, for the permanent-magnet synchronous generator is taken from [22]. The inverter losses of the permanent-magnet synchronous generator system are assumed similar to the stator-fed induction generator system. It can be seen in the figure that the gain in energy increases with the rotor-speed range, even though the inverter losses of the DFIG system increases with the rotor-speed range. One reason for this is that if the rotor-speed range increases, the DFIG can operate at optimal tip speed ratio, λ, for lower and lower wind speeds. If the rotor-speed range is set ideally, i.e., it is possible to run at optimal tip-speed ratio in the whole variable-speed area, the DFIG system produces approximately the same amount of energy as the fixed-speed system. Further, it can be seen that there is a possibility to gain a few percentage units (approximately 3 %) in energy efficiency compared to a variable-speed IG system. In comparison to a direct-driven PMSG system there might be a slight gain in the energy depending on the average wind speed

3.5 Conclusions

In this section the gain in total energy produced by the doubly-fed induction generator system compared to the stator-fed generator system, for a wind turbine application, has been studied. It was found that if the range of the variable speed is set properly, there is the possibility to gain a few percentage units (approximately 3 %) in energy efficiency compared to a variable-speed induction generator. In comparison to a direct-

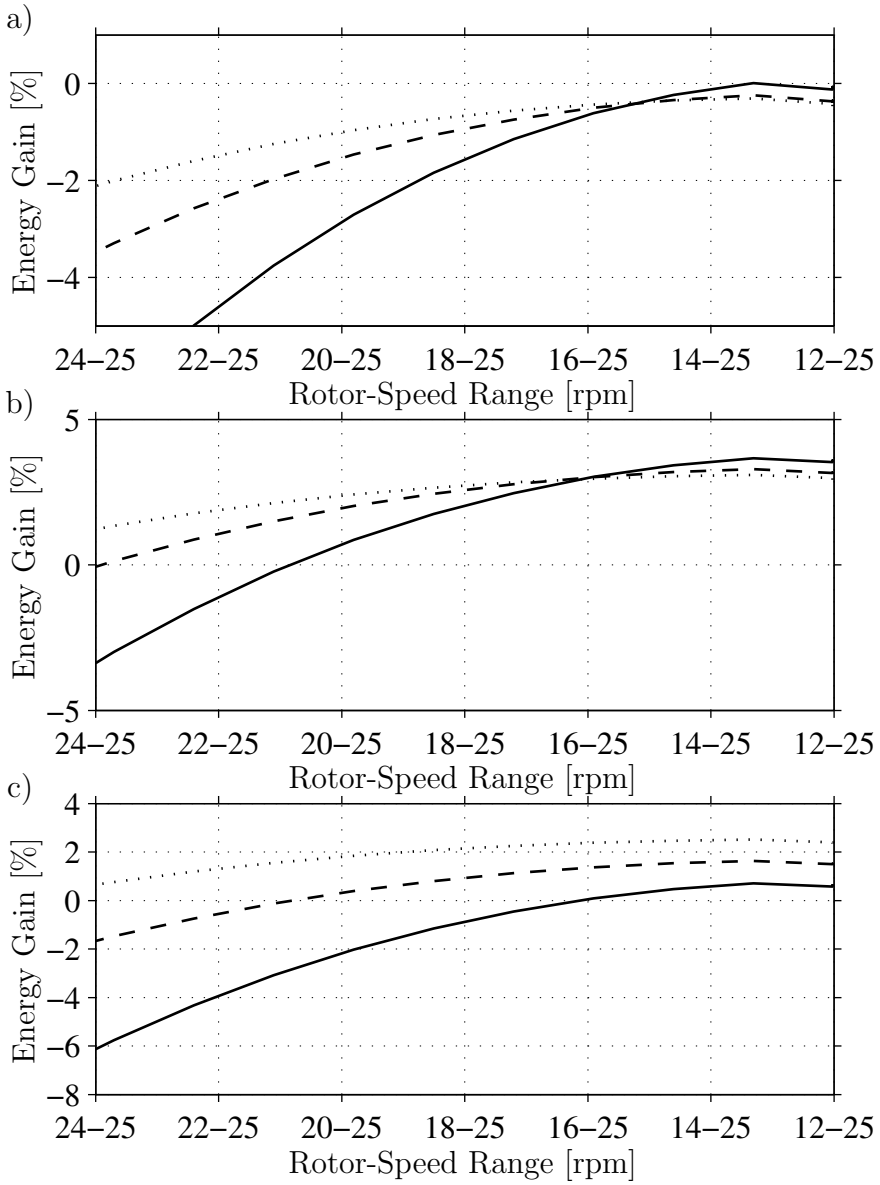

Figure 3.8: Gain in energy production for a DFIG-system, for average wind speeds of 5.4 m/s (solid), 6.8 m/s (dashed) and 8.2 m/s (dotted), as a function of the rotor speed range. The gain in energy is in comparisons with a) Fixed-speed system. b) Variable-speed IG system. c) PMSG system.

driven permanent-magnet synchronous generator system there might be a slight gain in the energy depending on the average wind speed.

The stator-to-rotor turns ratio is an important design parameter for lowering the losses of the doubly-fed induction generator system.

In comparison with the result obtained in [9], there is a great difference in the gain in energy (even for a high average wind speed), i.e., 3 % in comparison with 20 % for the doubly-fed induction generator system compared to the variable-speed induction generator system. Further, in this study it was found that the fixed-speed

system produces approximately the same amount of energy as the doubly-fed induction generator system, while in [9] the gain in energy for the doubly-fed induction generator system is 60 %. Probable reasons for this might be, in [9] the electric and mechanical losses are neglected, the maximum power, that can be produced, of each turbine is different and that the result is only calculated with one simulated wind speed (with an average value of 10 m/s).

The results found here are fairly similar to the ones found by Mutschler et al. [45]. However, here the energy capture by a two-generator fixed-speed turbine and a variable-speed system was found to be almost the same, while Mutschler et al. [45] found a difference of 1–8 %. The higher value was for a low average wind speed.

Chapter 4

Steady-State Analysis of Doubly-Fed Induction Machines

In this chapter, suitable models of standard induction machine (IM) and the doubly-fed induction machine (DFIM) for steady-state calculations will be presented. Further, the operational profile (speed–torque characteristics) of the induction machine and how it is possible to affect these characteristics are shown. There are two main types of rotors in the induction machines: the short-circuited squirrel-cage rotor and the wound rotor with slip rings that either can be short-circuited or connected to an external electric circuit. This circuit can either be connected to a passive load (resistors) or an active source (converter). The most commonly used rotor is the short-circuited squirrel-cage rotor. In applications where it is desired to influence the rotor circuit, a wound rotor with slip rings can be used, to be able to affect the speed–torque characteristics without changing the stator supply. An application can for example be to increase the starting torque (by increasing the rotor resistance by external resistances) or to control the speed of a wind turbine. Machines fed from the stator and the rotor are called DFIM. DFIM concepts are presented in Section 4.3.

4.1 Equivalent Circuit

Figure 4.1 shows a diagram over the steady-state equivalent circuit of the short-circuited induction machine [43]. This equivalent circuit is valid for one equivalent Y-phase and for steady-state calculations. In the case that it is Δ-connected the machine can still be represented by this equivalent Y representation. In this section the $\mathrm{j}\omega$-method is adopted for calculations. In the equivalent circuit $\mathbf{V}_s$ is the applied phase stator voltage to the induction machine, $\mathbf{I}_s$ is the stator current, $\mathbf{I}_r$ is the rotor current, R_s is the stator resistance, R_r is the rotor resistance, $L_{s\lambda}$ is the stator leakage inductance, $L_{r\lambda}$ is the rotor leakage inductance, R_m represents the magnetizing losses, L_m is the magnetizing inductance, ω_1 is the stator angular frequency, and s is the slip. The

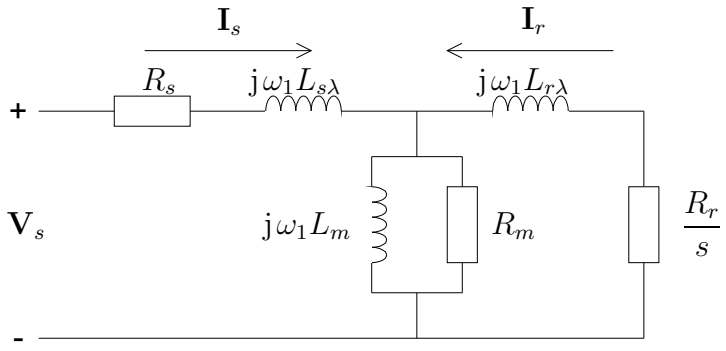

Figure 4.1: Equivalent circuit of the induction machine with a short-circuited rotor.

latter is defined by

$$s = \frac{\omega_1 - \omega_r}{\omega_1} = \frac{\omega_2}{\omega_1} \tag{4.1}$$

where ω_r is the rotor speed (referred to the electrical side).

Most induction machines have a short-circuited rotor, but to be able to influence the rotor circuit, the induction machine must be equipped with a wound rotor equipped with slip rings. In order to take the wound rotor with slip rings into consideration we have to extend the equivalent circuit with the applied phase rotor voltage, $\mathbf{V}_r$. The equivalent circuit with the inclusion of an external rotor voltage can be seen in Figure 4.2, [54].

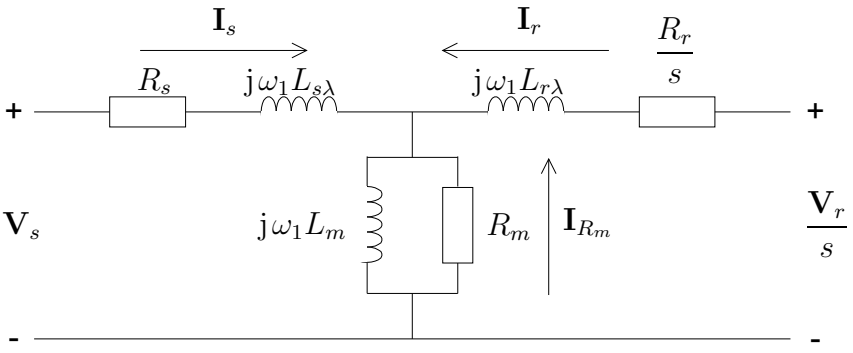

Figure 4.2: Equivalent circuit of the induction machine with inclusion of rotor voltage.

Applying Kirchhoff's voltage law to the circuit in Figure 4.12 yields

$$\mathbf{V}_s = R_s\mathbf{I}_s + \mathrm{j}\omega_1 L_{s\lambda}\mathbf{I}_s + \mathrm{j}\omega_1 L_m(\mathbf{I}_s + \mathbf{I}_r + \mathbf{I}_{R_m}) \tag{4.2}$$

$$\frac{\mathbf{V}_r}{s} = \frac{R_r}{s} + \mathrm{j}\omega_1 L_{r\lambda}\mathbf{I}_r + \mathrm{j}\omega_1 L_m(\mathbf{I}_s + \mathbf{I}_r + \mathbf{I}_{R_m}) \tag{4.3}$$

$$0 = R_m\mathbf{I}_m + \mathrm{j}\omega_1 L_m(\mathbf{I}_s + \mathbf{I}_r + \mathbf{I}_{R_m}) \tag{4.4}$$

where $\mathbf{I}_{R_m}$ is the current through R_m. The mechanical power, P_{mech}, and the losses,

P_{loss}, of the induction machine can be found as

$$P_{\text{mech}} = 3|\mathbf{I}_r|^2 R_r \frac{1-s}{s} - 3\text{Re}\Big[\mathbf{V}_r \mathbf{I}_r^*\Big] \frac{1-s}{s} \tag{4.5}$$

$$P_{\text{loss}} = 3R_s|\mathbf{I}_s|^2 + 3R_r|\mathbf{I}_r|^2 + 3R_m|\mathbf{I}_{R_m}|^2 \tag{4.6}$$

where the multiplication by 3 is due to the fact that the induction machines has three phases. The electromechanical torque, T_e, can be found from

$$T_e = P_{\text{mech}} \frac{n_p}{(1-s)\omega_1} = 3|\mathbf{I}_r|^2 R_r \frac{n_p}{s\omega_1} - 3\text{Re}\Big[\mathbf{V}_r \mathbf{I}_r^*\Big] \frac{n_p}{s\omega_1} \tag{4.7}$$

where n_p is the number of pole pairs. Table 4.1 shows typical parameters of the induction machine in per unit (p.u.).

Table 4.1: Typical parameters of the induction machine in p.u., [65].

		Small Machine 4 kW	Medium Machine 100 kW	Large Machine 800 kW
Stator and rotor resistance	R_s and R_r	0.04	0.01	0.01
Leakage inductance	$L_{\sigma,\Gamma} \approx L_{s\lambda} + L_{r\lambda}$	0.2	0.3	0.3
Magnetizing inductance	L_m	2.0	3.5	4.0

4.2 Steady-State Characteristics

In this section the speed–torque characteristics of the induction machine will be presented. See Appendix C.2 for data and parameters of the induction machine used in this section.

4.2.1 Induction Machine Connected to the Grid

Figure 4.3 shows the shaft torque of an induction machine as a function of rotor speed when a 22-kW induction machine is connected to a 50-Hz grid and has a short-circuited rotor, i.e., $\mathbf{V}_r = 0$. As can be seen in the figure the speed–torque characteristic is quite linear around synchronous speed, i.e., 1 p.u. If the rotor speed is below synchronous speed (positive slip) the induction machine is operating as a motor and if the rotor speed is above synchronous speed (negative slip) the induction machine is running as a generator.

4.2.2 Induction Machine with External Rotor Resistance

Section 4.1 showed how the mechanical power and the mechanical torque are given by the slip, rotor resistance and the rotor current, see (4.7). The speed–torque characteristic of the induction machine is quite linear around synchronous speed, as could be

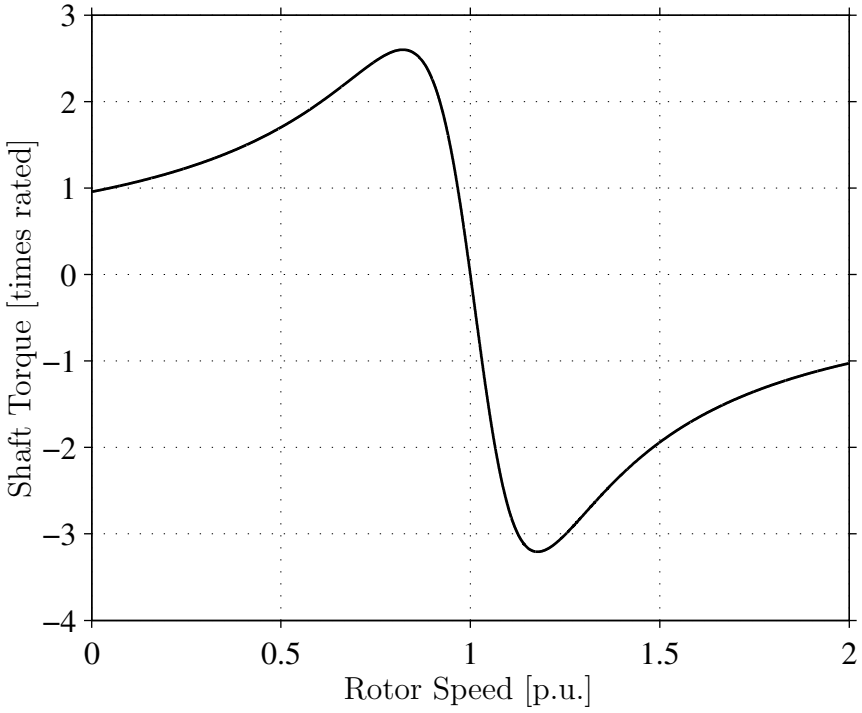

Figure 4.3: Shaft torque of the induction machine with a short-circuited rotor, $\mathbf{v}_r = 0$, as a function rotor speed.

seen in Figure 4.3, and the torque in (4.7) is proportional to the inverse of the rotor resistance. This implies that it is possible to have external rotor resistances connected in series with the existing rotor resistances of a wound-rotor induction machine. By changing the value of the external rotor resistance it is possible to change the slope of the speed–torque characteristic. Figure 4.4 shows the speed–torque characteristic for three different rotor resistances. One disadvantage with this method is that it is only possible to increase the slip using the external rotor resistances. This implies that if the induction machine is running as a motor, then an increased rotor resistance will decrease the rotor speed. On the other hand, if the induction machine is running as a generator, then if the rotor resistance increases, the rotor speed will also increase, see Figure 4.4.

4.2.3 Induction Machine with Slip Power Recovery (Using a Diode Rectifier)

Before semiconductors were available, one way of adjusting the slip was to introduce external rotor resistances as described in previous section. The external rotor resistance will cause additional losses in the rotor circuit. When semiconductors became available it was possible to recover the slip otherwise dissipated in the external rotor resistance. Thus, the slip power can be recovered into mechanical or electrical energy; therefore this method is called "slip power recovery." The rotor current must be rectified with

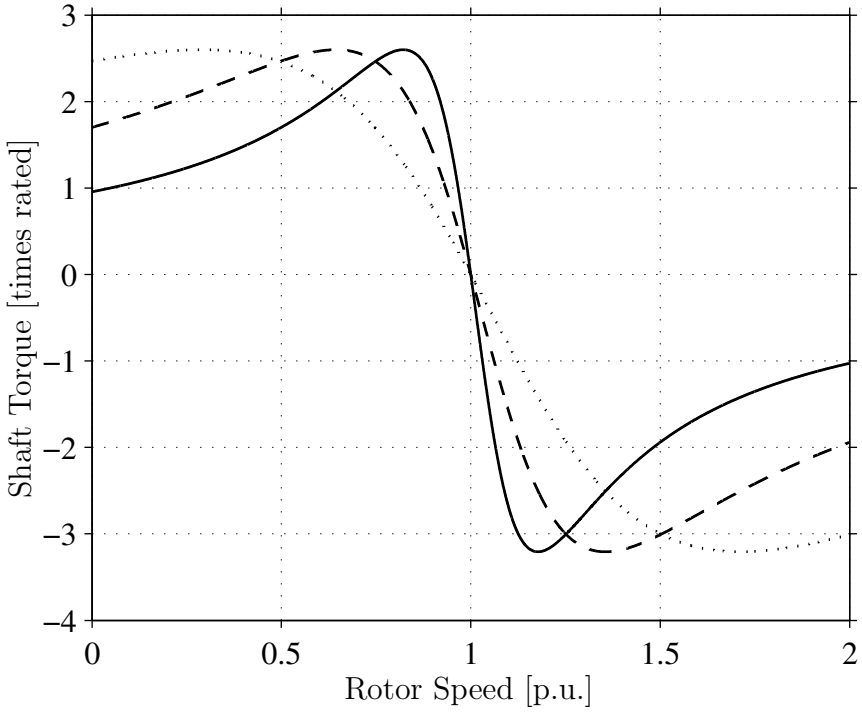

Figure 4.4: Shaft torque of the induction machine as a function rotor speed for different rotor resistances. Solid R_r equals nominal rotor resistance, dashed equals two times the nominal rotor resistance and dotted equals four times the nominal rotor resistance.

a diode rectifier. For motor operation, the rotor circuit will see the diode rectifier as a resistance and therefore this method will work approximately in the same way as for the external rotor resistances. Note that the diode rectifier cannot be used in generator operation. The rectified current could be converted to mechanical power using a dc motor coupled to the shaft of the induction motor (Krämer drive) or fed back into the grid (Scherbius drive). Since Krämer drive require an extra dc motor it is of no interest, while the Scherbius drive is still in use [42]. The main advantage of this configuration compared to the external rotor resistance is that the losses of the external rotor resistance can be recovered.

4.2.4 Induction Machine Fed by a Stator-Circuit Connected Inverter

If both stator voltage and frequency can be adjusted by an inverter, the torque–speed characteristic can be easily changed. When the speed is increased so that the stator voltage reaches maximum voltage, there is need for field weakening, i.e., the stator voltage is kept constant while the frequency is still increased. In this section it is assumed that the rotor is short-circuited, i.e., $\mathbf{V}_r = 0$.

Open-Loop Control

For applications where the dynamical performance is of a minor importance, e.g. pump and fan drives, the induction machine can be open-loop controlled, often called "volts per hertz" control. The idea is to keep the air-gap flux, Ψ_m, constant by keeping the ratio between the applied voltage and frequency constant, i.e.,

$$\text{constant} = \frac{|\mathbf{V}_s|}{\omega_1} \approx \Psi_m$$

where the approximation is due to neglecting the stator resistance and stator leakage inductance. Since the rotor only "feels" the air-gap flux and its speed relative to the rotor, the torque–speed characteristic will maintain its shape. However, the torque–speed curve will move back and forward in the speed direction. Figure 4.5 shows the speed–torque characteristics for the open-loop-controlled induction machine for different applied frequencies using (4.2)–(4.4) and (4.7). It can be seen in the figure that the shapes of the curves d) and e) differ significantly from the others. This is due to field weakening. The reason for this, as mentioned before, is that the rated voltage has been reached, but the frequency has still been increased.

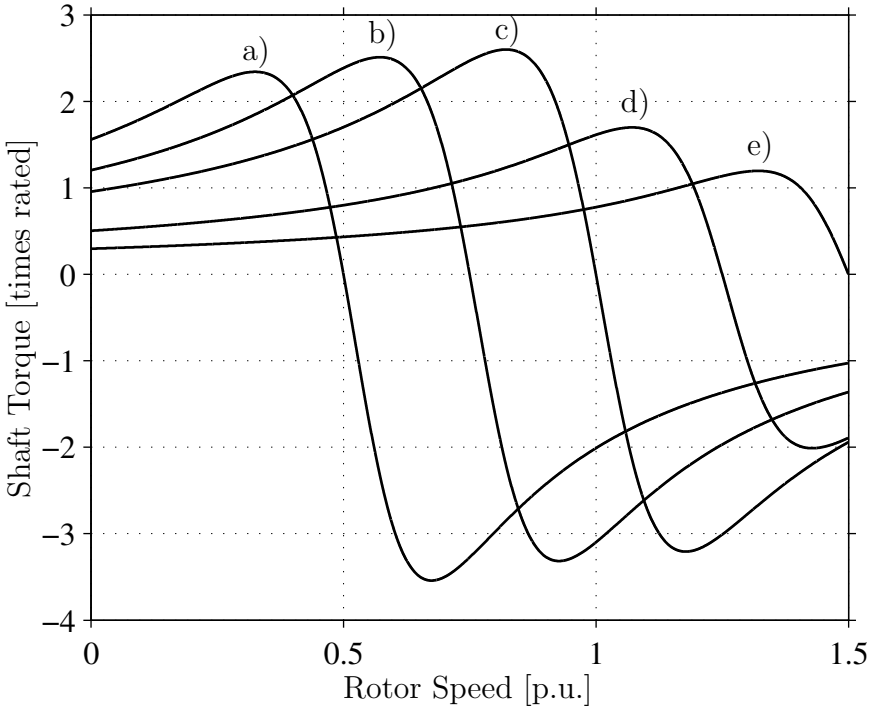

Figure 4.5: Torque–speed characteristic for an open-loop-controlled induction machine. The curves are from left to right a) $V/f = 0.5/0.5$, b) $V/f = 0.75/0.75$, c) $V/f = 1/1$, d) $V/f = 1/1.25$ (field weakening) and e) $V/f = 1/1.5$ (field weakening).

The frequency (and voltage) must be varied slowly in order to maintain stability [3]. The open-loop controlled induction machine has unstable zones in the $V - f$-plane

which are caused by the stator resistance and stator leakage inductance in the sense that these two parameters contribute to self excitation [68].

Vector Control

Vector control, or field-oriented control, of the induction machine is used where high dynamic performance of the drive is desired. The main idea behind vector control is to transform the model of the induction machine so that it is mathematically equivalent to a separately magnetized dc machine. This means that if the induction machine is fed by an inverter, it is possible to produce any torque at any speed, as long as maximum allowed torque, speed, or power is not reached. Figure 4.6 shows the operational area for an inverter-fed induction machine. In the figure the maximum allowed rotor speed

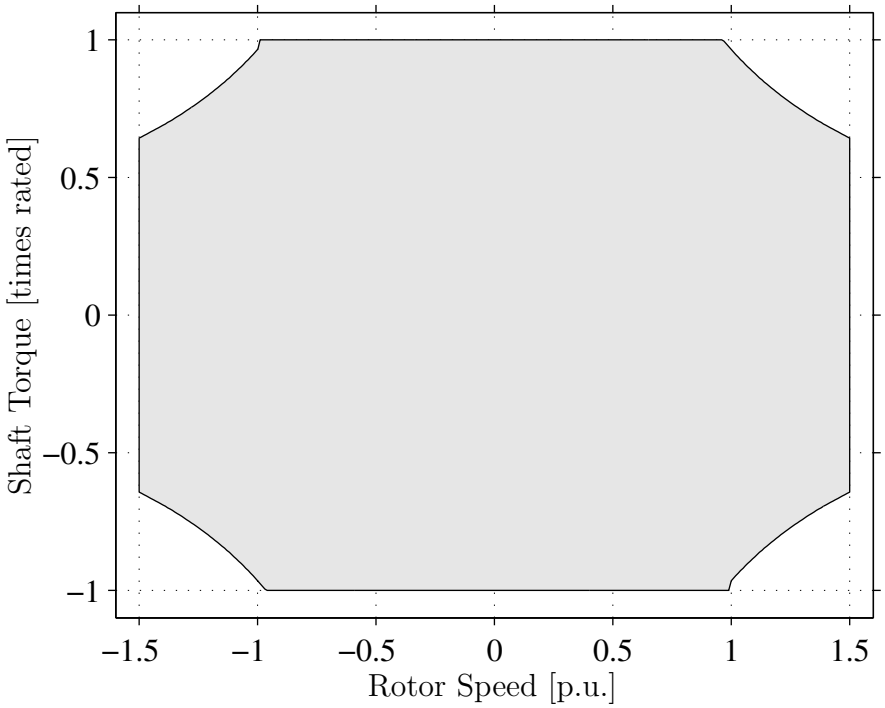

Figure 4.6: Operational area for an inverter-fed induction machine.

is set to 1.5 p.u. and the maximum torque and the maximum power are set to the rated values. Above synchronous speed, the rated power will limit the system, so that the rated torque can not be produced in this region.

4.3 Doubly-Fed Induction Machines

In this section a short presentation of different kinds of doubly-fed machines is made. The doubly-fed machine can be categorized into a *standard doubly-fed induction machine*, *cascaded doubly-fed induction machine*, *single frame cascaded doubly-fed induction machine* and *doubly-fed reluctance machine*. Hopfensperger et al. have done a

classification and comparison of various doubly-fed machines [31] which has served as a basis for this section.

Doubly-fed machines can be used in variable-speed constant-frequency applications, such as wind turbines. The main advantage of a doubly-fed machine compared to a singly-fed for a variable-speed system is the reduced rating of the converter's power rating. The reduction in power rating is dependent on the speed range of the drive [29, 31, 42].

4.3.1 Standard Doubly-Fed Induction Machine

The standard doubly-fed induction machine is a wound rotor induction machine equipped with slip rings. Figure 4.7 shows a principle diagram of the doubly-fed induction machine. The stator circuit is connected directly to the grid while the rotor circuit is controlled by an inverter via slip rings.

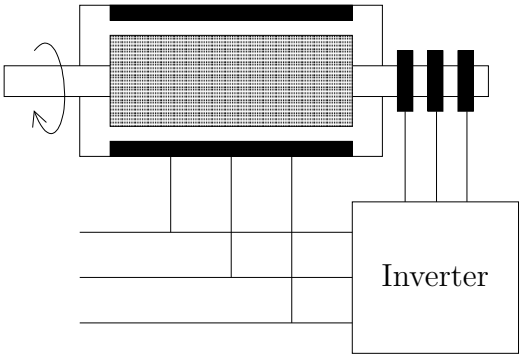

Figure 4.7: Principle of the standard doubly-fed induction machine.

In Chapter 5, control and dynamic analysis of the standard doubly-fed induction machine are treated in more detail.

4.3.2 Cascaded Doubly-Fed Induction Machine

The cascaded doubly-fed induction machine consists of two doubly-fed induction machines with wound rotors, that are connected mechanically through the rotor and electrically through the rotor circuits. See Figure 4.8 for a principle diagram. The stator circuit of one of the machines is directly connected to the grid while the other machine's stator is connected via an inverter to the grid. Since the rotor voltages of both machines are equal, it is possible to control the induction machine that is directly connected to the grid with the other induction machine.

It is possible to achieve decoupled control of active and reactive power control of the cascaded doubly-fed induction machine in a manner similar to the standard doubly-fed

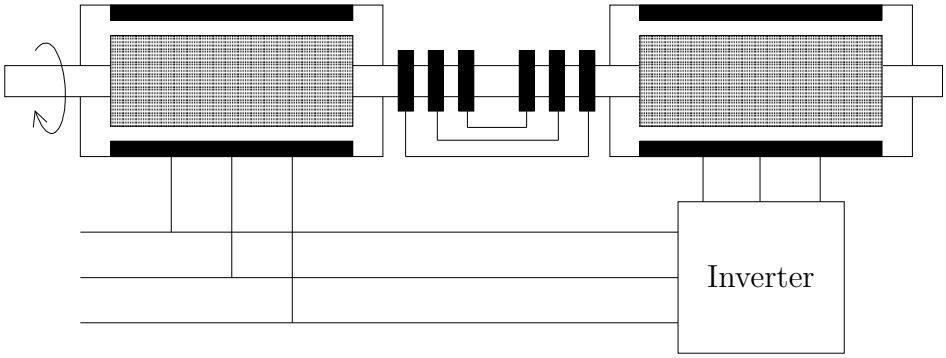

Figure 4.8: Principle of cascaded doubly-fed induction machine.

induction machine [32].

It is doubtful whether it is practical to combine two individual machines to form a cascaded doubly-fed induction machine, even though it is the basic configuration of doubly-fed induction machine arrangement. Due to a large amount of windings, the losses are expected to be higher than for a standard doubly-fed induction machine of a comparable rating [31].

Single-Frame Cascaded Doubly-Fed Induction Machine

The single-frame cascaded doubly-fed induction machine is a cascaded doubly-fed induction machine, but with the two induction machines in one common frame. Although this machine is mechanically more robust than the cascaded doubly-fed induction machine, it suffers from comparatively low efficiency [31].

4.3.3 Brushless Doubly-Fed Induction Machine

This is an induction machine with two stator windings in the same slot. That is, one winding for the power and one winding for the control. See Figure 4.9 for a principle sketch. To avoid a direct transformer coupling between the two stator windings, they can not have the same number of pole pairs. Furthermore, to avoid unbalanced magnetic pull on the rotor the difference between the pole pairs must be greater than one [71]. The number of poles in the rotor must equal the sum of the number of poles in the two stator windings [71]. For further information and more details, see [71, 73, 78].

Doubly-Fed Reluctance Machine

The stator of the doubly-fed reluctance machine is identical to the brushless doubly-fed induction machine, while the rotor is based on the principle of reluctance. An equivalent circuit with constant parameters can be obtained for the doubly-fed reluctance machine,

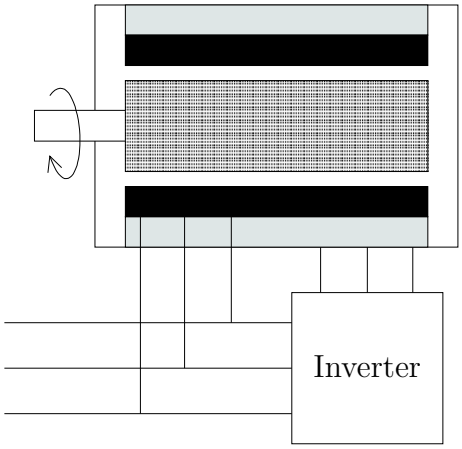

Figure 4.9: Principle of the brushless doubly-fed induction machine.

in spite the fact that the machine is characterized by a pulsating air-gap flux. It has almost the same equivalent circuit as the standard doubly-fed induction machine [75].

4.4 Steady-State Operational Characteristics of the Doubly-Fed Induction Machine

In this thesis the standard doubly-fed induction machine is the only one to be studied further, since most of the other doubly-fed machines are still in research process [31]. This is confirmed by the fact and that the standard doubly-fed induction machine is the only one used today by the major wind turbine manufacturers.

For the doubly-fed induction machine the applied rotor voltage, $\mathbf{V}_r$, can be adjusted to get the desired slip or torque. Simplified expressions of the slip can be derived from (4.2) and (4.3), by neglecting the resistances and assuming that the stator flux equals the rotor flux, as

$$s = \frac{\omega_2}{\omega_1} \approx \left|\frac{\mathbf{V}_r}{\mathbf{V}_s}\right|. \tag{4.8}$$

Since the stator is connected to the grid, the flux is mainly determined by the voltage and frequency of the grid. It is also possible to control the power factor or the reactive power in the stator circuit [76], in a similar way as for the synchronous generator. Figure 4.10 shows a principle diagram of the power flow in a doubly-fed induction machine. It can be seen in the figure that power through the inverter is the slip power, i.e., the slip, s, multiplied with the stator power, P_s. In Figure 4.11 an example of how the grid power, $P_g \approx (1-s)P_s$, the stator power, P_s, and, the rotor power, $P_r \approx -sP_s$ varies with the slip. In the figure the shaft power is constant (1 p.u.) and all losses are neglected.

The operational area for a 22-kW doubly-fed induction machine is shown in Figure 4.12. The maximum rotor voltage is set to 0.35 p.u. and the reactive power from the

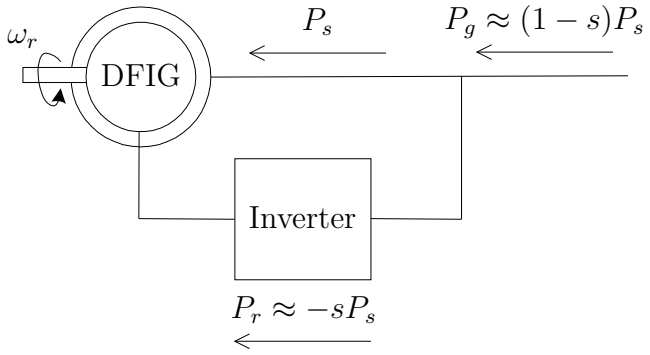

Figure 4.10: Power flow in the doubly-fed induction generator.

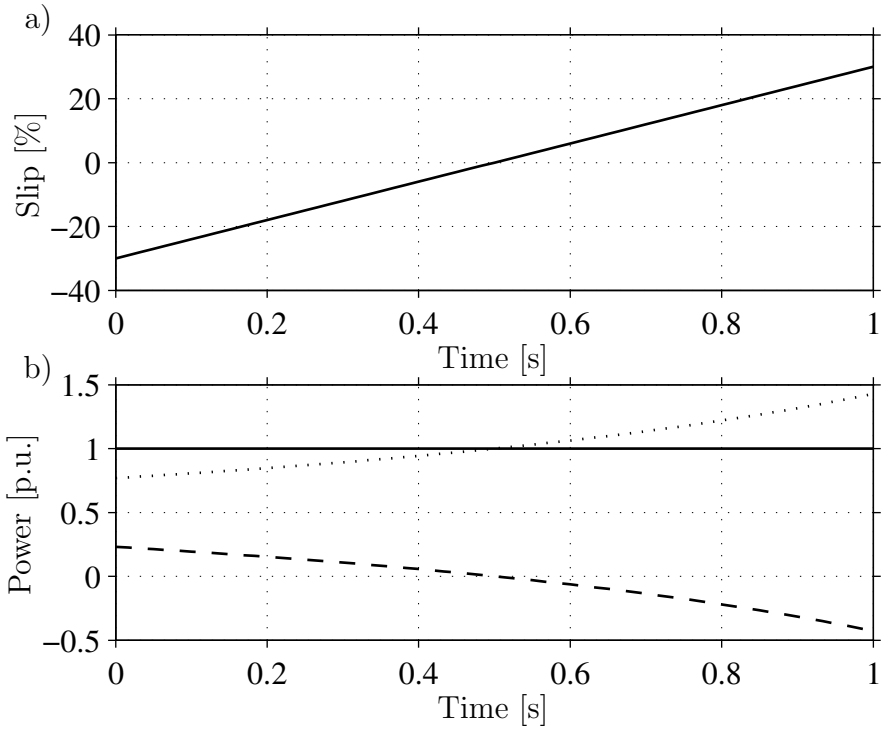

Figure 4.11: a) Slip b) Grid power (solid), stator power (dotted) and rotor power (dashed).

stator is kept at zero. As can be seen in the figure, the rotor speed can approximately vary between 0.65 to 1.35 p.u., i.e., the rotor speed can vary ±0.35 p.u. around synchronous speed. The torque can vary between plus/minus the rated torque. However, the rated power limits the torque for rotor speeds above synchronous.

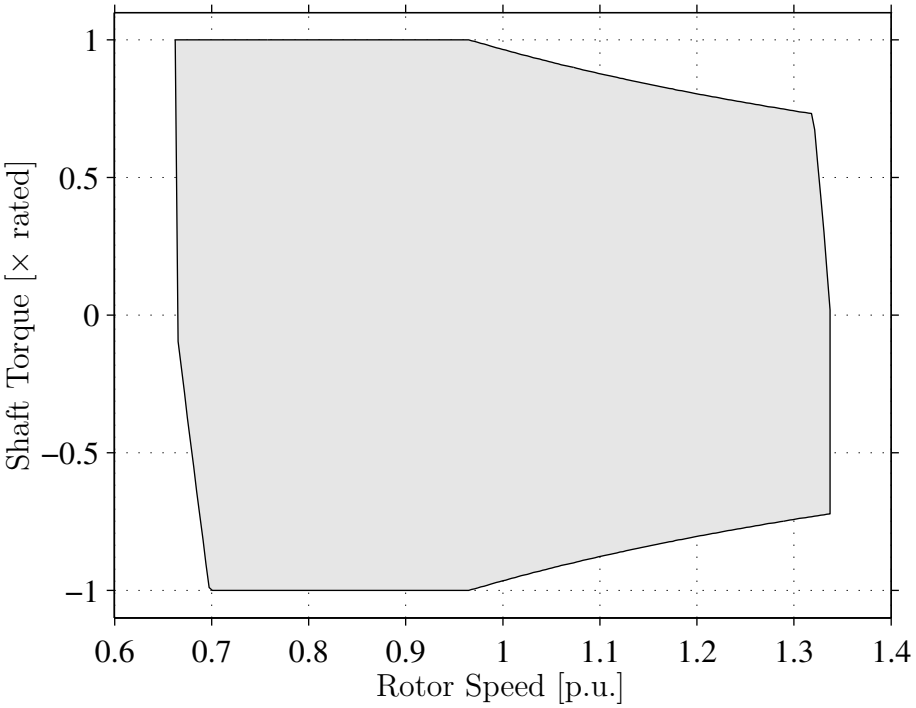

Figure 4.12: Operational area for a doubly-fed induction machine.

Chapter 5

Dynamic Modeling and Control of the Doubly-Fed Induction Machine

In this chapter dynamic space-vector models of the induction machine will be presented, suitable for different purposes. Design and implementation aspects of controllers for the DFIM will be presented. Finally, vector control of the doubly-fed induction machine is treated in detail.

5.1 Dynamic Modeling of the Induction Machine

Since all of the dynamic models of the induction machine are described in space vectors, a short description of space vectors will also be presented. The induction machine models are based on the fifth-order two-axis representation commonly know as the "Park model" [40]. The equations will be arranged in alternative representations. For certain applications it is more convenient to use the Γ representation or the inverse-Γ representation instead of the equivalent T representation.

5.1.1 Space-Vector Notation

The idea behind space vectors is to describe the induction machine with two phases instead of three. A three-phase stator winding, which is supplied with three phase currents, forms a rotating flux in the air gap. The same rotating flux could also be formed with only two phases, as seen in Figure 5.1. This is the principle of space vectors.

In order to determine the space vector, $\mathbf{s}^s$, of a three-phase quantity, s_a, s_b, and s_c, the following transformation can be applied [25]

$$\mathbf{s}^s = s_\alpha + \mathrm{j}\, s_\beta = \frac{2K}{3}\Big(s_a + \mathbf{a} s_b + \mathbf{a}^2 s_c\Big)$$

where K is a constant and

$$\mathbf{a} = \mathrm{e}^{\mathrm{j}\frac{2\pi}{3}}.$$

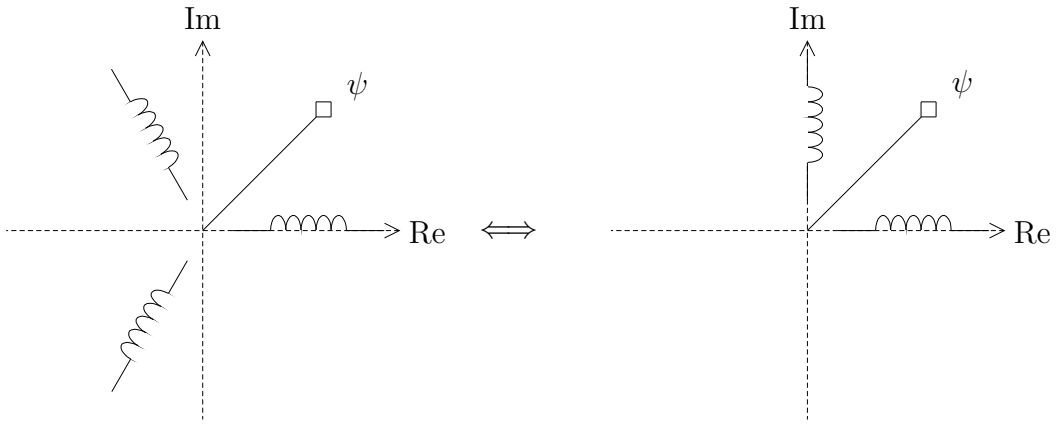

Figure 5.1: Principle of space vectors.

Superscript "s" indicates that the space vectors are referred to the reference frame of the stator of the induction machine. The constant K can be chosen arbitrary, though if it is chosen as

$$K = \frac{1}{\sqrt{2}}$$

the space vectors quantities, i.e., voltages and currents, will be scaled according to the RMS value of the three phase quantities. A general space vector, $\mathbf{s}^s$, can be expressed as

$$\mathbf{s}^s = s\mathrm{e}^{\mathrm{j}\,(\theta_1+\phi)}$$

where ϕ is a phase shift and θ_1 can be found from the synchronous frequency, ω_1, as

$$\theta_1 = \int \omega_1 \mathrm{d}t.$$

It is also possible to transform it to synchronous coordinates (dq coordinates) as

$$\mathbf{s} = s_d + \mathrm{j}\, s_q = \mathrm{e}^{-\mathrm{j}\,\theta_1}\mathbf{s}^s = \hat{s}\mathrm{e}^{\mathrm{j}\,\phi}.$$

The synchronous coordinate system is not indicated by a superscript. Space vectors in synchronous coordinates will be dc quantities in the steady state. The instantaneous power in a three-phase system is given by

$$P = v_a i_a + v_b i_b + v_c i_c = \frac{3}{2K^2}(v_\alpha i_\alpha + v_\beta i_\beta) = \frac{3}{2K^2}\mathrm{Re}\Big[\mathbf{v}\mathbf{i}^*\Big]$$

The above-mentioned choice of the scaling constant K yields

$$P = 3\mathrm{Re}\Big[\mathbf{v}\mathbf{i}^*\Big].$$

K will be chosen as $1/\sqrt{2}$ throughout this thesis.

5.1.2 Park Model (T Representation)

The stator of the induction machine can be described by the following space-vector equation [40]

$$\mathbf{v}_s^s = R_s \mathbf{i}_s^s + \frac{\mathrm{d}\boldsymbol{\Psi}_s^s}{\mathrm{d}t} \tag{5.1}$$

where $\mathbf{v}_s^s$ is the stator voltage, $\mathbf{i}_s^s$ is the stator current, R_s is the stator resistance, and $\boldsymbol{\Psi}_s^s$ is the stator flux. The equation is represented in stator coordinates, which is indicated with superscript "s." Further, the rotor equation can be described by

$$\mathbf{v}_r^r = R_r \mathbf{i}_r^r + \frac{\mathrm{d}\boldsymbol{\Psi}_r^r}{\mathrm{d}t} \tag{5.2}$$

where $\mathbf{v}_r^r$ is the rotor voltage, $\mathbf{i}_r^r$ is the rotor current, R_r is the rotor resistance and $\boldsymbol{\Psi}_r^r$ is the rotor flux. The rotor equation is described in rotor coordinates, which is indicated by superscript "r." The relation between stator and rotor coordinates is given by

$$\mathbf{x}^s = \mathrm{e}^{\mathrm{j}\,\theta_r}\mathbf{x}^r \tag{5.3}$$

where θ_r the is the rotor angle referred to the electrical system. The stator, $\boldsymbol{\Psi}_s^s$, rotor, $\boldsymbol{\Psi}_r^r$, and air-gap fluxes, $\boldsymbol{\Psi}_m^s$, are given by

$$\boldsymbol{\Psi}_s^s = L_s \mathbf{i}_s^s + L_m \mathbf{i}_r^r \mathrm{e}^{\mathrm{j}\,\theta_r} = (L_{s\lambda} + L_m)\mathbf{i}_s^s + L_m \mathbf{i}_r^r \mathrm{e}^{\mathrm{j}\,\theta_r} \tag{5.4}$$

$$\boldsymbol{\Psi}_r^r = L_m \mathbf{i}_s^s \mathrm{e}^{-\mathrm{j}\,\theta_r} + L_r \mathbf{i}_r^r = L_m \mathbf{i}_s^s \mathrm{e}^{-\mathrm{j}\,\theta_r} + (L_{r\lambda} + L_m)\mathbf{i}_r^r \tag{5.5}$$

$$\boldsymbol{\Psi}_m^s = L_m \mathbf{i}_s^s + L_m \mathbf{i}_r^r \mathrm{e}^{\mathrm{j}\,\theta_r} \tag{5.6}$$

where L_m is the magnetizing inductance, L_s is the stator inductance, L_r is the rotor inductance, $L_{s\lambda}$ is the stator leakage inductance, and $L_{r\lambda}$ is the rotor leakage inductance. The induction machine can be represented in several ways. The Park model, also called T model since the leakage inductances forms the letter "T," see Figure 5.2, can be described using (5.1) and (5.2) in stator coordinates as [40]

$$\mathbf{v}_s^s = R_s \mathbf{i}_s^s + \frac{\mathrm{d}\boldsymbol{\Psi}_s^s}{\mathrm{d}t} \tag{5.7}$$

$$\mathbf{v}_r^s = R_r \mathbf{i}_r^s + \frac{\mathrm{d}\boldsymbol{\Psi}_r^s}{\mathrm{d}t} - \mathrm{j}\,\omega_r \boldsymbol{\Psi}_r^s \tag{5.8}$$

where ω_r is the (electrical) rotor speed, i.e.,

$$\omega_r = \frac{\mathrm{d}\theta_r}{\mathrm{d}t}.$$

The term $\mathrm{j}\,\omega_r \boldsymbol{\Psi}_r^s$ in (5.8) arises from the transformation from rotor to stator coordinates. The fluxes are given by

$$\boldsymbol{\Psi}_s^s = L_s \mathbf{i}_s^s + L_m \mathbf{i}_r^s \tag{5.9}$$

$$\boldsymbol{\Psi}_r^s = L_m \mathbf{i}_s^s + L_r \mathbf{i}_r^s \tag{5.10}$$

$$\boldsymbol{\Psi}_m^s = L_m \mathbf{i}_s^s + L_m \mathbf{i}_r^s. \tag{5.11}$$

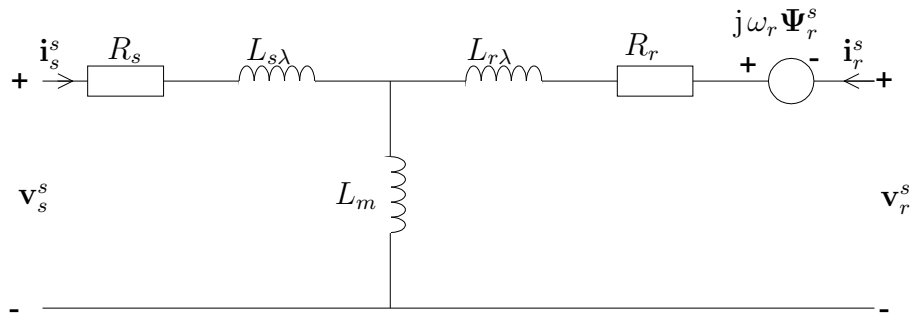

Figure 5.2: Park model (or T model) of the induction machine in stator coordinates.

Figure 5.2 shows a diagram over the T model in stator coordinates. Sometimes it is desirable to transform the Park model of the induction machine to synchronous coordinates. Transformation to synchronous coordinates implies that the variables will be dc quantities in the steady state. Transformation to synchronous coordinates implies substituting $\frac{\mathrm{d}}{\mathrm{d}t} \rightarrow \frac{\mathrm{d}}{\mathrm{d}t} + \mathrm{j}\omega_1$, where ω_1 is stator frequency (synchronous speed), or $p \rightarrow p + \mathrm{j}\omega_1$, where p is the derivative operator. The stator and rotor voltage equations become

$$\mathbf{v}_s = R_s\mathbf{i}_s + \frac{\mathrm{d}\boldsymbol{\Psi}_s}{\mathrm{d}t} + \mathrm{j}\omega_1\boldsymbol{\Psi}_s \tag{5.12}$$

$$\mathbf{v}_r = R_r\mathbf{i}_r + \frac{\mathrm{d}\boldsymbol{\Psi}_r}{\mathrm{d}t} + \mathrm{j}\omega_2\boldsymbol{\Psi}_r \tag{5.13}$$

where $\omega_2 = \omega_1 - \omega_r$ is the slip frequency. The torque production can be identified from the applied power. The applied power that is fed to the induction machine can be expressed as

$$\begin{aligned} P &= 3\mathrm{Re}\Big[\mathbf{v}_s\mathbf{i}_s^*\Big] + 3\mathrm{Re}\Big[\mathbf{v}_r\mathbf{i}_r^*\Big] \\ &= 3R_s|\mathbf{i}_s|^2 + 3R_r|\mathbf{i}_r|^2 + 3\mathrm{Re}\Big[\frac{\mathrm{d}\boldsymbol{\Psi}_s}{\mathrm{d}t}\mathbf{i}_s^* + \frac{\mathrm{d}\boldsymbol{\Psi}_r}{\mathrm{d}t}\mathbf{i}_r^*\Big] - 3\mathrm{Re}\Big[\mathrm{j}\omega_r\boldsymbol{\Psi}_m\mathbf{i}_r^*\Big] \end{aligned}$$

where we can identify the following terms:

$$\begin{aligned} P_{\text{loss}} &= 3R_s|\mathbf{i}_s|^2 + 3R_r|\mathbf{i}_r|^2 \\ P_{\text{field}} &= 3\mathrm{Re}\Big[\frac{\mathrm{d}\boldsymbol{\Psi}_s}{\mathrm{d}t}\mathbf{i}_s^* + \frac{\mathrm{d}\boldsymbol{\Psi}_r}{\mathrm{d}t}\mathbf{i}_r^*\Big] \\ P_{\text{mech}} &= -3\mathrm{Re}\Big[\mathrm{j}\omega_r\boldsymbol{\Psi}_m\mathbf{i}_s^*\Big] = 3\omega_r\mathrm{Im}\Big[\boldsymbol{\Psi}_m\mathbf{i}_s^*\Big] \end{aligned}$$

where P_{loss} is the resistive (copper) losses, P_{field} is the stored magnetic power, and P_{mech} is the mechanical power produced by the induction machine. The electromechanical torque can now be found from:

$$T_e = \frac{P_{\text{mech}}}{\omega_r/n_p} = 3n_p\mathrm{Im}\Big[\boldsymbol{\Psi}_m\mathbf{i}_r^*\Big] = 3n_p\mathrm{Im}\Big[\boldsymbol{\Psi}_r^*\mathbf{i}_s\Big] = 3n_p\mathrm{Im}\Big[\boldsymbol{\Psi}_m^*\mathbf{i}_s\Big] = 3n_p\mathrm{Im}\Big[\boldsymbol{\Psi}_s\mathbf{i}_r^*\Big]. \tag{5.14}$$

The mechanical dynamics can be described by the following differential equation:

$$J\frac{1}{n_p}\frac{\mathrm{d}\omega_r}{\mathrm{d}t} = T_e - T_s \tag{5.15}$$

where T_s is the applied shaft torque, ω_r is the electrical rotor speed, and J is the inertia.

5.1.3 Γ Representation

From a dynamic point of view, the rotor and the stator leakage inductance have the same effect. Therefore, it is possible to use a different representation of the Park model in which the leakage inductance is placed in the rotor circuit, the so-called Γ *representation* of the induction machine [59]. The Γ representation is more suitable to work with when developing control laws than the Park model. The Γ-representation is particularly suited for control in which it is attempted to keep the magnitude of the stator flux constant [59]. This model is named Γ representation since the inductances form the letter "Γ," see Figure 5.3. This model can be described by the following vector

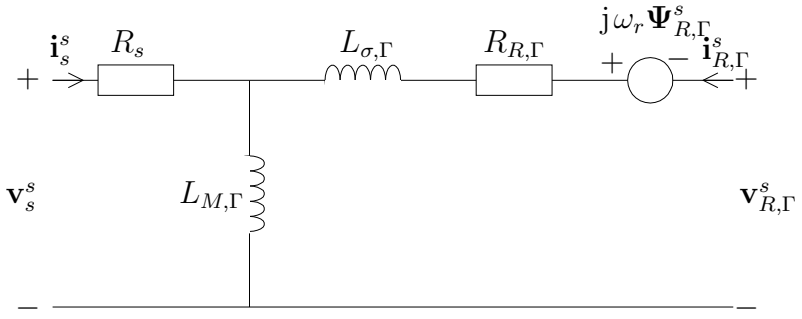

Figure 5.3: Γ representation of the induction machine in stator coordinates.

equations in stator and rotor coordinates, respectively:

$$\mathbf{v}_s^s = R_s\mathbf{i}_s^s + \frac{\mathrm{d}\boldsymbol{\Psi}_s^s}{\mathrm{d}t} \tag{5.16}$$

$$\mathbf{v}_{R,\Gamma}^r = R_{R,\Gamma}\mathbf{i}_{R,\Gamma}^r + \frac{\mathrm{d}\boldsymbol{\Psi}_{R,\Gamma}^r}{\mathrm{d}t} \tag{5.17}$$

or transformed to synchronous coordinates as

$$\mathbf{v}_s = R_s\mathbf{i}_s + \frac{\mathrm{d}\boldsymbol{\Psi}_s}{\mathrm{d}t} + \mathrm{j}\omega_1\boldsymbol{\Psi}_s \tag{5.18}$$

$$\mathbf{v}_{R,\Gamma} = R_{R,\Gamma}\mathbf{i}_{R,\Gamma} + \frac{\mathrm{d}\boldsymbol{\Psi}_{R,\Gamma}}{\mathrm{d}t} + \mathrm{j}\omega_2\boldsymbol{\Psi}_{R,\Gamma} \tag{5.19}$$

where the fluxes are given by

$$\boldsymbol{\Psi}_s = L_{M,\Gamma}(\mathbf{i}_s + \mathbf{i}_{R,\Gamma}) \tag{5.20}$$

$$\boldsymbol{\Psi}_{R,\Gamma} = L_{M,\Gamma}\mathbf{i}_s + (L_{\sigma,\Gamma} + L_{M,\Gamma})\mathbf{i}_{R,\Gamma} = L_{\sigma,\Gamma}\mathbf{i}_{R,\Gamma} + \boldsymbol{\Psi}_s. \tag{5.21}$$

The quantities and parameters of the Γ model relate to the Park model as follows:

$$\mathbf{v}_{R,\Gamma} = \gamma_\Gamma\mathbf{v}_r \qquad \mathbf{i}_{R,\Gamma} = \frac{\mathbf{i}_r}{\gamma_\Gamma} \qquad \boldsymbol{\Psi}_{R,\Gamma} = \gamma_\Gamma\boldsymbol{\Psi}_r \qquad \gamma_\Gamma = \frac{L_s}{L_m}$$

$$R_{R,\Gamma} = \gamma_\Gamma^2 R_r \qquad L_{\sigma,\Gamma} = \gamma_\Gamma L_{s\lambda} + \gamma_\Gamma^2 L_{r\lambda} \qquad L_{M,\Gamma} = \gamma_\Gamma L_m.$$

The electromechanical torque can be found from (5.14) as

$$T_e = 3n_p \mathrm{Im}\Big[\boldsymbol{\Psi}_m \mathbf{i}_r^*\Big] = 3n_p \mathrm{Im}\Big[\boldsymbol{\Psi}_r \mathbf{i}_r^*\Big] = 3n_p \mathrm{Im}\Big[\boldsymbol{\Psi}_{R,\Gamma} \mathbf{i}_{R,\Gamma}^*\Big] = 3n_p \mathrm{Im}\Big[\boldsymbol{\Psi}_s \mathbf{i}_{R,\Gamma}^*\Big]. \quad (5.22)$$

5.1.4 Inverse-Γ Representation

In the Γ model the leakage inductance is reduced to the rotor side. It is also possible to reduce the leakage inductance to the stator side. This will accordingly be called the *inverse-Γ representation*. The inverse-Γ representation is more suitable to work with for control where the rotor-flux magnitude is maintained at a constant value [59]. The inductances form an "inverse Γ" sign, see Figure 5.4. This model can be described by the following vector equations in synchronous coordinates:

$$\mathbf{v}_s = R_s \mathbf{i}_s + \frac{\mathrm{d}\boldsymbol{\Psi}_s}{\mathrm{d}t} + \mathrm{j}\omega_1 \boldsymbol{\Psi}_s \quad (5.23)$$

$$\mathbf{v}_R = R_R \mathbf{i}_R + \frac{\mathrm{d}\boldsymbol{\Psi}_R}{\mathrm{d}t} + \mathrm{j}\omega_2 \boldsymbol{\Psi}_R \quad (5.24)$$

where the fluxes are given by

$$\boldsymbol{\Psi}_s = (L_\sigma + L_M)\mathbf{i}_s + L_M \mathbf{i}_R$$
$$\boldsymbol{\Psi}_R = \boldsymbol{\Psi}_M = L_M(\mathbf{i}_s + \mathbf{i}_R).$$

As can be seen in the above equation, the rotor flux equals the air-gap flux for the inverse-Γ representation.

Figure 5.4 shows a circuit diagram of the inverse-Γ representation in stator coordinates. The quantities and parameters of the inverse-Γ representation relates to the

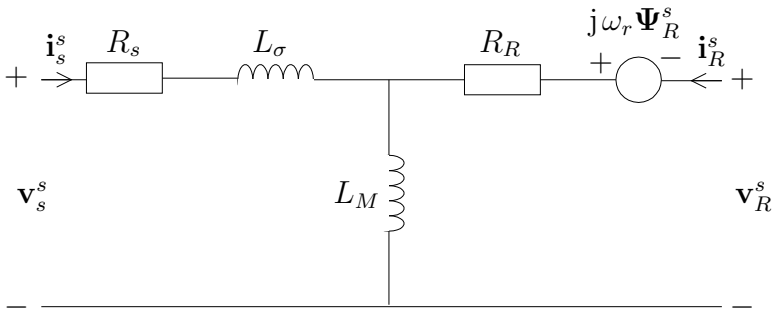

Figure 5.4: Inverse-Γ representation of the induction machine in stator coordinates.

Park model as follows:

$$\mathbf{v}_R = \gamma \mathbf{v}_r \qquad \mathbf{i}_R = \frac{\mathbf{i}_r}{\gamma} \qquad \boldsymbol{\Psi}_R = \gamma \boldsymbol{\Psi}_r \qquad \gamma = \frac{L_m}{L_r}$$
$$R_R = \gamma^2 R_r \qquad L_\sigma = L_{s\lambda} + \gamma L_{r\lambda} \qquad L_M = \gamma L_m.$$

The electromechanical torque can be found from (5.14) as

$$T_e = 3n_p \mathrm{Im}\Big[\boldsymbol{\Psi}_m \mathbf{i}_r^*\Big] = 3n_p \mathrm{Im}\Big[\boldsymbol{\Psi}_r \mathbf{i}_r^*\Big] = 3n_p \mathrm{Im}\Big[\boldsymbol{\Psi}_R \mathbf{i}_R^*\Big] = 3n_p \mathrm{Im}\Big[\boldsymbol{\Psi}_R^* \mathbf{i}_s\Big]. \quad (5.25)$$

Note that the Γ representation, the inverse-Γ representation, and the T representations are identical to each other with respect to the dynamic and the steady-state performance.

5.2 Induction Machine Control

In this section, different aspects of designing and implementing control systems for induction machines are treated.

5.2.1 Cascade Control

Since the electrical and mechanical dynamics are in different time scales, i.e., the electrical dynamics are much faster than the mechanical, it might be advantageous to control the machine in a cascade structure. Since the electrical dynamics are the fastest, the current has to be controlled in an inner loop. Then a speed controller can be added in an outer slower loop, see Figure 5.5. If the inner control loop is set much

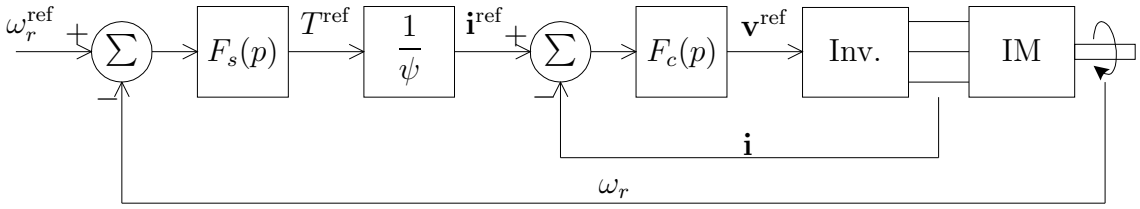

Figure 5.5: Cascade control.

faster, than the outer, it is possible to neglect the dynamics of the inner control loop, i.e., assuming its transfer function to be 1. This assumption will usually make the design of the outer control loop much easier.

5.2.2 Controller Design

There are a number of methods for designing controllers, such as pole placement, linear quadratic, and internal model control (IMC) [20]. Due to the simplicity of IMC for designing controller it will be used throughout this thesis. IMC can, for instance, be used for current or speed control of any ac machine [26, 30, 66]. The idea behind IMC is to augment the error between the system, $G(p)$, and the model of the system, $\hat{G}(p)$, by a transfer function $C(p)$, see Figure 5.6. It is just a matter of choosing the right transfer function $C(p)$. The closed-loop system will be

$$G_{cl}(p) = G(p)\Big(1 + C(p)[G(p) - \hat{G}(p)]\Big)^{-1} C(p). \tag{5.26}$$

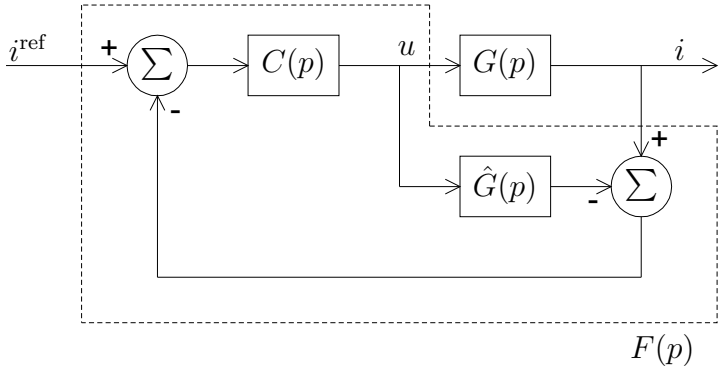

Figure 5.6: Principle of IMC.

One common way of choosing the transfer function $C(p)$ when $\hat{G}(p)$ has more poles than zeros is [20]

$$C(p) = \left(\frac{\alpha}{p+\alpha}\right)^n \hat{G}^{-1}(p) \tag{5.27}$$

where n is chosen so that $C(p)$ become implementable, i.e., the order of the denominator is greater than of the numerator. The parameter α is a design parameter adjusted to the desired bandwidth of the closed-loop system. The controller, $F(p)$, becomes (inside the dashed area in Figure 5.6)

$$F(p) = \left(1 - C(p)\hat{G}(p)\right)^{-1} C(p). \tag{5.28}$$

For a first-order system, $n = 1$ is sufficient. The controller then becomes an ordinary PI controller:

$$F(p) = k_p + \frac{k_i}{p} = \frac{\alpha}{p}\hat{G}^{-1}(p) \tag{5.29}$$

where k_p is the proportional gain and k_i is the integral gain. The closed-loop system with ideal parameters becomes

$$G_{cl}(p) = G(p)C(p) = \frac{\alpha}{p+\alpha}. \tag{5.30}$$

The relationship between the bandwidth and the rise time (10 %–90 %), when $n = 1$, is $\alpha = \ln 9/t_{\text{rise}}$.

5.2.3 Saturation and Anti-Windup

When designing control laws, the control signal cannot be arbitrary large due to design limitations of the inverter or the machine. Therefore, the control signal must be limited (saturated). This causes the integral part of the PI-controller to accumulate the control error during the saturation, i.e., integration "wind-up." This might cause overshoots in the controlled variable since the integration part of control law will keep

the ideal control signal high even when the controlled variable is getting closer to the reference value [25].

One method to avoid integration wind-up is to use the "back-calculation" method [25]. Another anti-windup method can be found in [62]. The idea behind the back-calculation method is to modify the reference value, in case of saturation, so that the ideal control signal, u, does not exceed the maximum value, i.e., $|u| = u_{\max}$. The algorithm can be described as [25]

$$u = k_p e + k_i I \tag{5.31}$$

$$u_{\text{sat}} = \text{sat}(u) \tag{5.32}$$

$$\frac{\mathrm{d}I}{\mathrm{d}t} = e + \frac{u_{\text{sat}} - u}{k_p} \tag{5.33}$$

where e is the control error and I is the integral of the control error.

5.2.4 Discretization

Throughout the thesis, differential equations and control laws will be described in continuous time. However, when implementing control laws in computers, they have to be discretized. The forward Euler method will be used, i.e., a derivative is approximated as

$$\dot{x}(t) \approx \frac{x(n+1) - x(n)}{T_{\text{sample}}} \tag{5.34}$$

where n indicates the sample number, at time $t = nT_{\text{sample}}$. For a continuous system given as

$$\dot{x}(t) = Ax(t) + Bu(t) \tag{5.35}$$

$$y(t) = Cx(t) \tag{5.36}$$

the discrete equivalent using the forward Euler method then becomes

$$x(n+1) = (I + AT_{\text{sample}})x(n) + T_{\text{sample}}Bu(n) \tag{5.37}$$

$$y(n) = Cx(n). \tag{5.38}$$

The forward Euler discretization can also be written as

$$p \longrightarrow \frac{q-1}{T_{\text{sample}}} \tag{5.39}$$

where q is the forward shift operator. Stability of a linear time-invariant continuous systems requires that the poles are in the left half plane. For a linear time-invariant discrete system the corresponding stability region is inside the unit circle [55]. Mapping the unit circle onto the continuous p plane using (5.39) gives the region in the p plane

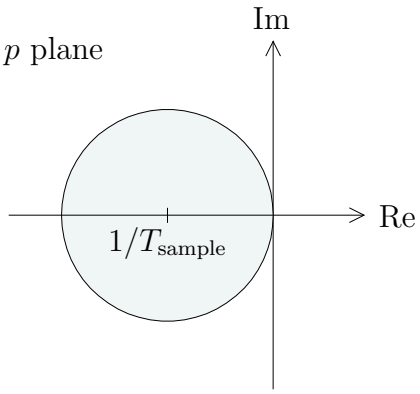

Figure 5.7: Region of stability.

where the poles of the continuous system must be located in order to get a stable discretization [24]. Figure 5.7 shows where the poles of continuous system must be located so that the forward Euler discretization, in (5.39), becomes stable. As can be seen in the figure the poles must be inside a circle with the radius of $1/T_{\text{sample}}$ with the center point located at $(-1/T_{\text{sample}}, 0)$ in order for the forward Euler discretization to be stable.

5.3 Vector Control of the Doubly-Fed Induction Machine

In the literature, vector control of the doubly-fed induction machine has been done in several ways. One common way is to control the rotor currents with stator-flux orientation [33, 42, 49, 63] or with air-gap-flux orientation [72, 76]. If the stator resistance can be considered small, the stator-flux orientation gives orientation also with the stator voltage [8, 42, 44]. According to [8], pure stator-voltage orientation can be done without any significant error. Another method presented in the literature is to control the stator currents with stator voltage orientation [50]. In this thesis, stator-flux-oriented rotor current control is adopted. This is due to the fact that the torque, with this choice of reference, is only dependent on the q component of the rotor current in the steady state for a stator-flux-oriented system. For stator-flux-oriented control of the doubly-fed induction machine it is advantageous to use the Γ model [59].

In [8, 33] the current controller is based on the dynamics described by (5.19). Using the relation in (5.21), i.e., $\boldsymbol{\Psi}_{R,\Gamma} = L_{\sigma,\Gamma}\mathbf{i}_{R,\Gamma} + \boldsymbol{\Psi}_s$, the rotor equation can be rewritten as

$$\begin{aligned}\mathbf{v}_{R,\Gamma} &= R_{R,\Gamma}\mathbf{i}_{R,\Gamma} + \frac{\mathrm{d}\boldsymbol{\Psi}_{R,\Gamma}}{\mathrm{d}t} + \mathrm{j}\,\omega_2\boldsymbol{\Psi}_{R,\Gamma} \\ &= (R_{R,\Gamma} + \mathrm{j}\,\omega_2 L_{\sigma,\Gamma})\mathbf{i}_{R,\Gamma} + L_{\sigma,\Gamma}\frac{\mathrm{d}\mathbf{i}_{R,\Gamma}}{\mathrm{d}t} + \frac{\mathrm{d}\boldsymbol{\Psi}_s}{\mathrm{d}t} + \mathrm{j}\,\omega_2\boldsymbol{\Psi}_s. \end{aligned} \tag{5.40}$$

Since the stator flux, $\boldsymbol{\Psi}_s$, is almost fixed to the stator voltage it is practically constant. This implies that the derivative of stator flux is close to zero and can be neglected [8]. The term $\mathrm{j}\hat{\omega}_2 L_{\sigma,\Gamma}\mathbf{i}_{R,\Gamma}$, in (5.40), introduces a cross coupling between the rotor current's d and q components. It is possible to decouple the cross coupling in the control law [8, 49], while [33] states that the influence is of minor importance since it is an order of magnitude smaller than the term $\mathrm{j}\omega_2\boldsymbol{\Psi}_s$. Nevertheless, in this thesis the d and q components will be decoupled since for a DSP-based digital controller is easy to implement. Hence, if the rotor voltage is chosen as

$$\mathbf{v}_{R,\Gamma} = \mathbf{v}'_{R,\Gamma} + \mathrm{j}\omega_2 L_{\sigma,\Gamma}\mathbf{i}_{R,\Gamma} \tag{5.41}$$

the rotor currents will be decoupled. The rotor current dynamics in (5.40) can now be written as

$$\mathbf{v}'_{R,\Gamma} = R_{R,\Gamma}\mathbf{i}_{R,\Gamma} + L_{\sigma,\Gamma}\frac{\mathrm{d}\mathbf{i}_{R,\Gamma}}{\mathrm{d}t} + \mathbf{E} \tag{5.42}$$

where $\mathbf{E} = \frac{\mathrm{d}\boldsymbol{\Psi}_s}{\mathrm{d}t} + \mathrm{j}\omega_2\boldsymbol{\Psi}_s \approx \mathrm{j}\omega_2\boldsymbol{\Psi}_s$ is defined as the back emf. Treating the back emf as a disturbance, the transfer function from the rotor voltage, $\mathbf{v}'_{R,\Gamma}$, to the rotor current, $\mathbf{i}_{R,\Gamma}$, can be found as

$$\mathbf{G}(p) = \frac{1}{pL_{\sigma,\Gamma} + R_{R,\Gamma}}. \tag{5.43}$$

Using IMC (see Section 5.2.2) to design the current controllers yields

$$\mathbf{F}(p) = k_p + \frac{k_i}{p} = \frac{\alpha_c}{p}\mathbf{G}^{-1}(p) \tag{5.44}$$

where α_c is the bandwidth of the current control loop, k_p is the proportional gain and k_i is the integral gain. The proportional and the integral gains become

$$k_p = \alpha_c L_{\sigma,\Gamma} \qquad k_i = \alpha_c R_{R,\Gamma}. \tag{5.45}$$

In Figure 5.8 a block diagram of the current control scheme. In the figure the actual induction machine is in the dashed box.

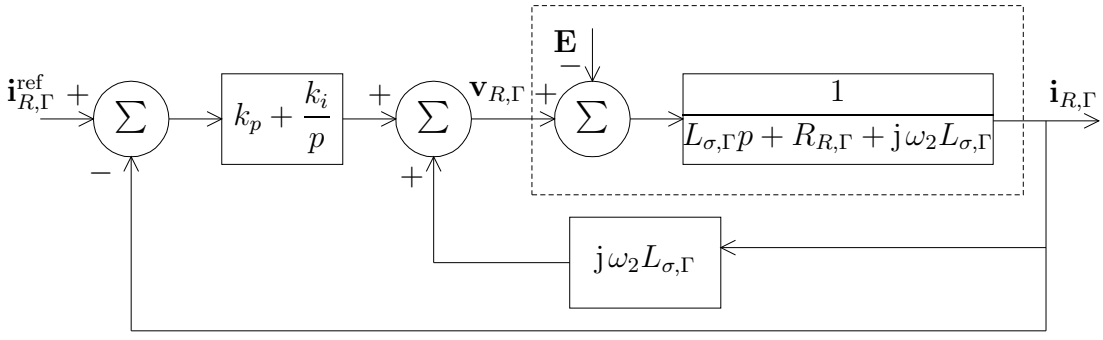

Figure 5.8: Block diagram of the current control system.

Hence, the current control law can be written as

$$\mathbf{v}_{R,\Gamma} = k_p \mathbf{e} + k_i \int \mathbf{e}\, \mathrm{d}t + \mathrm{j}\omega_2 L_{\sigma,\Gamma} \mathbf{i}_{R,\Gamma} \tag{5.46}$$

where $\mathbf{e} = \mathbf{i}_{R,\Gamma}^{\mathrm{ref}} - \mathbf{i}_{R,\Gamma}$ is the control error, k_p is the proportional gain, k_i is the integral gain and the term $\mathrm{j}\omega_2 L_{\sigma,\Gamma} \mathbf{i}_{R,\Gamma}$ is added in order to decouple the d and q components of the rotor current.

In order to evaluate the performance of the current controller, simulations of the system have been carried out. In Figure 5.9, a simulation of the current control with three different bandwidths, α_c, 0.14 p.u., 1.4 p.u., and 14 p.u., can be seen. As can be

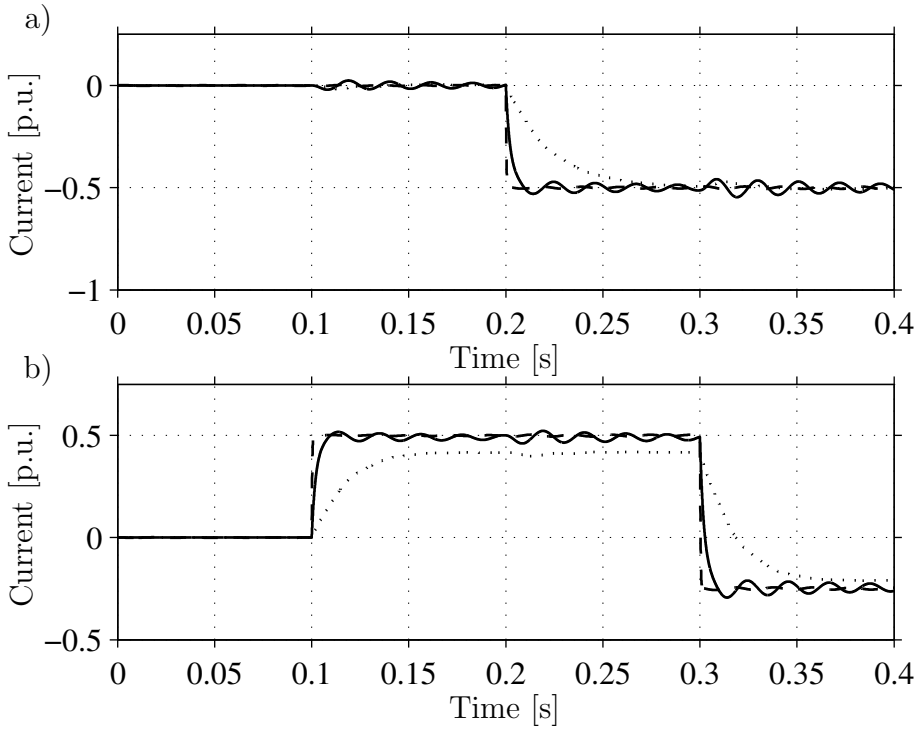

Figure 5.9: Simulation of rotor current control. The reference values are initially set to zero, and after 0.1 s, $i_{Rq,\Gamma}^{\mathrm{ref}}$ changes to 0.5 p.u., after 0.2 s, $i_{Rd,\Gamma}^{\mathrm{ref}}$, changes to -0.5 p.u., and finally after 0.3 s $i_{Rq,\Gamma}^{\mathrm{ref}}$ changes to -0.25 p.u. The bandwidth of the current control loop is set to 0.14 p.u. (50 ms rise time) dotted line, 1.4 p.u. (5 ms rise time) solid line and 14 p.u. (0.5 ms rise time) dashed line. a) The rotor current's d component b) The rotor current's q component

seen in Figure 5.9b) the rotor current does not reach the the reference value perfectly if the bandwidth of the current controller is set to 0.14 p.u. This tracking error is caused by the back emf, $\mathbf{E}$. The back emf, $\mathbf{E} \approx \mathrm{j}\omega_2 \boldsymbol{\Psi}_s$, is dependent of the slip frequency ω_2. A step in the q component rotor current implies that the electromechanical torque will be changed accordingly since it is proportional to the rotor current's q component. The induction machine, in this simulation, operates under no-load conditions, which

implies that the rotor speed will vary according to (5.15), i.e.,

$$J\frac{1}{n_p}\frac{\mathrm{d}\omega_r}{\mathrm{d}t} = T_e. \tag{5.47}$$

If the electromechanical torque is constant and differs from zero, the above equation implies that the rotor speed, ω_r, will vary as a ramp. Since the stator frequency, ω_1, is almost fixed to the grid frequency, the slip frequency will vary according to $\omega_2 = \omega_1 - \omega_r$. This tracking error can be eliminated with an increased bandwidth of the current control loop [33], which also can be seen in Figure 5.9b).

It can also be seen in Figure 5.9 that oscillations occur in the current when the bandwidth is set to 1.4 p.u. The reason for this is that the bandwidth is close to the excitation frequency of the stator voltage and oscillations occur in the stator flux. The stator flux, and the derivative of the stator flux in the back emf, will affect the performance of the current controller. The explicit reason for the oscillations in the stator flux will be further discussed in Section 5.3.2. If the bandwidth of the current controller is increased even further, to e.g. 14 p.u., the current controller is fast enough to handle the disturbance and oscillations caused by the back emf.

The main disturbance to the current controller is the back emf, $\mathbf{E}$. The transfer function from the back emf to the current can be expressed as

$$\begin{aligned}\frac{\mathbf{I}_{R,\Gamma}(p)}{\mathbf{E}(p)} &= -\frac{p}{L_{\sigma,\Gamma}p^2 + (R_{R,\Gamma} + k_p)p + k_i} \\ &= -\frac{p}{L_{\sigma,\Gamma}p^2 + (R_{R,\Gamma} + \alpha_c L_{\sigma,\Gamma})p + \alpha_c R_{R,\Gamma}}.\end{aligned} \tag{5.48}$$

In Figure 5.10 a Bode plot of the above transfer function can be seen for different bandwidths, i.e., the same bandwidths as in Figure 5.9. In the figure it can be seen that if the bandwidth of the rotor current controller increases, the damping of the back emf, $\mathbf{E}$, becomes better.

5.3.1 Current Control with Feed-Forward of the Back EMF

As described previous, the back emf causes a tracking error, when the rotor speed changes, in the current if the bandwidth is small enough. It is possible to include a feed-forward compensating term in the control law that will compensate for the tracking error caused by the back emf [33, 42, 49]. This can be done by setting the rotor voltage equal

$$\mathbf{v}_{R,\Gamma} = \mathbf{v}'_{R,\Gamma} + \mathrm{j}\omega_2 L_{\sigma,\Gamma}\mathbf{i}_{R,\Gamma} + \mathrm{j}\omega_2\boldsymbol{\Psi}_s. \tag{5.49}$$

In a similar way as before, the rotor-current dynamics in (5.40) can be rewritten as

$$\mathbf{v}'_{R,\Gamma} = R_{R,\Gamma}\mathbf{i}_{R,\Gamma} + L_{\sigma,\Gamma}\frac{\mathrm{d}\mathbf{i}_{R,\Gamma}}{\mathrm{d}t} + \frac{\mathrm{d}\boldsymbol{\Psi}_s}{\mathrm{d}t} \approx R_{R,\Gamma}\mathbf{i}_{R,\Gamma} + L_{\sigma,\Gamma}\frac{\mathrm{d}\mathbf{i}_{R,\Gamma}}{\mathrm{d}t}. \tag{5.50}$$

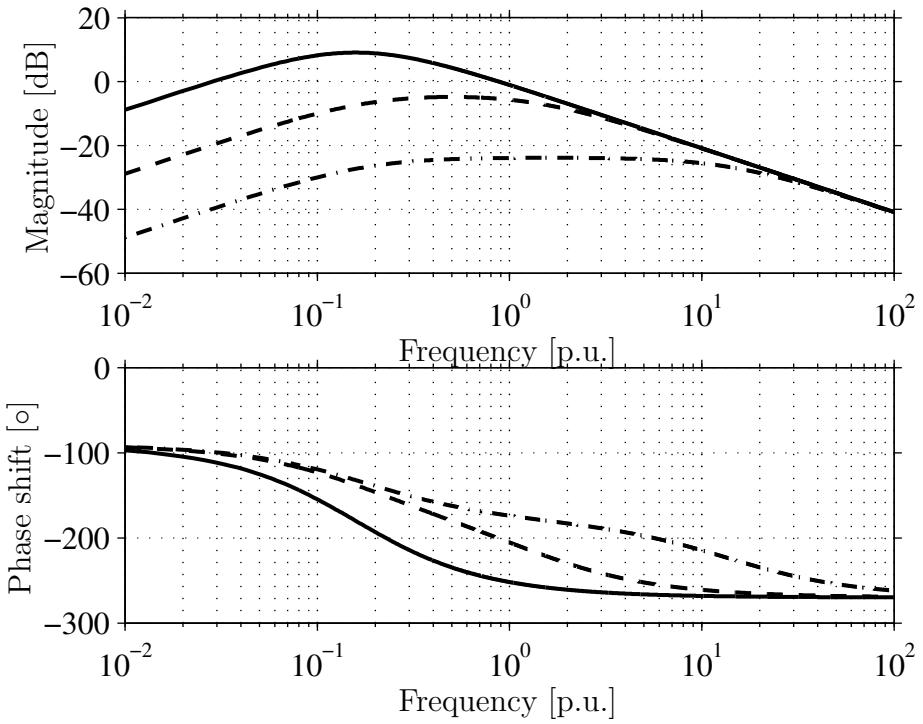

Figure 5.10: Bode plot of the transfer function from the back emf, **E**, to the current. Solid line corresponds to a bandwidth of 0.14 p.u., dashed line to a bandwidth 1.4 p.u. and dash-dotted to a bandwidth of 14 p.u.

Neglecting the derivative of the stator flux, the proportional and integral gains of the controller can still be found from (5.45). In Figure 5.11 a simulation of current control with feed-forward of the back emf is presented. The assumptions of this simulation is identical to the assumptions of the simulation in Figure 5.9 except for the feed-forward of the back emf in the control law. It can be seen in Figure 5.11 that the tracking error has vanished, although oscillations in the d component rotor current can still be seen. The reason for this is that the derivative of the stator flux has been neglected.

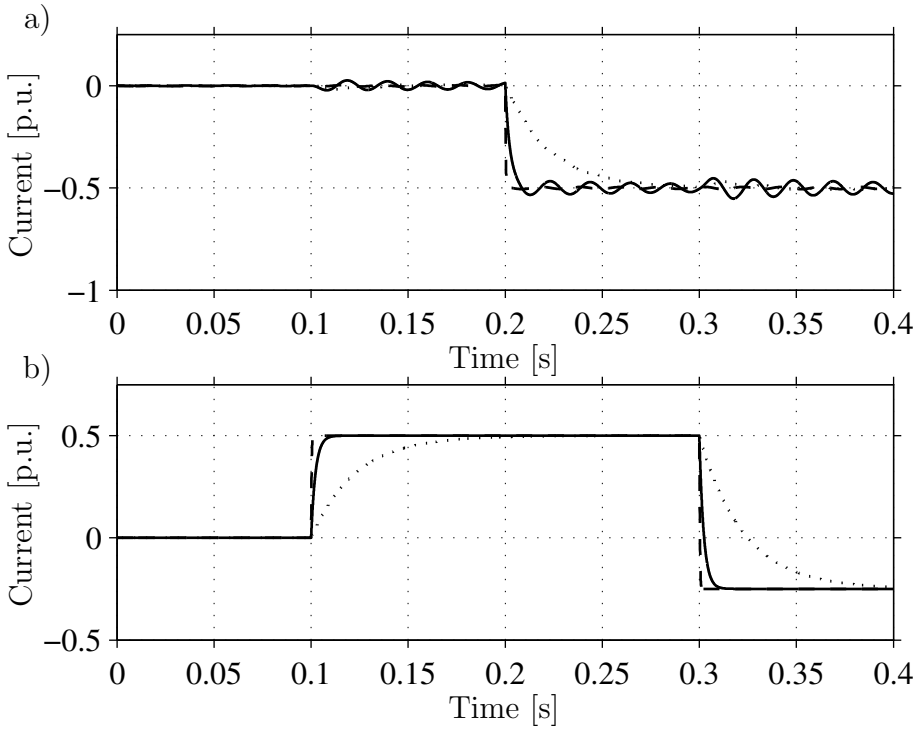

Figure 5.11: Simulation of rotor current control with feed-forward of the back emf. The reference values are initially set to zero and, after 0.1 s, $i^{\text{ref}}_{Rq,\Gamma}$ changes to 0.5 p.u., after 0.2 s, $i^{\text{ref}}_{Rd,\Gamma}$ changes to -0.5 p.u., and finally after 0.3 s, $i^{\text{ref}}_{Rq,\Gamma}$ changes to -0.25 p.u. The bandwidth of the current control loop is set to 0.14 p.u. (50 ms rise time) dotted line, 1.4 p.u. (5 ms rise time) solid line and 14 p.u. (0.5 ms rise time) dashed line. a) The rotor current's d component b) The rotor current's q component.

5.3.2 Stability Analysis

In [72] Wang et al. have by simulations derived that 1) the flux is influenced both by load change and stator power supply variations, 2) the flux response is a damped oscillation, and 3) the flux and rotor current oscillate more severely when speed is rising than when the speed is falling. Heller et al. [29] have investigated the stability of the doubly-fed induction machine mathematically. They have shown that the dynamics of the doubly-fed induction machine have poorly damped eigenvalues with a corresponding natural frequency near the line frequency and that when the d component rotor current exceeds a certain value, the system turns unstable. It is concluded that either it is necessary to reduce the bandwidth of the current control loops or to implement an additional flux damper [29]. But if the bandwidth of the current control loop is reduced, the assumption of fast current dynamics might not hold. In Section 6.1.4 a stability analysis will be performed when the current dynamics are considered.

This section will present a stability analysis, using Lyapunov's linearization method [60], of the flux dynamics in a way similar to what has been done in [6, 29]. Since the

current dynamics are assumed much faster than the flux dynamics we can neglect the current dynamics when analyzing the stability. The flux dynamics can be found from (5.18). Eliminating the stator current in (5.18) using (5.20) yields

$$\mathbf{v}_s = -R_s \mathbf{i}_{R,\Gamma} + \frac{\mathrm{d}\mathbf{\Psi}_s}{\mathrm{d}t} + \Big(\frac{R_s}{L_{M,\Gamma}} + \mathrm{j}\,\omega_1\Big)\mathbf{\Psi}_s. \tag{5.51}$$

The stator voltage in stator coordinates equals $\mathbf{v}_s^s = \mathrm{j}\, v_s \mathrm{e}^{\mathrm{j}\,\theta_s}$, where θ_s is grid angle. Transformation to synchronous coordinates gives

$$\mathbf{v}_s = \mathrm{j}\, v_s \mathrm{e}^{\mathrm{j}\,(\theta_s - \theta_1)} \tag{5.52}$$

where θ_1 is the angle that corresponds to the synchronous speed ω_1. Splitting (5.51) into real and imaginary parts, assuming stator-flux orientation, i.e., $\mathbf{\Psi}_s = \psi_s$, yields

$$\frac{\mathrm{d}\psi_s}{\mathrm{d}t} = -v_s \sin(\theta_s - \theta_1) + R_s i_{Rd,\Gamma} - \frac{R_s}{L_{M,\Gamma}}\psi_s \tag{5.53}$$

$$\frac{\mathrm{d}\theta_1}{\mathrm{d}t} = \omega_1 = \frac{v_s \cos(\theta_s - \theta_1) + R_s i_{Rq,\Gamma}}{\psi_s}. \tag{5.54}$$

Making the variable substitution $\Delta\theta = \theta_s - \theta_1$ yields

$$\frac{\mathrm{d}\psi_s}{\mathrm{d}t} = -v_s \sin(\Delta\theta) + R_s i_{Rd,\Gamma} - \frac{R_s}{L_{M,\Gamma}}\psi_s \tag{5.55}$$

$$\frac{\mathrm{d}\Delta\theta}{\mathrm{d}t} = \frac{\mathrm{d}\theta_s}{\mathrm{d}t} - \frac{\mathrm{d}\theta_1}{\mathrm{d}t} = \omega_s - \frac{v_s \cos(\Delta\theta) + R_s i_{Rq,\Gamma}}{\psi_s} \tag{5.56}$$

where ω_s is the frequency of the applied stator voltage. Eqs. (5.55) and (5.56) form a non-linear system. This system has two equilibrium points (neglecting the periodic solutions of the trigonometric functions). One of the solutions corresponds to negative flux, which is not reasonable, therefore it is not applicable. The second equilibrium point becomes

$$\psi_{s0,\Gamma} \approx \frac{v_s + R_s i^{\mathrm{ref}}_{Rq,\Gamma}}{\omega_s} - \frac{R_s^2 (v_s - \omega_s L_{M,\Gamma} i^{\mathrm{ref}}_{Rd,\Gamma})^2}{2 L_{M,\Gamma}^2 v_s \omega_s^3} \tag{5.57}$$

$$\Delta\theta_0 \approx -\frac{R_s}{L_{M,\Gamma}} \frac{v_s + R_s i^{\mathrm{ref}}_{Rq,\Gamma} - \omega_s L_{M,\Gamma} i^{\mathrm{ref}}_{Rd,\Gamma}}{v_s \omega_s} \tag{5.58}$$

where the approximations are obtained as a second-order Taylor series expansion of the equilibrium point around $R_s = 0$. See Figure 5.12 for a phase portrait. Linearization of the system around the equilibrium point yields the following characteristic polynomial

$$p^2 + \frac{R_s}{L_{M,\Gamma}}\Big(2 - \frac{\omega_s L_{M,\Gamma} i^{\mathrm{ref}}_{Rd,\Gamma}(v_s - R_s i^{\mathrm{ref}}_{Rq,\Gamma})}{v_s^2}\Big)p$$
$$+ \frac{R_s^2}{L_{M,\Gamma}^2} - \frac{R_s^2 \omega_s i^{\mathrm{ref}}_{Rd,\Gamma}}{L_{M,\Gamma} v_s} + \Big(1 + \frac{(R_s i^{\mathrm{ref}}_{Rq,\Gamma})^2 - R_s i^{\mathrm{ref}}_{Rq,\Gamma} v_s}{v_s^2}\Big)\omega_s^2.$$

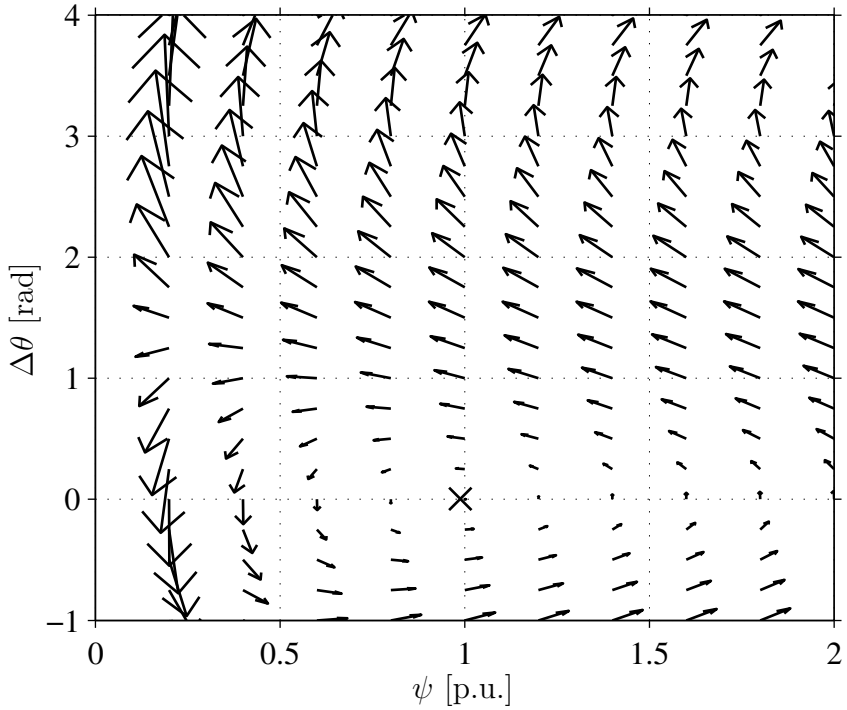

Figure 5.12: Phase portrait of the flux dynamics. The rotor current's d component, $i_{Rd,\Gamma}$, is set to -0.5 p.u. and the q component, $i_{Rq,\Gamma}$, is set to 0.5 p.u. The equilibrium point is marked with "x".

The above characteristic polynomial uses a second-order Taylor series expansion around $R_s = 0$. For a first-order Taylor series expansion around $R_s = 0$ the characteristic polynomial is reduced to

$$p^2 + \frac{R_s}{L_{M,\Gamma}}\Big(2 - \frac{\omega_s L_{M,\Gamma} i^{\text{ref}}_{Rd,\Gamma}}{v_s}\Big)p + \Big(1 - \frac{R_s i^{\text{ref}}_{Rq,\Gamma}}{v_s}\Big)\omega_s^2. \tag{5.59}$$

There are two poorly damped eigenvalues[1] where the oscillating frequency is close to the line frequency, ω_s, as concluded in [29]. In order for the system to be stable the following constraint, which is similar to what can be found in [6, 29], can be set on $i^{\text{ref}}_{Rd,\Gamma}$:

$$i^{\text{ref}}_{Rd,\Gamma} < \frac{2v_s^2}{\omega_s L_{M,\Gamma}(v_s - R_s i^{\text{ref}}_{Rq,\Gamma})} \approx \frac{2v_s}{\omega_s L_{M,\Gamma}}. \tag{5.60}$$

There are different methods of damping the flux oscillations. As mentioned before, one method is to reduce the bandwidth of the current controllers [29]. In [72], a feedback of the derivative of flux was introduced in order to improve the damping of the flux. Another possibility is to use an inverter to substitute the star point of the stator winding, i.e., an extra degree of freedom is introduced that can be used to actively damp

[1]When simulating the doubly-fed induction machine in synchronous coordinates, one must be aware of the poorly damped eigenvalues, which can cause instability due to a poor discretization of the induction machine model.

out the flux oscillations, [38].

Kelber in [37] made a comparison of different methods of damping the flux oscillations. The methods are 1) reducing the bandwidth of the current control loop, 2) compensation of the transformation angle (to synchronous coordinates), 3) feedback of the derivative of the flux and 4) the method with an inverter substituting the star point in the stator winding. It is concluded in [37] that the method with reducing the bandwidth works quite well, although it has the disadvantage of slowly damping of a grid disturbances. Compensation of the transformation angle method improves the dampening only slightly. Feedback of the flux derivative method performs well and has a low cost; the disadvantage of this method is that the method cause relatively high rotor currents. The method with an inverter in the star point of the stator winding performs very well, but the disadvantage with this method is the required addition in hardware and software. Since there is a need for another inverter the cost is also very high.

5.4 Sensorless Operation

With "sensorless" operation, implies, in this thesis, that the rotor position is not measured. This means that the stator frequency, ω_1, and the slip frequency, ω_2, and their corresponding angles, θ_1 and θ_2, must be estimated. Note that if no stator variables exist in the control law, it might be unnecessary to estimate ω_1.

5.4.1 Estimation of θ_1

For a system which is oriented with the stator voltage, or the voltage drop across the stator resistance is negligible, the angle θ_1 can easily be found from measurement of the stator voltage. For a stator-flux-oriented control of the doubly-fed induction machine, where the voltage drop across the stator resistance can not be neglected, the stator flux can be estimated in stator coordinates using (5.16) as [33, 39]

$$\hat{\mathbf{\Psi}}_s^s = \int (\mathbf{v}_s^s - \hat{R}_s \mathbf{i}_s^s) \mathrm{d}t \tag{5.61}$$

and the estimate of the transformation angle, θ_1, can then be found from $\hat{\theta}_1 = \arg \hat{\mathbf{\Psi}}_s^s$. The sign " $\hat{}$ " is used for estimated variables and parameters. Since, the estimator in (5.61) is an open-loop integration, it is marginally stable, i.e, it has to be modified in order to gain stability. This could be done by replacing the open-loop integration with a low-pass filter [25]. It is also possible to estimate the transformation angle in synchronous coordinates. Starting with the stator voltage equation in stator coordinates and taking into account that for a stator-flux-oriented system $\mathbf{\Psi}_s^s = \psi_s \mathrm{e}^{\mathrm{j}\,\theta_1}$ yields

$$\mathbf{v}_s^s = R_s \mathbf{i}_s^s + \frac{\mathrm{d}\mathbf{\Psi}_s^s}{\mathrm{d}t} = R_s \mathbf{i}_s^s + \frac{\mathrm{d}\psi_s}{\mathrm{d}t} \mathrm{e}^{\mathrm{j}\,\theta_1} + \mathrm{j}\,\omega_1 \psi_s \mathrm{e}^{\mathrm{j}\,\theta_1}. \tag{5.62}$$

If $\mathbf{v}_s^s = \mathbf{v}_s e^{j\hat{\theta}_1}$ and $\mathbf{i}_s^s = \mathbf{i}_s e^{j\hat{\theta}_1}$ the above equation can be rewritten in synchronous coordinates as

$$\mathbf{v}_s = R_s \mathbf{i}_s + \frac{d\psi_s}{dt} e^{j\tilde{\theta}_1} + j\omega_1 \psi_s e^{j\tilde{\theta}_1} \tag{5.63}$$

where $\tilde{\theta}_1 = \theta_1 - \hat{\theta}_1$ is the estimation error. Taking the real part of the above equation and neglecting the flux dynamics yields

$$v_{sd} = R_s i_{sd} - \omega_1 \psi_s \sin(\tilde{\theta}_1) \tag{5.64}$$

Now it is possible to form an error signal, suitable for a phase locked loop (PLL)-type estimator, as

$$\epsilon = \sin(\theta_1 - \hat{\theta}_1) = \sin(\tilde{\theta}_1) = -\frac{v_{sd} - \hat{R}_s i_{sd}}{\omega_1 \psi_s} \approx -\frac{v_{sd} - \hat{R}_s i_{sd}}{v_s} \tag{5.65}$$

where the approximation is due to the fact that the stator is directly connected to the grid so $\omega_1 \psi_{M,\Gamma} \approx v_s$. The flux frequency PLL-type estimator is then given by

$$\frac{d\hat{\omega}_1}{dt} = \gamma_1 \epsilon \tag{5.66}$$

$$\frac{d\hat{\theta}_1}{dt} = \hat{\omega}_1 + \gamma_2 \epsilon \tag{5.67}$$

where γ_1 and γ_2 are gain parameters. If the true stator frequency and position are given by $\frac{d\omega_1}{dt} = 0$ and $\frac{d\theta_1}{dt} = \omega_1$, then it is shown in [27] that the estimation error equations for $\tilde{\omega}_1 = \omega_1 - \hat{\omega}_1$ and $\tilde{\theta}_1 = \theta_1 - \hat{\theta}_1$ are asymptotic stable if $\{\gamma_1, \gamma_2\} > 0$. This implies that $\hat{\omega}_1$ and $\hat{\theta}_1$ will converge to ω_1 and θ_1 respectively asymptotically. If the difference $\theta_1 - \hat{\theta}_1$ is small, it is possible to approximate $\sin(\theta_1 - \hat{\theta}_1) \approx \theta_1 - \hat{\theta}_1$, and the following characteristic polynomial, of the system described by (5.66) and (5.67), can be found

$$p^2 + \gamma_2 p + \gamma_1. \tag{5.68}$$

If the parameters are chosen as

$$\gamma_1 = \rho^2 \qquad \gamma_2 = 2\rho \tag{5.69}$$

then ρ can be adjusted to the desired bandwidth of the PLL-type estimator.

5.4.2 Estimation of θ_2

In the literature are, at least, two methods to perform sensorless operation. In the first method a set of variables is estimated or measured in one reference frame and then the variables are used in another reference frame to estimate the slip angle θ_2. This can be done by estimating the rotor currents from the flux and the stator currents. In [10] the estimation of the rotor currents have been carried out in stator coordinates while in [33, 44] it have been done in synchronous coordinates. The method will

here be described in synchronous coordinates. Starting with the stator flux, which, in synchronous coordinates, is given by

$$\mathbf{\Psi}_s = \psi_s = L_{M,\Gamma}(\mathbf{i}_s + \mathbf{i}_{R,\Gamma}) \tag{5.70}$$

and since the stator flux is known, i.e., it is to a great extent determined by the stator voltage, it is possible to use the above-mentioned equation to estimate the rotor current, i.e.,

$$\hat{\mathbf{i}}_{R,\Gamma} = \frac{\hat{\psi}_s}{\hat{L}_{M,\Gamma}} - \mathbf{i}_s \tag{5.71}$$

where the stator current has been measured and transformed with the transformation angle θ_1; see previous section for determination of this angle. The magnitude of the stator flux can be estimated as $\hat{\psi}_s = v_s/\omega_1$ [33]. Then, if the rotor current is measured in rotor coordinates the estimate of the slip angle can be found as

$$\hat{\theta}_2 = \arg \mathbf{i}^r_{R,\Gamma} - \arg \hat{\mathbf{i}}_{R,\Gamma}. \tag{5.72}$$

The second method is based on determining the slip frequency by the rotor circuit equation. In [39] a stator-flux-oriented sensorless control using the rotor voltage circuit equation is proposed. The rotor voltage equation is given by

$$\mathbf{v}_{R,\Gamma} = R_{R,\Gamma}\mathbf{i}_{R,\Gamma} + \frac{\mathrm{d}\mathbf{\Psi}_{R,\Gamma}}{\mathrm{d}t} + \mathrm{j}\,\omega_2 \mathbf{\Psi}_{R,\Gamma} \tag{5.73}$$

neglecting the derivative of the flux, the slip frequency, ω_2, can be estimated from the imaginary part of the above equation as

$$\hat{\omega}_2 = \frac{v_{Rq,\Gamma} - \hat{R}_{R,\Gamma} i_{Rq,\Gamma}}{\psi_{Rd,\Gamma}} = \frac{v_{Rq,\Gamma} - \hat{R}_{R,\Gamma} i_{Rq,\Gamma}}{\psi_s + \hat{L}_{\sigma,\Gamma} i_{sd}}. \tag{5.74}$$

Then, the estimate of the slip angle, $\hat{\theta}_2$, can be found from integration of the estimate of the slip frequency, $\hat{\omega}_2$, as

$$\hat{\theta}_2 = \int \hat{\omega}_2 \mathrm{d}t. \tag{5.75}$$

5.5 Torque and Speed Control of the Doubly-Fed Induction Machine

5.5.1 Torque Control

The electromechanical torque can be found from (5.22). Assuming perfect field orientation, i.e., $\mathbf{\Psi}_s = \psi_s$, the electromechanical torque can be found as

$$T_e = -3n_p \psi_s i_{Rq,\Gamma}. \tag{5.76}$$

Since the stator flux, ψ_s, is almost fixed to the stator voltage, the torque can be controlled by the q component of the rotor current, $i_{Rq,\Gamma}$. Since it is difficult to measure the torque, it is most often controlled in an open-loop manner. Therefore, the q component reference current, $i_{Rq,\Gamma}^{\text{ref}}$, can be determined from the reference torque, T_e^{ref}, as

$$i_{Rq,\Gamma}^{\text{ref}} = -\frac{T_e^{\text{ref}}}{3n_p\psi_s}. \tag{5.77}$$

Instead of using the actual flux in (5.77), the approximation in (5.57) can be used

$$\psi_s \approx \frac{v_s + R_s i_{Rq,\Gamma}^{\text{ref}}}{\omega_s} - \frac{R_s^2(v_s - \omega_s L_{M,\Gamma} i_{Rd,\Gamma}^{\text{ref}})^2}{2L_{M,\Gamma}^2 v_s \omega_s^3} \approx \frac{v_s + R_s i_{Rq,\Gamma}^{\text{ref}}}{\omega_s} \approx \frac{v_s}{\omega_s}. \tag{5.78}$$

Figure 5.13 shows a block diagram of the open-loop torque control scheme.

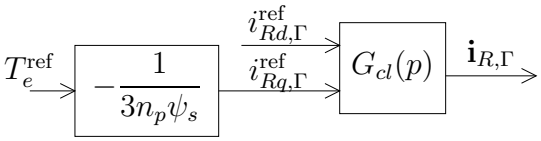

Figure 5.13: Block diagram of the torque control system.

5.5.2 Speed Control

Since the current dynamics, i.e., with the bandwidth α_c, should be set much faster than the speed dynamics, the speed can be controlled in cascade with the current. The mechanical dynamic is described by (5.15) as

$$\frac{J}{n_p}\frac{\mathrm{d}\omega_r}{\mathrm{d}t} = T_e - T_s \tag{5.79}$$

where T_e is the electromechanical torque and T_s is the shaft torque. The electromechanical torque can be expressed, under the assumption that the current dynamics is much faster, as

$$T_e = T_e^{\text{ref}}$$

where the reference torque is set to

$$T_e^{\text{ref}} = T_e'^{\text{ref}} - B_a\omega_r$$

where an "active damping" term, B_a, is introduced. This is an inner feedback loop [28]. Its transfer function, treating the shaft torque, T_s, as a disturbance, now becomes

$$H(p) = \frac{\omega_r(p)}{T_e'^{\text{ref}}(p)} = \frac{1}{\frac{J}{n_p}p + B_a}.$$

Using internal model control, as described in Section 5.2.2, yields in following proportional, k_{ps}, and integral, k_{is} gains, of the controller:

$$k_{ps} = \alpha_s \frac{J}{n_p} \qquad k_{is} = \alpha_s B_a$$

where α_s is the desired closed-loop bandwidth of the speed control loop. The closed-loop dynamic is then described by

$$H_{cl}(p) = \frac{\alpha_s}{p + \alpha_s}.$$

Figure 5.14 shows a block diagram of the speed control system. In the figure, $D(p)$ describes disturbances, i.e., in this case the shaft torque, T_s.

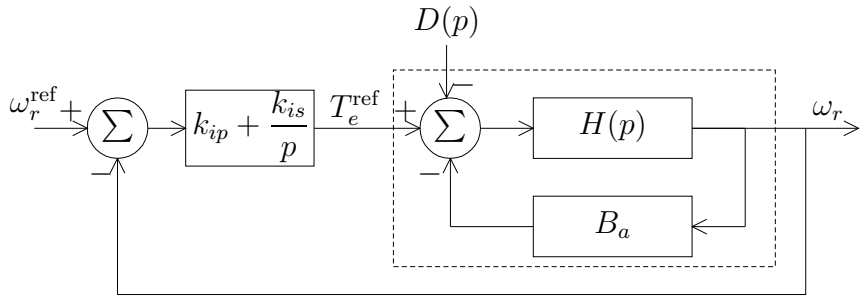

Figure 5.14: Block diagram of the speed control system.

5.5.3 Choosing the "Active Damping"

The transfer function from a disturbance, $D(p)$, to the rotational speed can be described by, see Figure 5.14,

$$\frac{\omega_r(p)}{D(p)} = \frac{p}{\frac{J}{n_p}p^2 + (B_a + k_{ps})p + k_{is}}$$

if the active damping is chosen as $B_a = \frac{J}{n_p}\alpha_s$ we get

$$\frac{\omega_r(p)}{D(p)} = \frac{p}{\frac{J}{n_p}(p + \alpha_s)^2}$$

i.e., a disturbance, $D(p)$, is damped with the same time constant as the bandwidth of the speed control loop.

5.5.4 Evaluation

Figure 5.15 shows a simulation of the speed control loop with a constant driving torque of approximately 40 % of rated torque (note that the stator voltage is lower than the rated voltage, which means that the maximum torque is approximately 60 % of rated).

The bandwidth of the current control loop is set to 1.4 p.u., the flux damping, α_d, is set to 0.14 p.u., and the bandwidth of the speed control loop, α_s, is set to 0.014 p.u. A bandwidth of 1.4 p.u. corresponds to a rise time of 5 ms and 0.014 p.u. corresponds to 0.5 s. Initially the speed reference is set to 1 p.u., after 3 s it is changed to 0.75 p.u., after 6 s it is changed to 1.25 p.u., and after 9 s the reference is ramped down during 3 s to 1 p.u. Figure 5.16 shows the corresponding measurement. The driving torque has been produced by a dc machine connected to the induction machine's shaft. The torque presented in the figure has been calculated from measured data. The data of the measurement have been sampled with 2 kHz and low-pass filtered with a cut-off frequency of 500 Hz. It can be seen in the simulation and in the measurement that the current limit of the current controller has been reached. This causes the rise time of the rotor speed to be longer than the ideal.

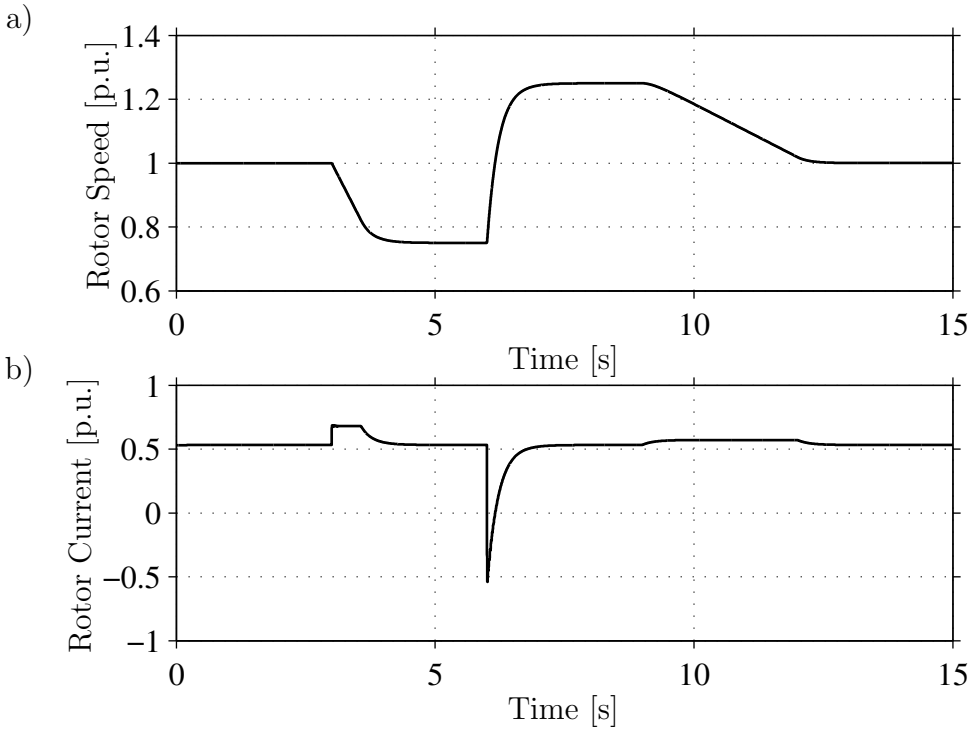

Figure 5.15: Simulations of speed control with a driving torque. a) The rotational speed, ω_r. b) The q-component rotor current, $i_{Rq,\Gamma}$.

5.6 Reactive Power Control

The reactive power can be controlled with the d component of the rotor current, since (5.18) can be rewritten using (5.20) as

$$\mathbf{v}_s = -R_s \mathbf{i}_{R,\Gamma} + \frac{\mathrm{d}\boldsymbol{\Psi}_s}{\mathrm{d}t} + \left(\frac{R_s}{L_{M,\Gamma}} + \mathrm{j}\omega_1\right)\boldsymbol{\Psi}_s. \tag{5.80}$$

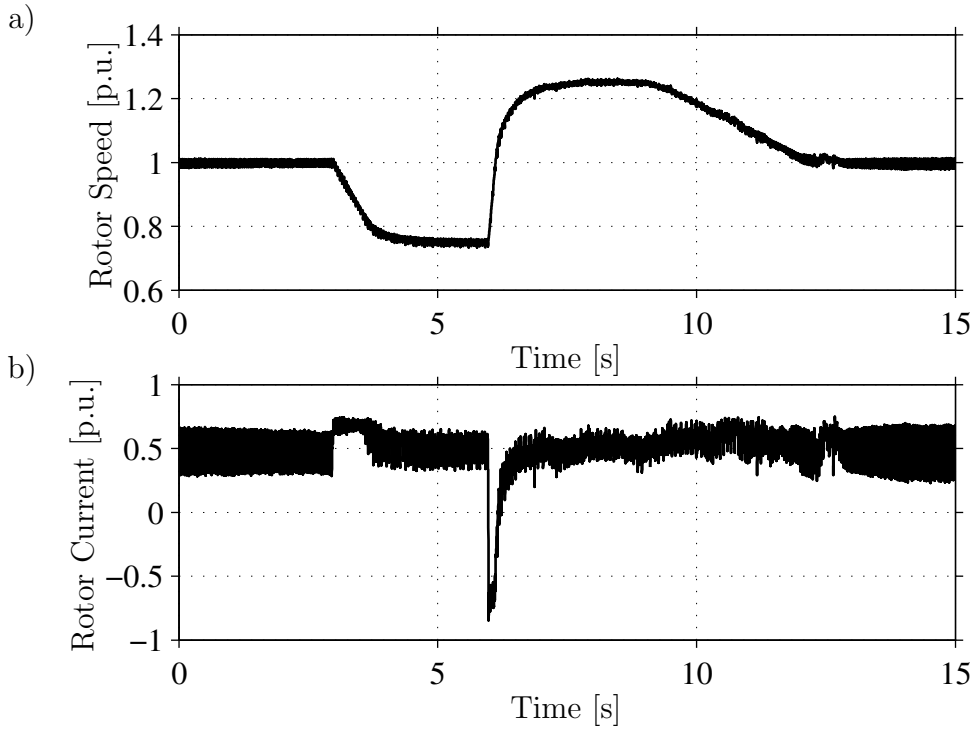

Figure 5.16: Measurements of speed control with a driving torque. a) The rotational speed, ω_r. b) The q-component rotor current, $i_{Rq,\Gamma}$.

The apparent power, $\mathbf{S}$, can be found from

$$\mathbf{S} = 3\mathbf{v}_s\mathbf{i}_s^* = 3\Big(\mathbf{v}_s\frac{\mathbf{\Psi}_s^*}{L_{M,\Gamma}} - \mathbf{v}_s\mathbf{i}_{R,\Gamma}^*\Big) \tag{5.81}$$

which can be expressed as

$$\begin{aligned}\mathbf{S} = \; & 3\Big[-R_s\mathbf{i}_{R,\Gamma} + \frac{\mathrm{d}\mathbf{\Psi}_s}{\mathrm{d}t} + \Big(\frac{R_s}{L_{M,\Gamma}} + \mathrm{j}\,\omega_1\Big)\mathbf{\Psi}_s\Big]\frac{\mathbf{\Psi}_s^*}{L_{M,\Gamma}} \\ & -3\Big[-R_s\mathbf{i}_{R,\Gamma} + \frac{\mathrm{d}\mathbf{\Psi}_s}{\mathrm{d}t} + \Big(\frac{R_s}{L_{M,\Gamma}} + \mathrm{j}\,\omega_1\Big)\mathbf{\Psi}_s\Big]\mathbf{i}_{R,\Gamma}^*\end{aligned} \tag{5.82}$$

neglecting the derivatives of the flux, assuming stator-flux orientation, i.e., $\mathbf{\Psi}_s = \psi_s$. With $\mathbf{S} = P + \mathrm{j}\,Q$ we have

$$P = 3\Big[R_s|\mathbf{i}_{R,\Gamma}|^2 + \frac{R_s\psi_s}{L_{M,\Gamma}}\Big(\frac{\psi_s}{L_{M,\Gamma}} - 2i_{Rd,\Gamma}\Big) - \omega_1\psi_s i_{Rq,\Gamma}\Big] \tag{5.83}$$

$$Q = 3\omega_1\psi_s\Big(\frac{\psi_s}{L_{M,\Gamma}} - i_{Rd,\Gamma}\Big). \tag{5.84}$$

Note that the power, P, given above is the power at the stator terminals of the doubly-fed induction motor and not the total power that is consumed in the induction machine. The active and reactive power at the rotor terminals can be expressed as (derived in a similar way and neglecting derivatives)

$$P_r = 3\Big(R_{R,\Gamma}|\mathbf{i}_{R,\Gamma}|^2 + \omega_2\psi_s i_{Rq,\Gamma}\Big) \tag{5.85}$$

$$Q_r = 3\Big(\omega_2 L_{\sigma,\Gamma}|\mathbf{i}_{R,\Gamma}|^2 + \omega_2\psi_s i_{Rd,\Gamma}\Big). \tag{5.86}$$

It is assumed that the dc-link capacitor is large enough to generate the reactive power that is fed via rotor terminals. If the d component of the rotor current is controlled as

$$i_{Rd,\Gamma}^{\text{ref}} = \frac{\psi_s}{L_{M,\Gamma}} \tag{5.87}$$

unity power factor at the stator is achieved.

Chapter 6

Evaluation of Control Laws for Doubly-Fed Induction Machines

6.1 Current Control of Doubly-Fed Induction Machines

In this section the Γ model of the induction machine will be derived in synchronous coordinates with the assumption that the transformation between the coordinate systems is not perfect, i.e., there is a transformation error.

The stator equation (in stator coordinates) and rotor equation (in rotor coordinates) for the Γ representation of the induction machine can be expressed as

$$\mathbf{v}_s^s = R_s \mathbf{i}_s^s + \frac{\mathrm{d}\boldsymbol{\Psi}_s^s}{\mathrm{d}t} \tag{6.1}$$

$$\mathbf{v}_{R,\Gamma}^r = R_{R,\Gamma} \mathbf{i}_{R,\Gamma}^r + \frac{\mathrm{d}\boldsymbol{\Psi}_{R,\Gamma}^r}{\mathrm{d}t} \tag{6.2}$$

where the fluxes are given by

$$\boldsymbol{\Psi}_s^s = L_{M,\Gamma}(\mathbf{i}_s^s + \mathbf{i}_{R,\Gamma}^r \mathrm{e}^{\mathrm{j}\,\theta_r}) \tag{6.3}$$

$$\boldsymbol{\Psi}_{R,\Gamma}^r = L_{\sigma,\Gamma}\mathbf{i}_{R,\Gamma}^r + L_{M,\Gamma}(\mathbf{i}_s^s \mathrm{e}^{-\mathrm{j}\,\theta_r} + \mathbf{i}_{R,\Gamma}^r) = L_{\sigma,\Gamma}\mathbf{i}_{R,\Gamma}^r + \boldsymbol{\Psi}_s^r. \tag{6.4}$$

Since the stator and rotor circuits "feel" the same flux modulus we can express $\boldsymbol{\Psi}_s^s = \psi_s \mathrm{e}^{\mathrm{j}\,\theta_1}$ and $\boldsymbol{\Psi}_s^r = \psi_s \mathrm{e}^{\mathrm{j}\,\theta_2}$. The angles θ_1 and θ_2 are given as

$$\frac{\mathrm{d}\theta_1}{\mathrm{d}t} = \omega_1 \qquad \frac{\mathrm{d}\theta_2}{\mathrm{d}t} = \omega_2 \tag{6.5}$$

where ω_1 is the frequency by which the flux passes through the stator windings and ω_2 is the frequency (slip frequency) by which that the flux passes through the rotor windings. The stator and rotor equations can be now be expressed as

$$\mathbf{v}_s^s = R_s \mathbf{i}_s^s + \frac{\mathrm{d}\psi_s}{\mathrm{d}t}\mathrm{e}^{\mathrm{j}\,\theta_1} + \mathrm{j}\,\frac{\mathrm{d}\theta_1}{\mathrm{d}t}\psi_s \mathrm{e}^{\mathrm{j}\,\theta_1} \tag{6.6}$$

$$\mathbf{v}_{R,\Gamma}^r = R_{R,\Gamma}\mathbf{i}_{R,\Gamma}^r + L_{\sigma,\Gamma}\frac{\mathrm{d}\mathbf{i}_{R,\Gamma}^r}{\mathrm{d}t} + \frac{\mathrm{d}\psi_s}{\mathrm{d}t}\mathrm{e}^{\mathrm{j}\,\theta_2} + \mathrm{j}\,\frac{\mathrm{d}\theta_2}{\mathrm{d}t}\psi_s \mathrm{e}^{\mathrm{j}\,\theta_2}. \tag{6.7}$$

To be able to transform the stator and the rotor equations to synchronous coordinates, the following transformations can be applied:

$$\mathbf{i}_s^s = \mathbf{i}_s \mathrm{e}^{\mathrm{j}\,\hat{\theta}_1} \qquad \mathbf{i}_{R,\Gamma}^r = \mathbf{i}_{R,\Gamma} \mathrm{e}^{\mathrm{j}\,\hat{\theta}_2} \qquad \mathbf{v}_{R,\Gamma}^r = \mathbf{v}_{R,\Gamma} \mathrm{e}^{\mathrm{j}\,\hat{\theta}_2} \tag{6.8}$$

where $\hat{\theta}_1$ and $\hat{\theta}_2$ are estimates of θ_1 and θ_2, respectively. Using these transformations yields

$$\mathbf{v}_s^s \mathrm{e}^{-\mathrm{j}\,\hat{\theta}_1} = R_s \mathbf{i}_s + \frac{\mathrm{d}\psi_s}{\mathrm{d}t} \mathrm{e}^{\mathrm{j}\,\tilde{\theta}_1} + \mathrm{j}\,\frac{\mathrm{d}\theta_1}{\mathrm{d}t} \psi_s \mathrm{e}^{\mathrm{j}\,\tilde{\theta}_1} \tag{6.9}$$

$$\mathbf{v}_{R,\Gamma} = (R_{R,\Gamma} + \mathrm{j}\,\hat{\omega}_2 L_{\sigma,\Gamma}) \mathbf{i}_{R,\Gamma} + L_{\sigma,\Gamma} \frac{\mathrm{d}\mathbf{i}_{R,\Gamma}}{\mathrm{d}t} + \frac{\mathrm{d}\psi_s}{\mathrm{d}t} \mathrm{e}^{\mathrm{j}\,\tilde{\theta}_2} + \mathrm{j}\,\frac{\mathrm{d}\theta_2}{\mathrm{d}t} \psi_s \mathrm{e}^{\mathrm{j}\,\tilde{\theta}_2} \tag{6.10}$$

where $\tilde{\theta}_1 = \theta_1 - \hat{\theta}_1$ and $\tilde{\theta}_2 = \theta_2 - \hat{\theta}_2$. Further, the applied stator voltage as can be described as

$$\mathbf{v}_s^s = \mathrm{j}\, v_s \mathrm{e}^{\mathrm{j}\,\theta_s} \tag{6.11}$$

where θ_s is the angle of the applied angular frequency of the grid. The stator current can be expressed as

$$\mathbf{i}_s^s = \frac{\boldsymbol{\Psi}_s^s}{L_{M,\Gamma}} - \mathbf{i}_{R,\Gamma}^r \mathrm{e}^{\mathrm{j}\,\theta_r} = \frac{\psi_s \mathrm{e}^{\mathrm{j}\,\theta_1}}{L_{M,\Gamma}} - \mathbf{i}_{R,\Gamma} \mathrm{e}^{\mathrm{j}\,\hat{\theta}_2} \mathrm{e}^{\mathrm{j}\,\theta_r} \tag{6.12}$$

or in synchronous coordinates as

$$\mathbf{i}_s = \frac{\psi_s}{L_{M,\Gamma}} \mathrm{e}^{\mathrm{j}\,\tilde{\theta}_1} - \mathbf{i}_{R,\Gamma} \mathrm{e}^{\mathrm{j}\,\tilde{\theta}_r} \tag{6.13}$$

where $\tilde{\theta}_r$ is the estimation error of the rotor angle, θ_r. Eliminating the stator current, $\mathbf{i}_s^s$, from the above equations, the system can be expressed as

$$\frac{\mathrm{d}\psi_s}{\mathrm{d}t} = -v_s \sin(\theta_s - \theta_1) + R_s \Big(i_{Rd,\Gamma} \cos\tilde{\theta}_2 + i_{Rq,\Gamma} \sin\tilde{\theta}_2 \Big) - \frac{R_s}{L_{M,\Gamma}} \psi_s \tag{6.14}$$

$$\frac{\mathrm{d}\theta_1}{\mathrm{d}t} = \frac{v_s \cos(\theta_s - \theta_1) - R_s \Big(i_{Rd,\Gamma} \sin\tilde{\theta}_2 - i_{Rq,\Gamma} \cos\tilde{\theta}_2 \Big)}{\psi_s} \tag{6.15}$$

$$L_{\sigma,\Gamma} \frac{\mathrm{d}\mathbf{i}_{R,\Gamma}}{\mathrm{d}t} = \mathbf{v}_{R,\Gamma} - (R_{R,\Gamma} + R_s + \mathrm{j}\,\hat{\omega}_2 L_{\sigma,\Gamma}) \mathbf{i}_{R,\Gamma} - \mathbf{E} \tag{6.16}$$

where the flux dynamics have been divided into real and imaginary parts. The back emf, $\mathbf{E}$, is described by

$$\mathbf{E} = \Big[\mathrm{j}\, v_s \mathrm{e}^{\mathrm{j}\,(\theta_s - \theta_1)} - \Big(\frac{R_s}{L_{M,\Gamma}} + \mathrm{j}\,\omega_r \Big) \psi_s \Big] \mathrm{e}^{\mathrm{j}\,\tilde{\theta}_2}. \tag{6.17}$$

6.1.1 Current Control with Feed-Forward of the Back EMF

In Section 5.3.1 the tracking error was eliminated with feed-forward of the back emf. However, oscillations in the d component rotor current could be seen for some bandwidths of the current control loop. Since in (6.16) the derivative of the flux has been

eliminated (which was neglected in Section 5.3.1) it is possible to include the entire back emf in the feed-forward compensation term, i.e.,

$$\mathbf{v}_{R,\Gamma} = \mathbf{v}'_{R,\Gamma} + \mathrm{j}\,\omega_2 L_{\sigma,\Gamma}\mathbf{i}_{R,\Gamma} + \mathrm{j}\,v_s \mathrm{e}^{\mathrm{j}\,(\theta_s-\theta_1)} - \Big(\frac{R_s}{L_{M,\Gamma}} + \mathrm{j}\,\omega_r\Big)\psi_s \tag{6.18}$$

where the term $\mathrm{j}\,\omega_2 L_{\sigma,\Gamma}\mathbf{i}_{R,\Gamma}$ decouples the d and q components of the rotor current. The back emf is found from (6.17) with the assumption of perfect field orientation, i.e., $\tilde{\theta}_2 = 0$. The rotor current dynamics in (6.16) can now be expressed as

$$\mathbf{v}'_{R,\Gamma} = (R_{R,\Gamma} + R_s)\mathbf{i}_{R,\Gamma} + L_{\sigma,\Gamma}\frac{\mathrm{d}\mathbf{i}_{R,\Gamma}}{\mathrm{d}t}. \tag{6.19}$$

The transfer function from the rotor voltage, $\mathbf{v}'_{R,\Gamma}$, to the rotor current, $\mathbf{i}_{R,\Gamma}$, can be found as

$$G(p) = \frac{1}{pL_{\sigma,\Gamma} + R_{R,\Gamma} + R_s}. \tag{6.20}$$

Using IMC (see Section 5.2.2) to design the current controllers yields

$$F(p) = k_p + \frac{k_i}{p} = \frac{\alpha_c}{p}G^{-1}(p) \tag{6.21}$$

where the proportional gain, k_p, and the integral gain, k_i, become

$$k_p = \alpha_c L_{\sigma,\Gamma} \qquad k_i = \alpha_c(R_{R,\Gamma} + R_s). \tag{6.22}$$

6.1.2 Current Control with "Active Resistance"

It is also possible to introduce an extra term, called "active resistance," R_a, that can be used to damp out variations in the back emf faster. Similar approaches with the "active resistance" have been done for stator-fed induction machines [11, 28]. The rotor voltage should be chosen as

$$\mathbf{v}_{R,\Gamma} = \mathbf{v}'_{R,\Gamma} + (\mathrm{j}\,\hat{\omega}_2 L_{\sigma,\Gamma} - R_a)\mathbf{i}_{R,\Gamma}. \tag{6.23}$$

The current dynamics in (6.16) can now be rewritten as

$$L_{\sigma,\Gamma}\frac{\mathrm{d}\mathbf{i}_{R,\Gamma}}{\mathrm{d}t} = \mathbf{v}'_{R,\Gamma} - (R_{R,\Gamma} + R_s + R_a)\mathbf{i}_{R,\Gamma} - \mathbf{E}$$

where $\mathbf{E}$ is the back emf in (6.17). Under the assumption that the back emf is constant (or at least varying slowly), we can treat it as a disturbance which can be eliminated with integral action. Thus, the transfer function from $\mathbf{i}_{R,\Gamma}$ to $\mathbf{v}'_{R,\Gamma}$ can be expressed as

$$G(p) = \frac{1}{pL_{\sigma,\Gamma} + R_{R,\Gamma} + R_s + R_a}.$$

See Figure 6.1 for a block diagram of the current control system. Using IMC for designing the current controllers as described in Section 5.2.2 will yield in the following proportional, k_p, and integral, k_i, gains:

$$k_p = \alpha_c L_{\sigma,\Gamma} \qquad k_i = \alpha_c(R_{R,\Gamma} + R_s + R_a)$$

where α_c is closed-loop bandwidth of the current dynamics.

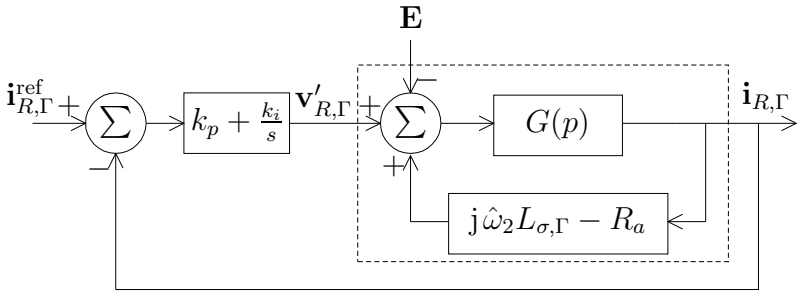

Figure 6.1: Block diagram of the current control system.

Choosing the "Active Resistance"

In this section we will discuss how to choose the introduced active resistance, R_a. The transfer function from the back emf, $\mathbf{E}$, to the current, $\mathbf{i}_{R,\Gamma}$, cf. Figure 6.1, becomes

$$\frac{\mathbf{I}_{R,\Gamma}}{\mathbf{E}} = -\frac{p}{L_{\sigma,\Gamma}p^2 + (R_{R,\Gamma} + R_s + R_a + k_p)p + k_i}. \tag{6.24}$$

Inserting the proportional and integral gains and letting the active resistance equal $R_a = \alpha_c L_{\sigma,\Gamma} - R_{R,\Gamma} - R_s$ yields

$$\frac{\mathbf{I}_{R,\Gamma}}{\mathbf{E}} = -\frac{p}{L_{\sigma,\Gamma}p^2 + 2\alpha_c L_{\sigma,\Gamma}p + \alpha_c^2 L_{\sigma,\Gamma}} = -\frac{p}{L_{\sigma,\Gamma}(p+\alpha_c)^2} \tag{6.25}$$

and a change in the back emf will be damped out with the same bandwidth as the closed-loop current dynamics. Since the active resistance is chosen as $R_a = \alpha_c L_{\sigma,\Gamma} - R_{R,\Gamma} - R_s$ and has to be greater than zero, the minimum bandwidth of the current control loop when using an active resistance becomes

$$\alpha_{c,\min} = \frac{R_{R,\Gamma} + R_s}{L_{\sigma,\Gamma}}. \tag{6.26}$$

6.1.3 Current Control with Feed-Forward of the Back EMF and "Active Resistance"

Combining the method with active resistance presented in Section 6.1.2 with feed-forward of the back emf presented in Section 6.1.1, implies choosing the rotor voltage as

$$\mathbf{v}_{R,\Gamma} = \mathbf{v}'_{R,\Gamma} + (\mathrm{j}\hat{\omega}_2 L_{\sigma,\Gamma} - R_a)\mathbf{i}_{R,\Gamma} + \mathbf{v}_s - \Big(\frac{R_s}{L_{M,\Gamma}} + \mathrm{j}\omega_r\Big)\psi_s. \tag{6.27}$$

The active resistance, R_a, can be chosen as described in Section 6.1.2. Since the current dynamics are

$$L_{\sigma,\Gamma}\frac{\mathrm{d}\mathbf{i}_{R,\Gamma}}{\mathrm{d}t} = \mathbf{v}'_{R,\Gamma} - (R_{R,\Gamma} + R_s + R_a)\mathbf{i}_{R,\Gamma}$$

the proportional and integral gains become as in Section 6.1.2.

6.1.4 Stability Analysis using the Proposed Current Control Laws

In Section 5.3.2 a stability analysis was made using the assumption that the current dynamics are much faster than the dynamics of the back emf, i.e., the flux dynamics. If the bandwidth of the current control loop is not set much higher than the dynamics of the back emf, the current dynamics can not be neglected in the stability analysis. The rotational speed is assumed to be varying slowly and is therefore treated as a constant. Consider the system described by (6.14)–(6.16). Perfect field orientation is assumed, i.e., $\tilde{\theta}_2 = 0$. Then the following system has to be analyzed:

$$\frac{\mathrm{d}\mathbf{I}}{\mathrm{d}t} = \mathbf{e} \tag{6.28}$$

$$\frac{\mathrm{d}\psi_s}{\mathrm{d}t} = -\frac{R_s}{L_{M,\Gamma}}\psi_s - v_s \sin(\Delta\theta) + R_s i_{Rd,\Gamma} \tag{6.29}$$

$$\frac{\mathrm{d}\Delta\theta}{\mathrm{d}t} = \omega_s - \frac{v_s \cos(\Delta\theta) + R_s i_{Rq,\Gamma}}{\psi_s} \tag{6.30}$$

$$\frac{\mathrm{d}\mathbf{i}_{R,\Gamma}}{\mathrm{d}t} = \frac{\mathbf{v}_{R,\Gamma} - (R_{R,\Gamma} + R_s + \mathrm{j}\,\omega_2 L_{\sigma,\Gamma})\mathbf{i}_{R,\Gamma} + \mathrm{j}\,v_s \mathrm{e}^{\mathrm{j}\,\Delta\theta} + (\frac{R_s}{L_{M,\Gamma}} + \mathrm{j}\,\omega_r)\psi_s}{L_{\sigma,\Gamma}} \tag{6.31}$$

where $\mathbf{I}$ is the integration variable in the control law and $\mathbf{e} = \mathbf{i}^{\mathrm{ref}}_{R,\Gamma} - \mathbf{i}_{R,\Gamma}$ is the control error. In (6.31) the chosen control law has to be inserted. Note that (6.28) and (6.31) are complex-valued equations while (6.29) and (6.30) are real-valued equations. In the following three subsections, stability analysis of three control laws, presented above, will be performed.

Feed-Forward of the Back EMF

In order to analyze the stability of the method with feed-forward of the back emf, the control law in (6.18) has to be inserted in (6.31). Linearization of the non-linear system described by (6.28)–(6.31) and insertion of the equilibrium point, the characteristic polynomial can be found. A first-order Taylor series expansion of the characteristic polynomial with respect to the stator resistance, R_s (around $R_s = 0$) yields

$$(p + \alpha_c)^2 \Big(p + \frac{R_{R,\Gamma}}{L_{\sigma,\Gamma}}\Big)(p^3 + c_2 p^2 + c_1 p + c_0). \tag{6.32}$$

The system has at least three real-valued poles, two located at $-\alpha_c$ and one at $-R_{R,\Gamma}/L_{\sigma,\Gamma}$. The coefficients in the third-order polynomial become

$$c_2 = \frac{2R_s}{L_{M,\Gamma}} + \frac{R_{R,\Gamma} + 2R_s}{L_{\sigma,\Gamma}} - \frac{i^{\mathrm{ref}}_{Rd,\Gamma} R_s \omega_s}{v_s} \tag{6.33}$$

$$c_1 = \frac{(v_s - i^{\mathrm{ref}}_{Rq,\Gamma} R_s)\omega_s^2}{v_s} + \frac{R_{R,\Gamma} R_s (2v_s - i^{\mathrm{ref}}_{Rd,\Gamma} L_{M,\Gamma} \omega_s)}{L_{M,\Gamma} L_{\sigma,\Gamma} v_s} \tag{6.34}$$

$$c_0 = \frac{\Big(- i^{\mathrm{ref}}_{Rq,\Gamma} R_{R,\Gamma} R_s + (R_{R,\Gamma} + 2R_s)v_s \Big)\omega_s^2}{L_{\sigma,\Gamma} v_s}. \tag{6.35}$$

As can be seen above, the coefficients are not dependent on the bandwidth of the current control loop, α_c. Since it is complicated, in general, to solve an equation of a third degree analytically, root loci are instead studied, and can be seen in Figure 6.2. The figure shows how the poles move with the d component of the rotor current. As

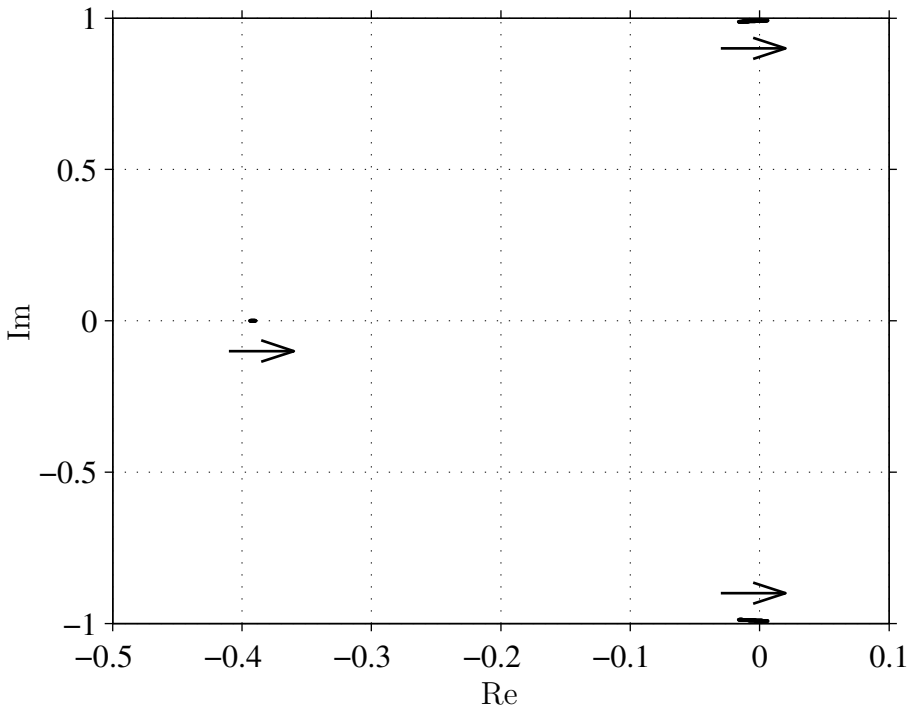

Figure 6.2: Root loci. The arrows show in what directions the poles move with increased $i_{Rd,\Gamma}^{\text{ref}}$.

can be seen in the figure, there are, as concluded in Section 5.3.2, two poorly damped poles. The poorly damped poles move towards instability when the d component rotor current increases.

To investigate the stability of the system, Routh's table can be used [7]. For the above characteristic polynomial, Routh's table can be found in Table 6.1. In order for

Table 6.1: Routh's table.

p^3	1	c_1
p^2	c_2	c_0
p^1	$C = \dfrac{c_2 c_1 - c_0}{c_2}$	0
p^0	0	0

the system to be stable all coefficients in the first column must not change sign. Since the first coefficient in Routh's table is 1, all other coefficients must be positive in order to maintain stability. The expression for the coefficient C becomes quite complex.

Therefore, an approximation of the coefficient can be found as

$$C \approx \frac{R_s(2v_s - L_{M,\Gamma}\omega_s i^{\text{ref}}_{Rd,\Gamma})(R^2_{R,\Gamma} + L^2_{\sigma,\Gamma}\omega_s^2)}{L_{M,\Gamma}L_{\sigma,\Gamma}R_{R,\Gamma}v_s} \tag{6.36}$$

where a first-order Taylor series expansion of the coefficient C with respect to the stator resistance, R_s (around $R_s = 0$), has been carried out. The following constraint can be set on $i^{\text{ref}}_{Rd,\Gamma}$ in order to keep the coefficient c_2 positive

$$i^{\text{ref}}_{Rd,\Gamma} < \frac{v_s}{R_s\omega_s}\Big(\frac{2R_s}{L_{M,\Gamma}} + \frac{R_{R,\Gamma} + 2R_s}{L_{\sigma,\Gamma}}\Big). \tag{6.37}$$

For keeping the coefficient C positive the following constraint has to be set

$$i^{\text{ref}}_{Rd,\Gamma} < \frac{2v_s}{\omega_s L_{M,\Gamma}}. \tag{6.38}$$

The constraint in (6.38) is "harder" than the constraint in (6.37). The constraint in (6.38) can be compared to the constraint in (5.60), i.e.,

$$i^{\text{ref}}_{Rd,\Gamma} < \frac{2v_s^2}{\omega_s L_{M,\Gamma}(v_s - R_s i^{\text{ref}}_{Rq,\Gamma})} \approx \frac{2v_s}{\omega_s L_{M,\Gamma}} \tag{6.39}$$

where the stability analysis, in Section 5.3.2, was performed assuming fast current dynamics. The system consists of two poorly damped poles, caused by the flux dynamics, and the constraint on $i^{\text{ref}}_{Rd,\Gamma}$ relates to the flux dynamics. Therefore, the constraint on $i^{\text{ref}}_{Rd,\Gamma}$, which relates to the flux dynamics, can be found more easily assuming a fast current dynamics. Generally, a full-order analysis is still valuable, if the current dynamics are not fast, since other parameters also may influence the stability.

"Active Resistance"

For the system with the active resistance, R_a, the same dynamic equation as in (6.28) to (6.31) can be analyzed, but the control law has to be modified to

$$\mathbf{v}_{R,\Gamma} = k_p\mathbf{e} + k_i\mathbf{I} + (\mathrm{j}\omega_2 L_{\sigma,\Gamma} - R_a)\mathbf{i}_{R,\Gamma} \tag{6.40}$$

in order include the "active resistance". Linearization and a Taylor expansion of the characteristic polynomial as before yields

$$(p + \alpha_c)^2(p^4 + c_3p^3 + c_2p^2 + c_1p + c_0). \tag{6.41}$$

That is, it consists of at least two real poles located at $-\alpha_c$. The coefficients of the fourth-order polynomial are given by

$$c_3 = 2\alpha_c + \frac{2R_s}{L_{M,\Gamma}} - \frac{i^{\text{ref}}_{Rd,\Gamma} R_s \omega_s}{v_s} \tag{6.42}$$

$$c_2 = \alpha_c^2 + \frac{4\alpha_c R_s}{L_{M,\Gamma}} - \frac{2\alpha_c i^{\text{ref}}_{Rd,\Gamma} R_s \omega_s}{v_s} + \omega_s^2 - \frac{i^{\text{ref}}_{Rq,\Gamma} R_s \omega_s^2}{v_s} \tag{6.43}$$

$$\begin{aligned} c_1 = {} & \frac{2\alpha_c (v_s - R_s i^{\text{ref}}_{Rq,\Gamma})\omega_s^2}{v_s} - \frac{R_s \omega_s (\omega_r + \omega_s)}{L_{\sigma,\Gamma}} \\ & + \frac{\alpha_c^2 R_s (2v_s - i^{\text{ref}}_{Rd,\Gamma} L_{M,\Gamma} \omega_s)}{L_{M,\Gamma} v_s} \end{aligned} \tag{6.44}$$

$$c_0 = \frac{\alpha_c^2 (v_s - R_s i^{\text{ref}}_{Rq,\Gamma})\omega_s^2}{v_s}. \tag{6.45}$$

In Figure 6.3 the root loci of the fourth-order characteristic polynomial are shown. The figure shows how the poles move when the bandwidth of the current control loop, α_c, varies from 0.28 p.u. to 10 p.u. The reason that the bandwidth does not start at a lower value is that the active resistance, R_a, becomes negative for smaller bandwidths, and is therefore not applicable. In the figure, the induction machine is running as a generator at rated torque, synchronous speed, and is magnetized from the rotor circuit. This implies that $i^{\text{ref}}_{Rd,\Gamma}$ is set to 0.33 p.u., $i^{\text{ref}}_{Rq,\Gamma}$ is set to 0.78 p.u. and ω_r is set to 1 p.u. It

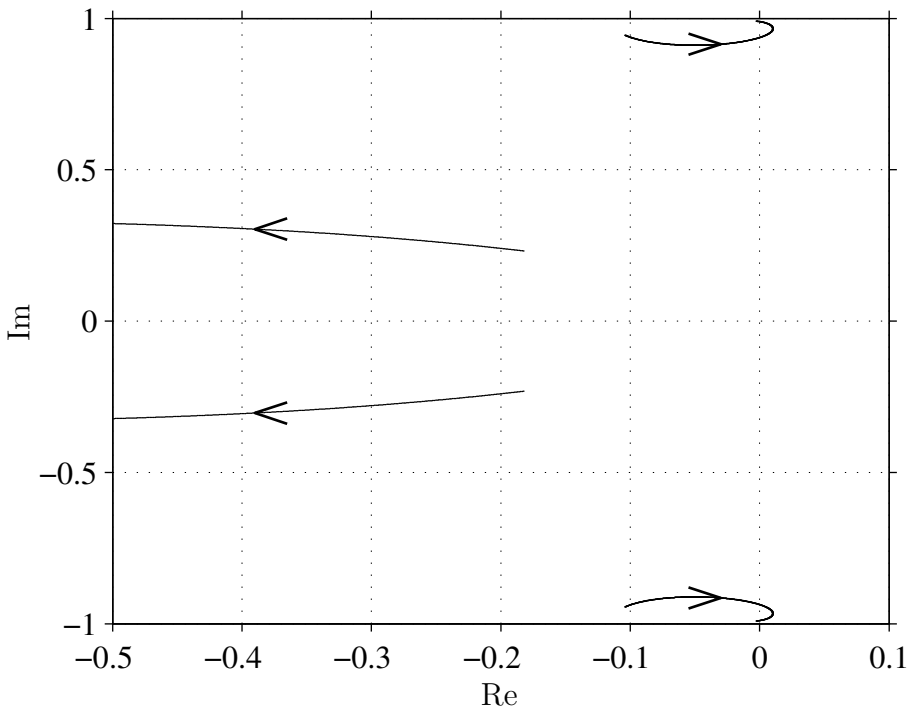

Figure 6.3: Root loci.

can be seen in the figure that the poorly damped poles move with increasing bandwidth of the current control loop from stable to unstable and back to be stable again. For the

case investigated in the figure, the system is unstable for bandwidths between 1 p.u. and 4.7 p.u.

Similar approach as in previous section with Routh's table produces very large expressions from which it is difficult to determine any constraints for stability. Therefore the approach with Routh's table is not carried out for this method.

This method actually might be unstable if the bandwidth of the current control loop is set to a high value. Therefore, one must very careful with the design and analysis of the system, if this method is to be chosen for controlling the rotor currents. The analysis of this system is rather difficult, since the system becomes quite complex.

"Active Resistance" and Feed-Forward of the Back EMF

The control law with feed-forward and active resistance can be expressed as

$$\mathbf{v}_{R,\Gamma} = k_p\mathbf{e} + k_i\mathbf{I} - (R_a - \mathrm{j}\hat{\omega}_2 L_{\sigma,\Gamma})\mathbf{i}_{R,\Gamma} + \mathbf{v}_s - (\frac{R_s}{L_{M,\Gamma}} + \mathrm{j}\omega_r)\psi_s. \tag{6.46}$$

and the dynamics are described by (6.28) to (6.31). Linearization of the system around its equilibrium point and after a first-order Taylor series expansion of the characteristic polynomial around $R_s = 0$, the following characteristic polynomial can be found:

$$(p+\alpha_c)^4\Big[p^2 + \frac{R_s}{L_{M,\Gamma}}\Big(2 - \frac{\omega_s L_{M,\Gamma} i^{\mathrm{ref}}_{Rd,\Gamma}}{v_s}\Big)p + \Big(1 - \frac{R_s i^{\mathrm{ref}}_{Rq,\Gamma}}{v_s}\Big)\omega_s^2\Big]. \tag{6.47}$$

The characteristic polynomial has four real roots located at $-\alpha_c$. The second-degree factor is identical to the characteristic polynomial in (5.59) where the current dynamics were neglected, i.e., assumed to be much faster than the flux dynamics. Therefore, when using feed-forward of the whole back emf and "active resistance" in the current control law, the same analysis as for the case with the assumption of fast current dynamics can be used.

6.1.5 Evaluation

In this section different current control laws will be compared:

I Current control with feed-forward of the back emf, without neglecting anything, as described in Section 6.1.1.

II Current control with active resistance to damp out the back emf, as described in Section 6.1.2.

III Current control with feed-forward of the back emf and active resistance, as described in Section 6.1.3.

In Figure 6.4 a Bode diagram, of the transfer function from $\mathbf{E}$ to $\mathbf{i}_{R,\Gamma}$, i.e., (6.24), for two different bandwidths of the current control loop, can be seen. The transfer functions are both without "active resistance" (I) and with "active resistance" (II and III).

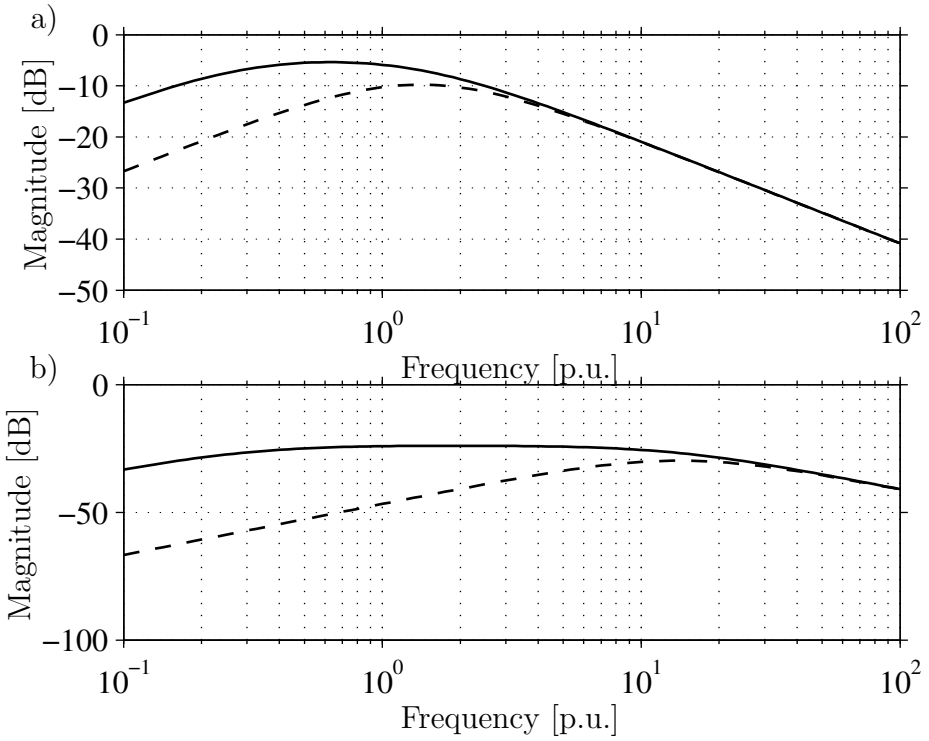

Figure 6.4: Bode diagram from $\mathbf{E}$ to $\mathbf{i}_{R,\Gamma}$. Without "active resistance" solid and with "active resistance" dashed. a) $\alpha_c = 1.4$ p.u. b) $\alpha_c = 14$ p.u.

It can be seen that when using "active resistance" that the damping of low-frequency disturbances has significantly improved. However, using the "active resistance" without feed-forward of the back emf (II) cannot be done without a careful analysis of the stability of the system, since as described in Section 6.1.4 the system might be unstable if the bandwidth of the current control loop is not set to a high value.

In Figure 6.5 simulations of current control using the above-mentioned Methods I to III are shown. In the simulations the reference values are initially set to zero; after 0.1 s $i^{\text{ref}}_{Rq,\Gamma}$ changes to 0.5 p.u., after 0.2 s $i^{\text{ref}}_{Rd,\Gamma}$ changes to -0.5 p.u. and, finally, after 0.3 s, $i^{\text{ref}}_{Rq,\Gamma}$ changes to -0.25 p.u. The bandwidth of the current control loop is set to 1.4 p.u., except Method III, where the bandwidth is set to 7 p.u., since as described in the previous section, the system tends to be unstable for medium bandwidths. The bandwidth 1.4 p.u. corresponds to a rise time (10%–90%) of 5 ms. It can be seen in the figure that oscillations caused from the flux have been damped out or been canceled by feed-forward compensation. In order to evaluate the performance of the current control laws experimentally, the doubly-fed induction machine has been exposed to current steps, see Figure 6.6. This has been done by letting $i^{\text{ref}}_{Rq,\Gamma}$ change from -0.25 p.u. to 0.25 p.u. when the rotor speed, ω_r, reaches 0.32 p.u. and vice versa when the rotor speed reaches 0.16 p.u. During the measurements the induction machine is magnetized entirely from the stator, i.e., $i^{\text{ref}}_{Rd,\Gamma} = 0$, and is operated under no-load conditions.

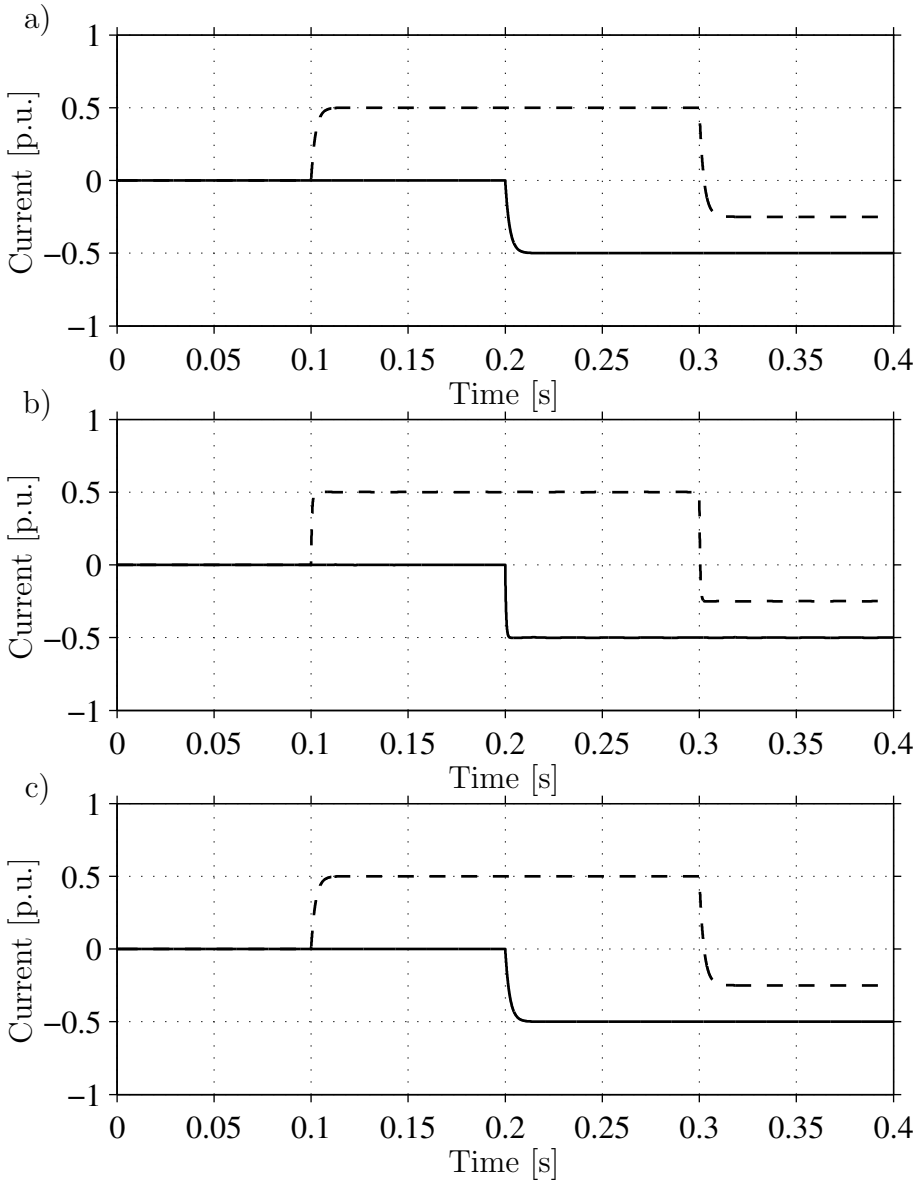

Figure 6.5: Simulation of rotor current control using feed-forward of the back emf. The rotor current's d component, $i_{Rd,\Gamma}$, is solid and the q component, $i_{Rq,\Gamma}$, is dashed. a) I (bandwidth 1.4 p.u.). b) II (bandwidth 7 p.u.). c) III (bandwidth 1.4 p.u.).

Further, the stator voltage of the doubly-fed induction machine was 230 V (the rated voltage of the machine is 380 V). Data have been sampled with 10 kHz and low-pass filtered with a cut-off frequency set to 5 kHz. In the measurements, the bandwidth of the current control was set to 1.4 p.u. During the experimental work it was found out that offsets in the stator voltage measurements caused a 100-Hz frequency component in the stator voltage. This 100-Hz frequency component influenced the performances of the current control Methods I and III, since the stator voltage is included in the control law. However, a notch filter was introduced to filter the stator voltage, and by this way the influence of the 100-Hz frequency component was limited. A scrutiny

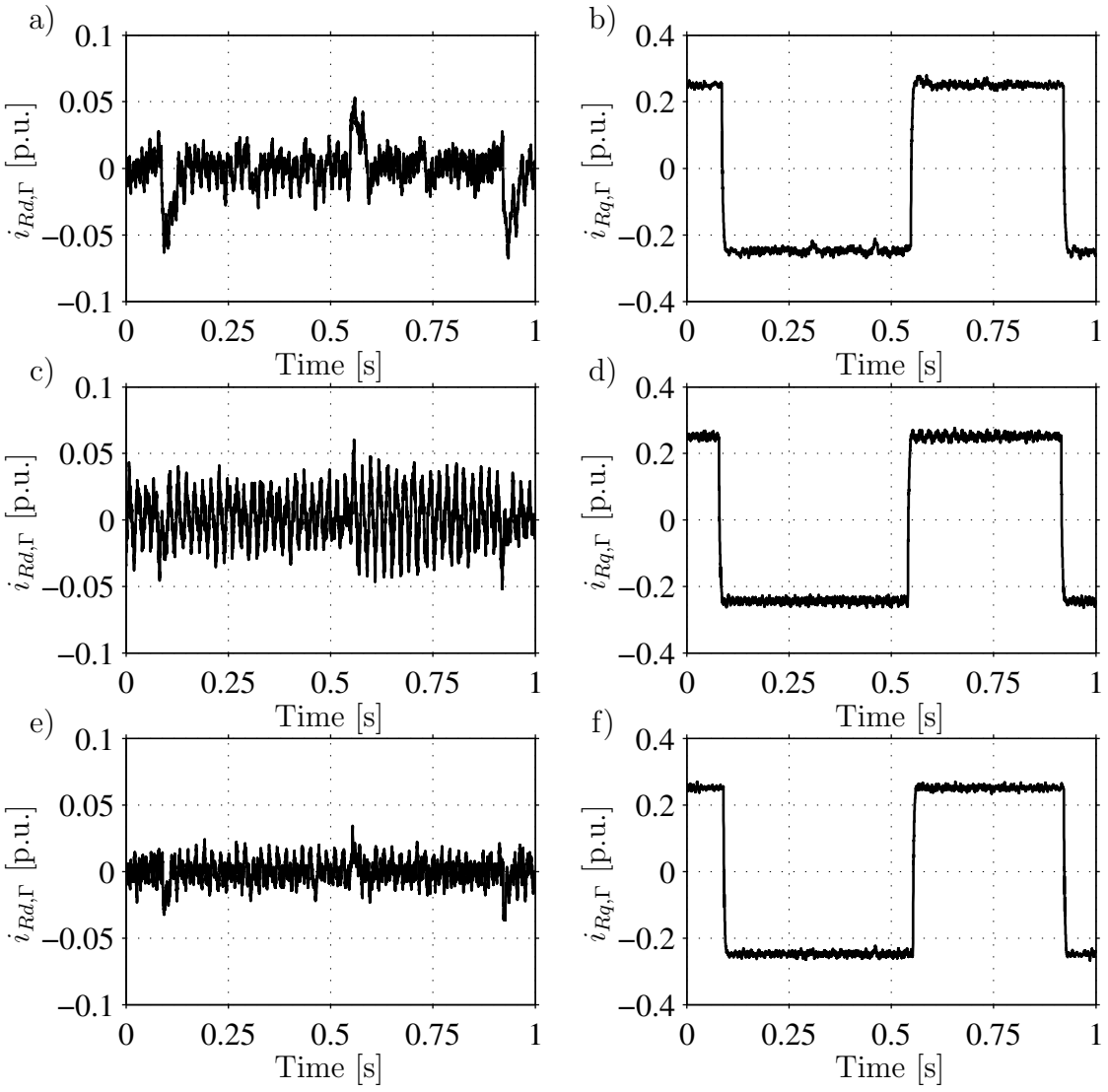

Figure 6.6: Measurement of the step response of the q component of the rotor current for the three current control methods. a) $i_{Rd,\Gamma}$ (I). b) $i_{Rq,\Gamma}$ (I). c) $i_{Rd,\Gamma}$ (II). d) $i_{Rq,\Gamma}$ (II). e) $i_{Rd,\Gamma}$ (III). f) $i_{Rq,\Gamma}$ (III).

investigation of Figure 6.6c) and d) reveal that Method II has a 50-Hz ripple. One reason for this is that using only "active resistance" to damp out the back emf, the system might be unstable as previously shown (note, that the operating condition in the measurements differs from plot in Figure 6.3). In Figure 6.6e) and f) it can be seen that the method with feed-forward of the back emf and with "active resistance" works well and the ripple in the d and q component is less than in the other investigated methods.

6.1.6 Conclusions and Discussion

The flux dynamics of the doubly-fed induction machine consists of two poorly damped poles which influence the current control loop, i.e., they will cause oscillations, close to the line frequency, in the flux and in the rotor currents. Current control Method I with feed-forward compensation of the whole back emf manages to suppress the oscillations in the d component of the rotor current. However, Method II which only uses "active resistance" to damp out disturbances acting on the rotor current might be unstable, even though the method manages to suppress low-frequency disturbances very well. For the current control Method III with feed-forward of the whole back emf and with the "active resistance," the stability analysis of the flux dynamics can be reduced to a system of the second order. This method manages to damp out both low-frequency disturbances in the d component rotor current and the oscillations caused by the flux dynamics better than the other methods in the comparison.

The dynamic performance of the doubly-fed induction machine, in comparison to singly-fed induction machine, is less good since, as mention before, it consists of two poorly damped poles which becomes unstable for a certain value of the d component of the rotor current.

6.2 Damping of Flux Oscillations

In Section 5.3.2, a short presentation of different methods of damping the flux oscillations was given. In this thesis, the flux oscillations will be damped out by feedback of the derivative of the flux. The reason that this method is chosen is that this method has low cost (i.e., no extra hardware), is easy to implement, and can damp the flux oscillations well. Due to the fact that the method with an extra inverter connected to the star-point of the stator winding has to handle the stator current, implying an increase of the losses, and the increased cost for an extra inverter this method, is not considered in this thesis since some of the benefits and reasons for the doubly-fed induction generator, e.g., smaller (cheaper) inverter and lower losses, vanishes.

The q component of the rotor current will be used for controlling the torque or the speed, but the d component of the current can be used to damp the oscillations and improve the stability. If we add a component $\Delta i^{\text{ref}}_{Rd,\Gamma}$ to the d component of the rotor current reference, which we control as

$$\Delta i^{\text{ref}}_{Rd,\Gamma} = -\frac{p}{p+\alpha_f}\frac{\alpha_d}{R_s}\psi_s \tag{6.48}$$

then we have introduced a flux differentiation compensation term, that will improve the damping of the system. In the above equation, a low-pass filter has been added since a pure differentiation is not implementable. Under the assumption that the current dynamics are set much faster than the flux dynamics and α_f is small, the characteristic polynomial in (5.59) can be rewritten as

$$p^2 + \Big[\alpha_d + \frac{R_s}{L_{M,\Gamma}}\Big(2 - \frac{\omega_s L_{M,\Gamma} i^{\text{ref}}_{Rd,\Gamma}}{v_s}\Big)\Big]p + \Big(1 - \frac{R_s i^{\text{ref}}_{Rq,\Gamma}}{v_s} + \alpha_d R_s \frac{v_s - i_{Rd0,\Gamma} L_{M,\Gamma}\omega_s}{v_s L_{M,\Gamma}\omega_s^2}\Big)\omega_s^2. \tag{6.49}$$

With the inclusion of a flux damping, the constraint on the d component becomes

$$i_{Rd0,\Gamma} < \Big(2 + \alpha_d \frac{L_{M,\Gamma}}{R_s}\Big)\frac{v_s}{\omega_s L_{M,\Gamma}} \tag{6.50}$$

in order to guarantee stability. Comparing to (5.60), it is seen that the constraint on the d component rotor current has increased $(2 + \alpha_d L_{M,\Gamma}/R_s)/2$ times.

6.2.1 Parameter Selection

As can be seen in (6.48) the flux damping uses two parameters, α_d and α_f, that have to be determined. Obviously, the cut-off frequency of the low-pass filter, α_f, must be set lower than the oscillating frequency in order to be able to damp the oscillation at all. The damping term, α_d, must be chosen smaller than the bandwidth of the current control loop, α_c, so that the flux damper becomes slower than the current dynamics. Of course, if a flux estimation is used to determine the flux, the bandwidth of the damper, α_d, must be smaller than the bandwidth of the flux estimation.

6.2.2 Evaluation

Figure 6.7 shows a simulation of a vector-controlled doubly-fed induction machine, according to (6.18), with and without flux damping. The reference value $i^{\text{ref}}_{Rd0,\Gamma}$ is initially zero and is at 0.5 s changed to -0.5 p.u. The reference value of $i^{\text{ref}}_{Rd,\Gamma}$ is initially zero and is at 0.25 s it is changed to 0.5 p.u., and at 0.75 s to -0.25 p.u. The

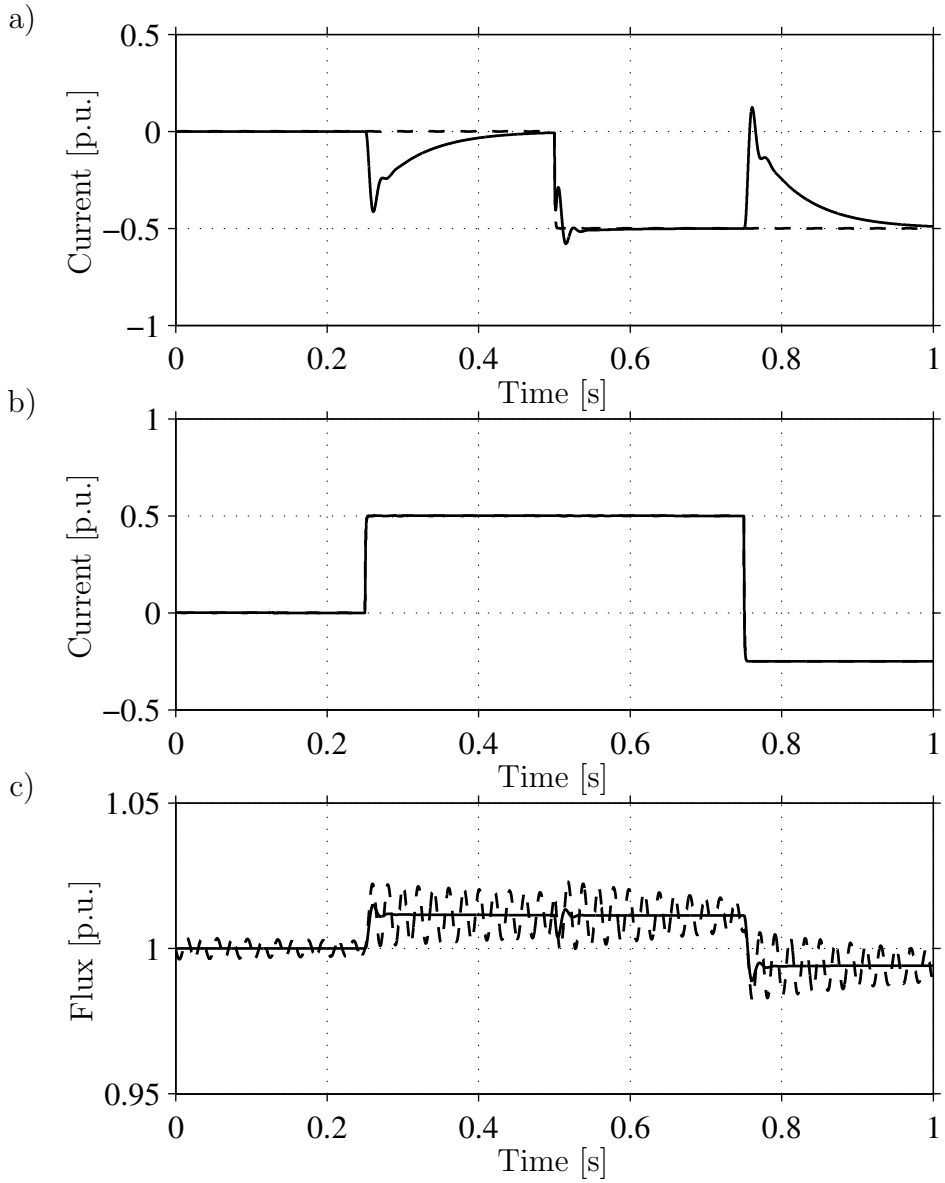

Figure 6.7: Simulation of current control with (solid) and without (dashed) damping of the flux oscillations. a) $i_{Rd,\Gamma}$. b) $i_{Rq,\Gamma}$. c) ψ_s.

bandwidth of the system, α_c, is set to 4.7 p.u., while α_d is set to 0.7 p.u., and α_f is set to 0.05 p.u. In the simulation it is assumed that the flux can be determined from measurements of the stator and the rotor currents. It can be seen in the figure that the oscillations in the flux has been damped out with the flux damper. Since it is difficult to see the effect of the flux damper in a measured time series, due to noise, a frequency

spectra of the flux magnitude has been plotted instead in Figure 6.8. In the figure the current control method with feed-forward of the back emf and with active resistance has been used, with and without flux damping. The frequency spectra is based on a 6 s long measurement. The doubly-fed induction machine is operated as described in Section 6.1.5. The bandwidth of the current control loop, α_c, was set to 2.3 p.u., the damping term, α_d, was set to 0.7 p.u. and, the cut-off frequency term, α_f, was set to 0.05 p.u. It can be seen in the figure that the 50-Hz component has been to a large

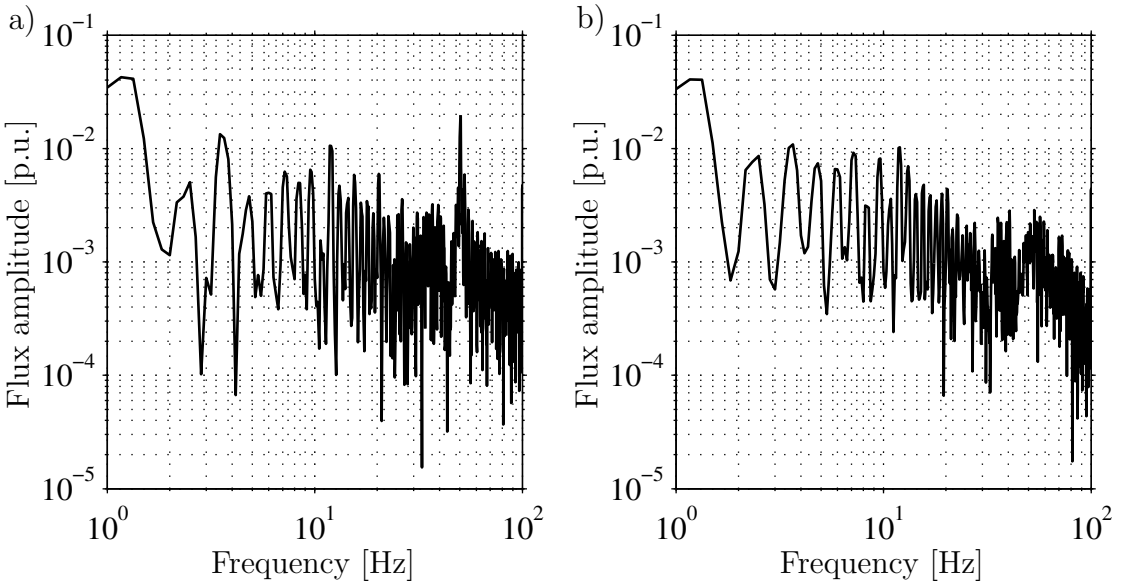

Figure 6.8: Frequency spectra of the flux (data from measurements). a) Without flux damping. b) With flux damping.

extent damped out, i.e., a factor of ten, by the flux damper.

6.3 Stator Current Control with Feed-Forward of the Back EMF and "Active Resistance"

One possibility, as mentioned before, is to control the stator currents instead of the rotor currents. In this section a stator current control law with feed-forward of the back emf and "active resistance" will be derived. The stator current will be controlled with stator flux orientation. The inverse-Γ representation of the induction machine will be used. Eliminating the rotor currents and the rotor flux from (5.23) and (5.24) yields

$$\mathbf{v}_s = R_s\mathbf{i}_s + \frac{\mathrm{d}\boldsymbol{\Psi}_s}{\mathrm{d}t} + \mathrm{j}\,\omega_1\boldsymbol{\Psi}_s \tag{6.51}$$

$$L_\sigma\frac{\mathrm{d}\mathbf{i}_s}{\mathrm{d}t} = -\mathbf{v}_R - \Big(R_s + R_R\frac{L_\sigma + L_M}{L_M} + \mathrm{j}\,\omega_2 L_\sigma\Big)\mathbf{i}_s + \Big(\frac{R_R}{L_M} - \mathrm{j}\,\omega_r\Big)\boldsymbol{\Psi}_s + \mathbf{v}_s. \tag{6.52}$$

Since we are free to chose the rotor voltage, we can chose it as

$$\mathbf{v}_R = \mathbf{v}'_R + (R_a - \mathrm{j}\omega_2 L_\sigma)\mathbf{i}_s + \Big(\frac{R_R}{L_M} - \mathrm{j}\omega_r\Big)\mathbf{\Psi}_s + \mathbf{v}_s \tag{6.53}$$

in order to feed-forward the back emf and include the "active resistance," R_a. Now it is possible to write the current dynamics (6.52) as

$$L_\sigma \frac{\mathrm{d}\mathbf{i}_s}{\mathrm{d}t} = -\mathbf{v}'_R - \Big(R_s + R_R\frac{L_\sigma + L_M}{L_M} + R_a\Big)\mathbf{i}_s. \tag{6.54}$$

The transfer function, $G'(p)$, from $\mathbf{v}_R$ to $\mathbf{i}_s$ becomes

$$G'(p) = \frac{-1}{pL_\sigma + R_s + R_R\frac{L_\sigma + L_M}{L_M} + R_a}. \tag{6.55}$$

Using IMC, the proportional and integral gains of a PI-controller can be found as

$$k_p = -\alpha_c L_\sigma \qquad k_i = -\alpha_c\Big(R_s + R_R\frac{L_\sigma + L_M}{L_M} + R_a\Big). \tag{6.56}$$

If the "active resistance" is set to

$$R_a = \alpha_c L_\sigma - R_s - R_R\frac{L_\sigma + L_M}{L_M} \tag{6.57}$$

a disturbance will be damped out with the same bandwidth as the current control loop. Compare to Section 6.1.2.

6.3.1 Stability Analysis

The current dynamics are assumed to be much faster than the flux dynamics. From (6.51) we can get the flux dynamics divided into real and imaginary parts and taking into account field orientation, as

$$\frac{\mathrm{d}\psi_s}{\mathrm{d}t} = -v_s\sin(\theta_s - \theta_1) - R_s i_{sd} \tag{6.58}$$

$$\frac{\mathrm{d}\theta_1}{\mathrm{d}t} = \omega_1 = \frac{v_s\cos(\theta_s - \theta_1) - R_s i_{sq}}{\psi_s} \tag{6.59}$$

where the stator voltage can be found from (6.11). Making the variable substitution $\Delta\theta = \theta_s - \theta_1$ yields

$$\frac{\mathrm{d}\psi_s}{\mathrm{d}t} = -v_s\sin(\Delta\theta) - R_s i_{sd} \tag{6.60}$$

$$\frac{\mathrm{d}\Delta\theta}{\mathrm{d}t} = \omega_s - \frac{v_s\cos(\Delta\theta) - R_s i_{sq}}{\psi_s} \tag{6.61}$$

where ω_s is the frequency of the grid voltage. As for the stability analysis in Section 5.3.2, the system has two equilibrium points (neglecting the periodic solutions of

the trigonometric functions) where one of the solutions is unfeasible since it corresponds to negative flux. The interesting equilibrium point becomes

$$\psi_{s0} = \frac{\sqrt{1 - \frac{R_s^2 i_{sd}^2}{v_s^2}} v_s - R_s i_{sq}}{\omega_s} \approx \frac{v_s - R_s i_{sq}}{\omega_s} \tag{6.62}$$

$$\Delta\theta_0 = -\cos^{-1}\left(\sqrt{1 - \frac{R_s^2 i_{sd}^2}{v_s^2}}\right) \approx -\frac{R_s}{v_s} i_{sd}. \tag{6.63}$$

The characteristic polynomial of the system around the equilibrium point yields

$$p^2 + \frac{R_s i_{sd} \omega_s}{\sqrt{1 - \frac{R_s^2 i_{sd}^2}{v_s^2}} v_s - R_s i_{sq}} p + \frac{\sqrt{1 - \frac{R_s^2 i_{sd}^2}{v_s^2}} v_s \omega_s^2}{\sqrt{1 - \frac{R_s^2 i_{sd}^2}{v_s^2}} v_s - R_s i_{sq}}. \tag{6.64}$$

A first-order Taylor series expansion, around $R_s = 0$, of the characteristic polynomial above yields

$$p^2 + \frac{R_s i_{sd} \omega_s}{v_s} p + \frac{(v_s + R_s i_{sq})\omega_s^2}{v_s}. \tag{6.65}$$

In the above characteristic polynomial it can be seen that i_{sd} must be greater than zero to maintain stability. Further, the q component of the rotor current must be

$$i_{sq} > -\frac{v_s}{R_s}. \tag{6.66}$$

However, this constraint will hardly make any difference on the stability, since the stator voltage is 1 p.u. and the stator resistance is at least less than 0.1 p.u. (according to Table 4.1). This means that $i_{sq} > -10$ p.u., which is ten times the rated current.

One possibility would also to apply flux damping in a way similar to what has been done in the previous section, i.e., letting

$$\Delta i_{sd}^{\text{ref}} = \frac{p}{p + \alpha_f} \frac{\alpha_d}{R_s} \psi_s. \tag{6.67}$$

Then, the characteristic polynomial in (6.65) becomes

$$p^2 + \left(\alpha_d + \frac{R_s i_{sd} \omega_s}{v_s}\right) p + \frac{(v_s + R_s i_{sq})\omega_s^2 + \alpha_d R_s i_{sd} \omega_s}{v_s}. \tag{6.68}$$

if the "low-pass" constant α_f is small.

If the characteristic polynomial, in (6.49), for the rotor current control with flux damping, as described in Section 6.2, is rewritten as

$$p^2 + \left[\alpha_d + \frac{R_s}{L_{M,\Gamma}}\left(1 + \frac{\omega_s L_{M,\Gamma} i_{sd}}{v_s}\right)\right] p + \left(1 + \frac{R_s i_{sq}}{v_s} + \frac{\alpha_d R_s i_{sd}}{v_s \omega_s}\right)\omega_s^2 \tag{6.69}$$

where the rotor currents has been exchanged to the stator currents, i.e., $i_{Rd,\Gamma} = \psi_s/L_{M,\Gamma} - i_{sd}$ and $i_{Rq,\Gamma} = -i_{sq}$. If $\alpha_d \gg R_s/L_{M,\Gamma}$ then the characteristic polynomial above can be approximated as

$$p^2 + \Big(\alpha_d + \frac{\omega_s R_s i_{sd}}{v_s}\Big)p + \Big(1 + \frac{R_s i_{sq}}{v_s} + \frac{\alpha_d R_s i_{sd}}{v_s \omega_s}\Big)\omega_s^2 \tag{6.70}$$

which is identical to the characteristic polynomial in (6.68), i.e., the dynamics are the same whether the rotor or stator currents are controlled when damping of the flux is used. Since the dynamics of stator current control and rotor current control are the same when using flux damping, only rotor current control will be treated further.

6.4 Investigation of Grid Disturbances

In this section the response of the doubly-fed induction machine due to grid disturbances will be studied. As shown in Section 5.3.2 and in Section 6.1.4, the doubly-fed induction machines consists of two poorly damped poles, with the oscillation frequency near the line frequency. These poorly damped poles will cause oscillations in the flux if the doubly-fed induction machine is exposed to a grid disturbance. Figure 6.9 shows a circuit of the doubly-fed induction generator system with a back-to-back inverter. Since the stator-to-rotor turns ratio, of the doubly-fed induction generator, is designed

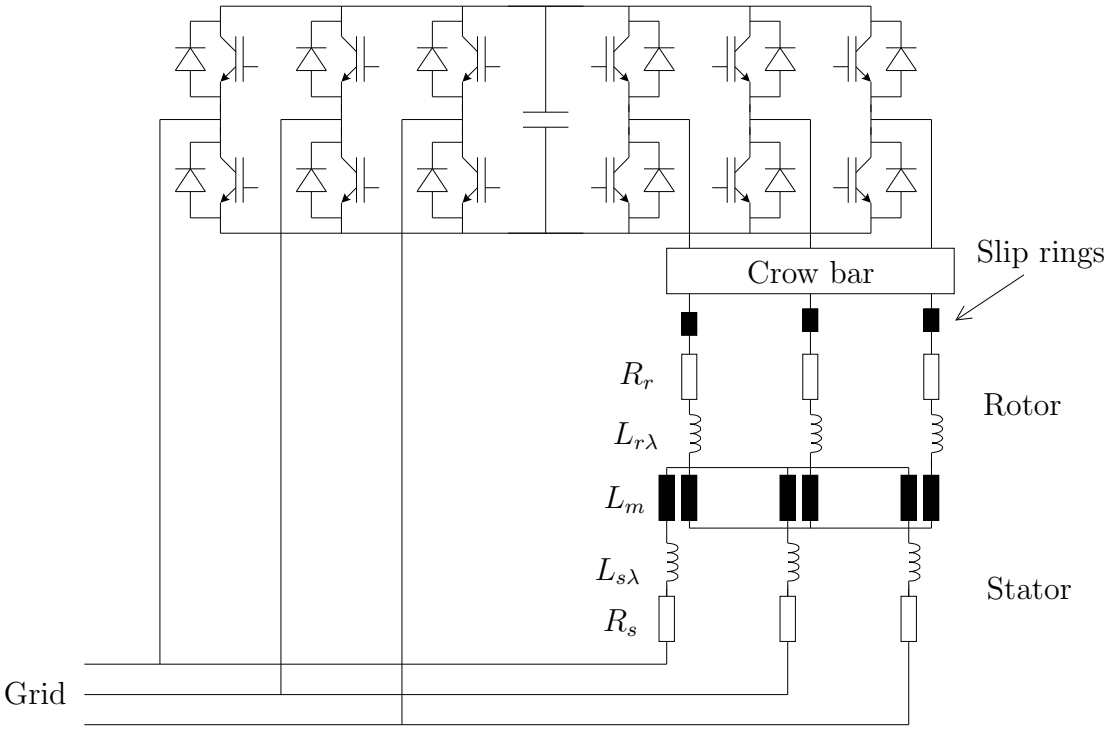

Figure 6.9: Doubly-fed induction generator circuit.

according to the desired variable-speed range it might not be possible to achieve the desired rotor voltage in order to control the rotor currents. This means that when the rotor voltage becomes limited it is not possible to control the current as desired. This implies that a voltage dip can cause high induced voltages or currents in the rotor circuit. If the rotor current or the internal rotor voltage becomes too high due to a line fault, e.g. a voltage dip, it is necessary to have a protection device that short circuit the rotor circuit, i.e., a crow bar, and thereby protect the inverter from over currents and the rotor of the generator to over-voltages. In this section an investigation of how the rotor current is influenced by a voltage dip is performed. Throughout this section a voltage dip will be referred to how much the voltage drops. For example, a voltage dip of 25 %, on a 400 V grid, implies that the remaining voltage in the grid is 75 %, i.e., 300 V. The grid disturbances, in this section, will be limited to symmetrical voltage dips only.

In order to show typical responses to voltage dips of wind turbines, equipped with doubly-fed induction generator, some measurements will be presented. Figure 6.10 shows a measurements of the response of a Vestas V52-850 kW wind turbine to a voltage dip. The voltage drops approximately 5 % after 0.1 s. The measured data was sampled with 2048 Hz and automatically low-pass filtered with the cut-off frequency set to 1000 Hz. The Vestas V52-850 kW wind turbine has a doubly-fed induction generator where the speed can vary with up to 60 % [70]. Before the voltage dip occurs the wind

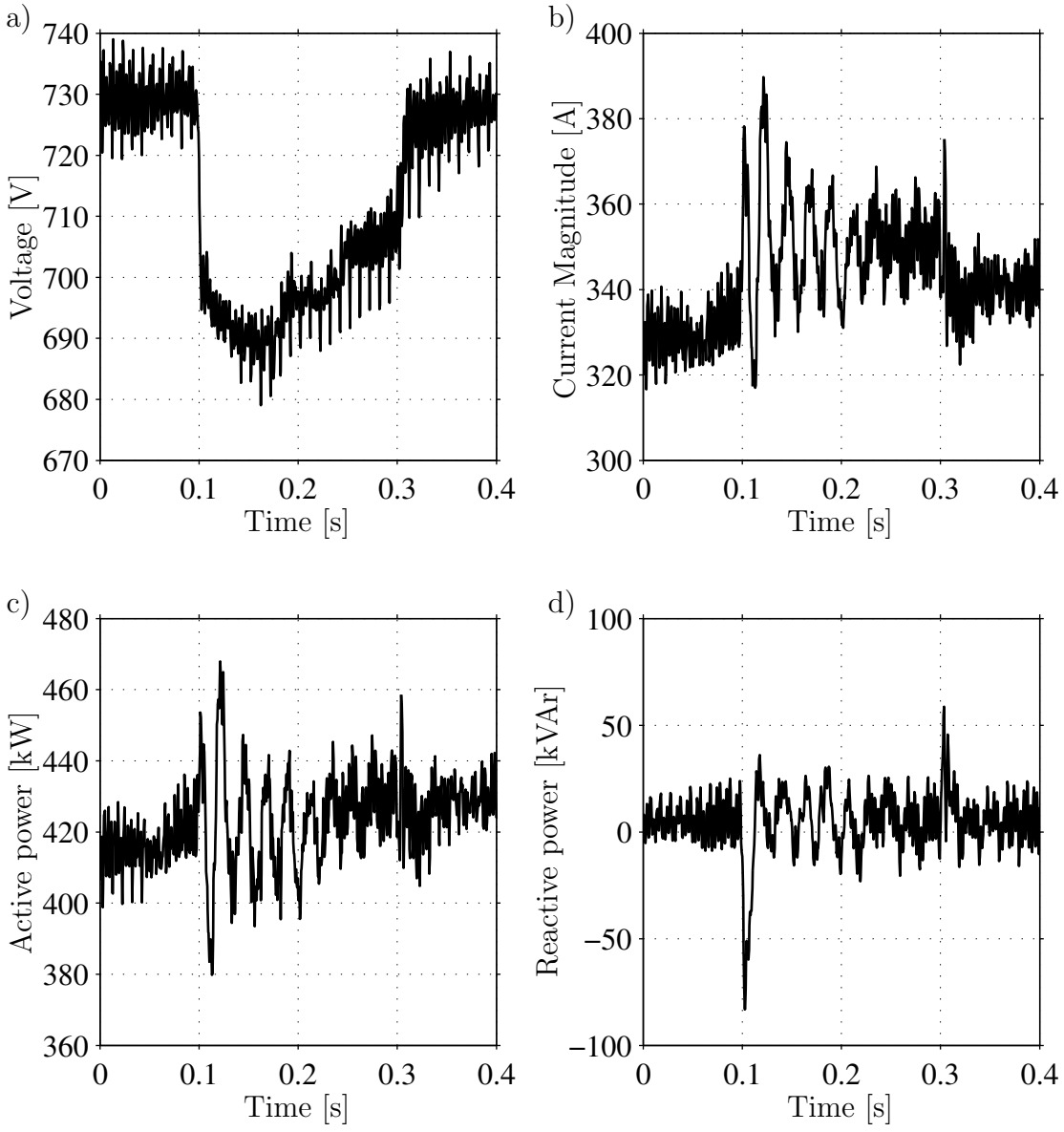

Figure 6.10: Measurement of the response of a Vestas V52-850 kW wind turbine to a voltage dip. a) Voltage. b) Current magnitude. c) Active power. d) Reactive power.

turbine is producing about 420 kW, which corresponds to approximately 50 % of the nominal power of the turbine. It can be seen in the figure that oscillations occur in the grid current, the active and the reactive power delivered to the grid. These oscillations

are caused by the poorly damped poles. The response to a larger voltage dip can be seen in Figure 6.11. The voltage drops down approximately 25 % to 550 V at t=0.1 s and after 0.1 s the fault, causing the voltage dip on the grid, is cleared, and the voltage starts to recover. Before the voltage dip the wind turbine is producing about 150 kW, which corresponds to approximately 18 % of the nominal power of the turbine. As for

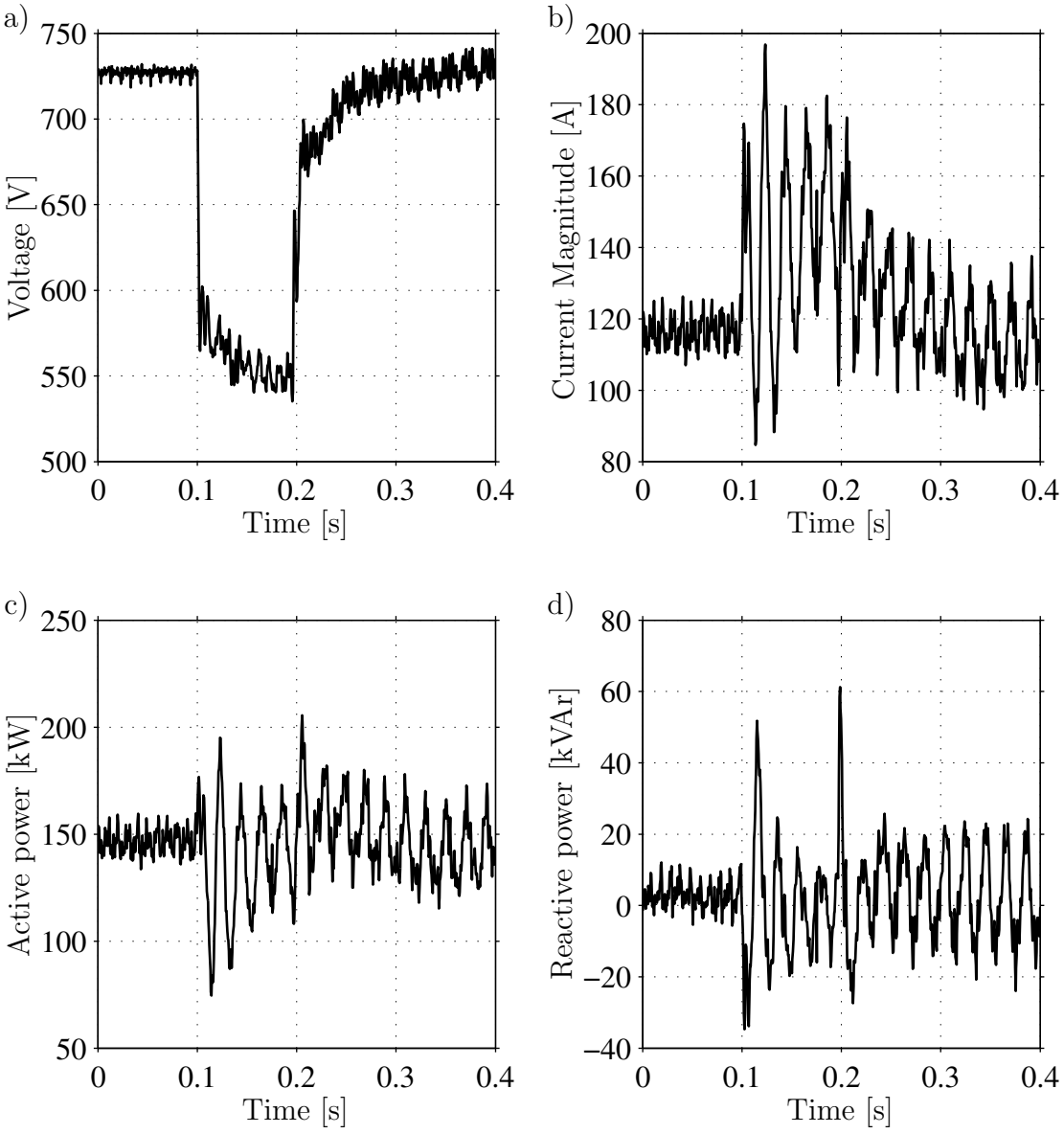

Figure 6.11: Measurement of the response of a Vestas V52-850 kW wind turbine to a voltage dip. a) Voltage. b) Current magnitude. c) Active power. d) Reactive power.

the case with a 5 % voltage dip, oscillations, close to the line frequency, occurs in the grid current, the active and the reactive power delivered to the grid.

As mentioned before the magnitude of the grid current is shown in Figure 6.10 and Figure 6.11 and not the stator current. The grid current consists of the stator current and the current from the inverter. However, the figures still show the typical response,

with oscillations close to line frequency, of doubly-fed induction machines due to a voltage dip.

6.4.1 Assumptions

In simulations that will be presented later on, the rotor current reference values have been set, unless otherwise stated, to

$$i_{Rd,\Gamma}^{\text{ref}} = \frac{\psi}{L_{M,\Gamma}} \tag{6.71}$$

$$i_{Rq,\Gamma}^{\text{ref}} = -\frac{T^{\text{ref}}}{3n_p\psi} \tag{6.72}$$

where the flux is approximated as $\psi \approx V_{\text{base}}/\omega_{\text{base}}$. This choice of the d component of the rotor current reference implies that the doubly-fed induction machine is magnetized from the rotor circuit.

The doubly-fed induction machine will operate under the following conditions before the grid disturbances

Case I 10 % of rated torque and at a rotor speed of 0.7 p.u.

Case II 50 % of rated torque and at synchronous rotor speed.

Case III 100 % of rated torque and at a rotor speed of 1.3 p.u.

Case IV 115 % of rated torque and at a rotor speed of 1.3 p.u.

The reason for choosing these four cases is the fact that these operating conditions reflect four normal operating-points of a variable-speed wind turbine. During the simulations in this section, the rotor speed, during the disturbance, is assumed to be constant.

Note, that throughout this section the rotor currents and voltages are referred to the stator circuit. For example, if the stator-to-rotor turns ratio equals 1:3 then the rotor voltage, referred to the stator circuit, is one third of the actual and the rotor current, referred to the stator circuit, is three times the actual. Other data and parameters of the doubly-fed induction machine, used in the simulations, can be found in Appendix C.2.

6.4.2 Without Flux Damping

When investigating how the maximum rotor current is influenced by a voltage dip, the following control-law methods will be used:

Method A The current control law given by (5.46).

Method B The current control law with feed-forward of the back emf. In the feed-forward back emf term the derivative of the flux is neglected. The current control law is given by (5.49).

Method C The current control law with feed-forward of the whole back emf as described by (6.18)

It can be noted that in neither of the control laws, flux damping has been performed, as described in Section 6.2. In order to verify the model of the doubly-fed induction machine comparisons of simulated and laboratory results, for a voltage dip, will be presented. Figure 6.12 shows the response of the laboratory doubly-fed induction machine due to a voltage dip. The voltage drops approximately 4.5 %. The induction machine is controlled using Method A and the bandwidth of the current control loop was set to 0.35 p.u., corresponding to a rise time of 20 ms. During the measurements, the stator is connected in series with resistances of approximately 0.85 Ω, which are short-circuited to accomplish a voltage dip. The induction machine is accordingly operated as a generator. The measured data were sampled with 10 kHz and low-pass filtered with a cut-off frequency set to 500 Hz. It can be seen in the figure that almost the same response could be accomplished using simulations as the measured ones.

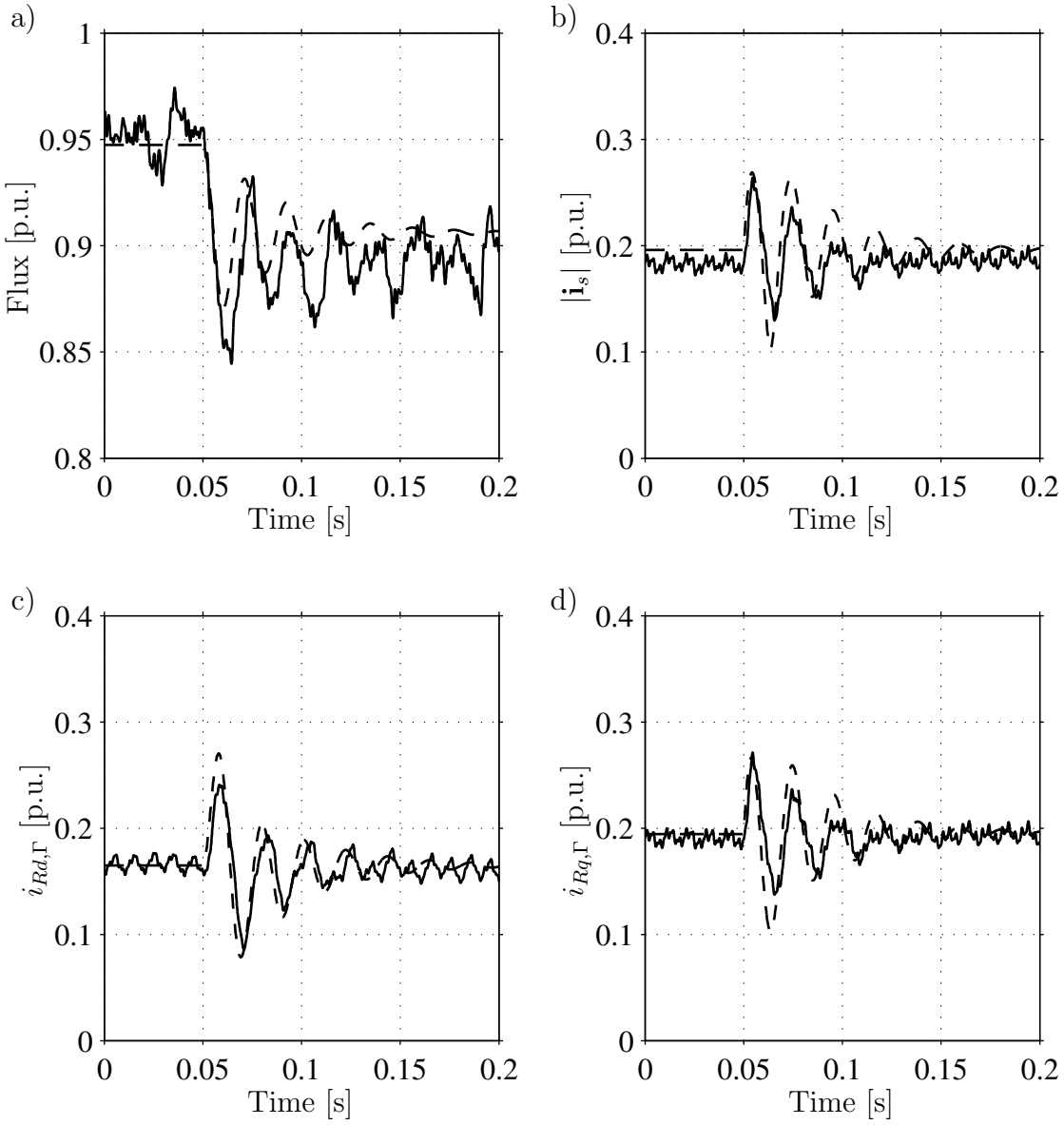

Figure 6.12: The response for method A due to a voltage dip. Solid line is measurements and dashed lines are simulation. a) ψ_s. b) $\mathbf{i}_s$. c) $i_{Rd,\Gamma}$. d) $i_{Rq,\Gamma}$.

Figure 6.13 shows a simulation of the responses, for current control Methods A to C, for a voltage dip of 25 %. In the simulation, the doubly-fed induction machine is magnetized from the rotor circuit, i.e., $i^{\text{ref}}_{Rd,\Gamma}$ is set according to (6.71), and is running at a rotor speed of 0.8 p.u. and at 17 % of rated torque. The bandwidth of the current control loop in the simulation was set to 0.7 p.u. It can be seen in the figure that

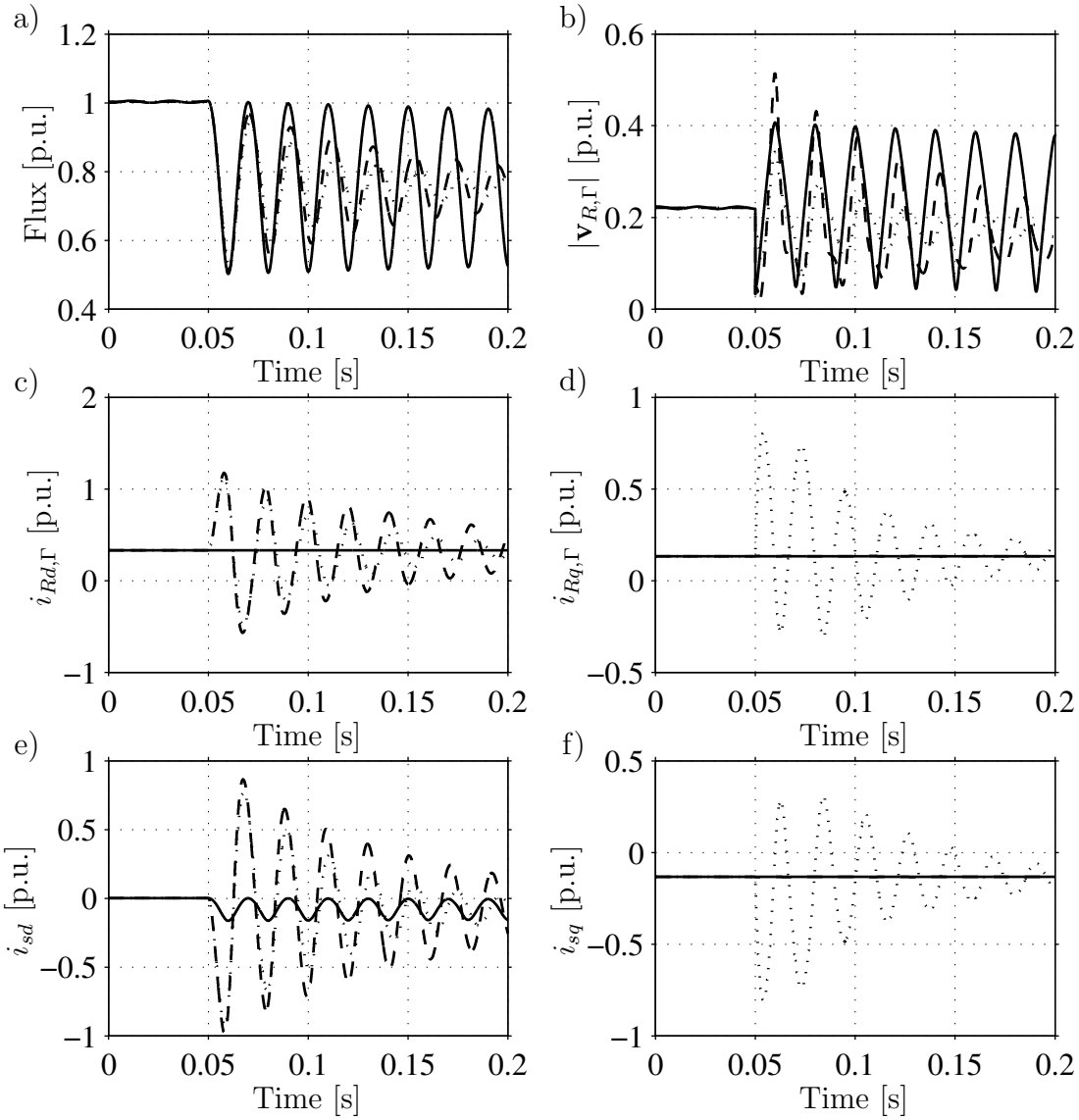

Figure 6.13: Responses due to a voltage dip, of 25 %, for current control Method A (dotted), Method B (dashed), and Method C (solid). a) Flux, ψ_s. b) Rotor voltage, $|\mathbf{v}_{R,\Gamma}|$. c) d component rotor current, $i_{Rd,\Gamma}$. d) q component rotor current, $i_{Rq,\Gamma}$. e) d component stator current, i_{sd}. f) q component stator current, i_{sq}.

Method A gives oscillations in both the d and the q component of the rotor current. The reason for this is that the "whole" back emf, i.e.,

$$\mathbf{E} = \frac{\mathrm{d}\psi_s}{\mathrm{d}t} + \mathrm{j}\,\omega_2\psi_s = \mathrm{j}\,v_s \mathrm{e}^{\mathrm{j}\,(\theta_s - \theta_1)} - \Big(\frac{R_s}{L_{M,\Gamma}} + \mathrm{j}\,\omega_r\Big)\psi_s \tag{6.73}$$

is treated as a disturbance to the current controller. In (6.73) it can be seen that the derivative of the flux will influence the d component of the rotor current while the term $\mathrm{j}\omega_2\psi_s$ will influence the q component of the rotor current. For Method B, the term $\mathrm{j}\omega_2\psi_s$, in the back emf is compensated for in a feed-forward manner. Therefore, the oscillations in the q component has vanished. In Method C, where the flux derivative in the back emf is not neglected in the feed-forward compensation term, the oscillations in the flux will not influence the rotor current, but then the oscillations is "pushed over" to the d component of the stator current. On the other hand, for Method C the flux oscillation, are worse damped than for Methods A and B. In the simulations the rotor voltage has not been limited, i.e., the current controller puts out the desired voltage. However, in a real system, the rotor voltage must be limited when it reaches the maximum value that the inverter can deliver. If the rotor voltage becomes limited the current controller loses control of the rotor current, which then might reach the rated current of the inverter. Then, the "crow bar" must short circuit the rotor circuit in order to protect the inverter.

In order to investigate the response to different magnitudes of the voltage dips and for different bandwidths of the current control loop, several simulations have been carried out. For Metod B the maximum current due to a voltage dip, can be seen in Figure 6.14, for different bandwidths of the current control loop, α_c. In the figure, the doubly-fed induction machine is operated under the four different conditions, Case I–Case IV. The different operating conditions are given in Section 6.4.1. It can be seen in the figure that the maximum rotor current increases with the size of the voltage dip, especially for low bandwidths of the current control loop. For higher bandwidths of the current control loop it can be seen that the rotor current is practically constant. The reason for this is that when the bandwidth is increased the "need" for compensating the back emf vanish, cf. the Bode plot in Figure 5.10. However, for large voltage dips and low bandwidths the results are independent of the operating point. The corresponding maximum rotor voltages, for Method B, are presented in Figure 6.15. In the figure it can be seen that the maximum rotor voltage increases with the size of the voltage dip. Further, the maximum rotor voltage, for large voltage dips, is relatively similar between the different operating points investigated. It can also be noted that the maximum rotor voltage, due to a voltage dip, is quit independent of the bandwidth of the current control loop, α_c.

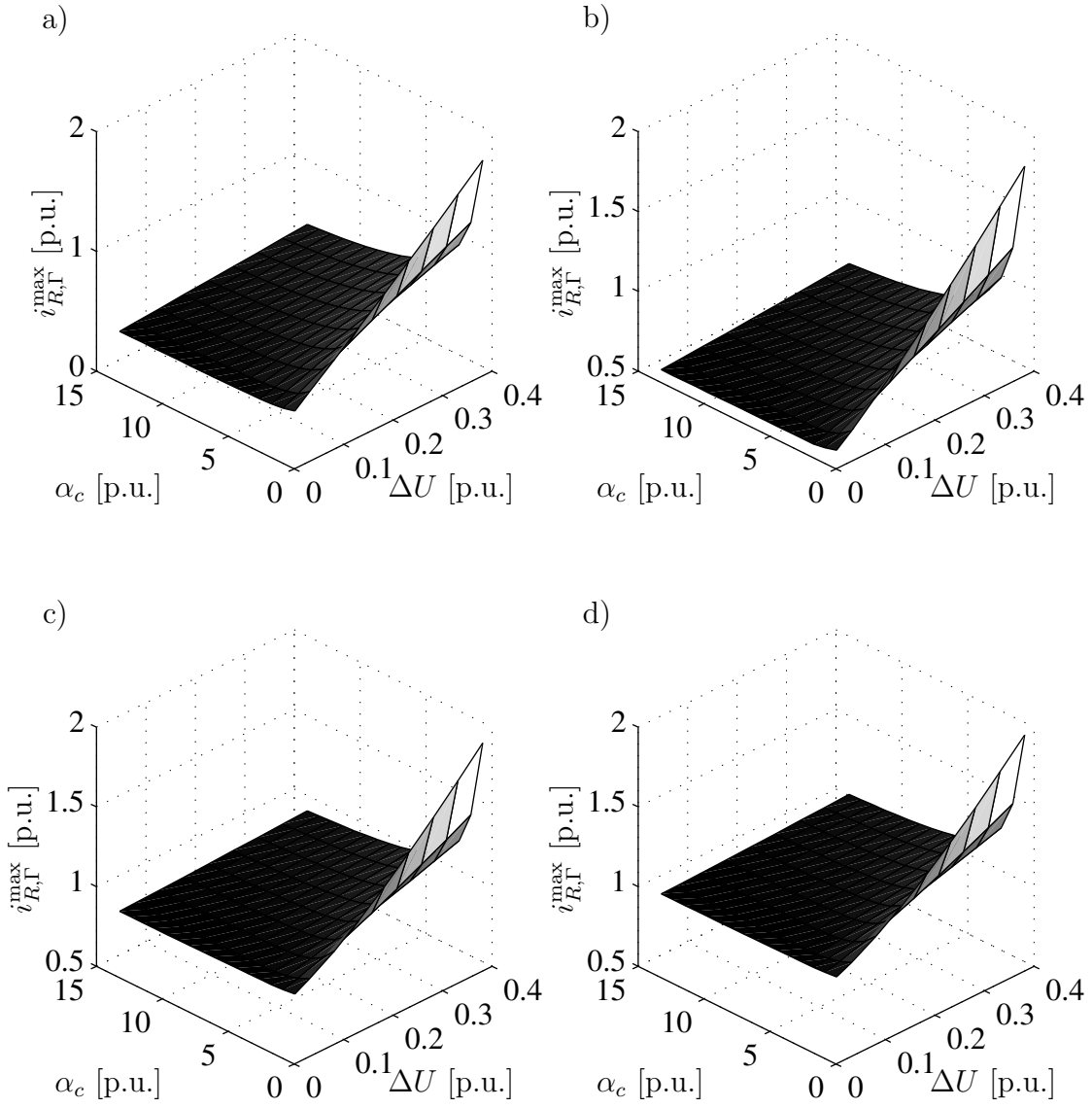

Figure 6.14: Maximum value of the rotor current, for current control Method B, after a voltage dip, and for different bandwidths of the current control loop, α_c. a) Case I. b) Case II. c) Case III. d) Case IV.

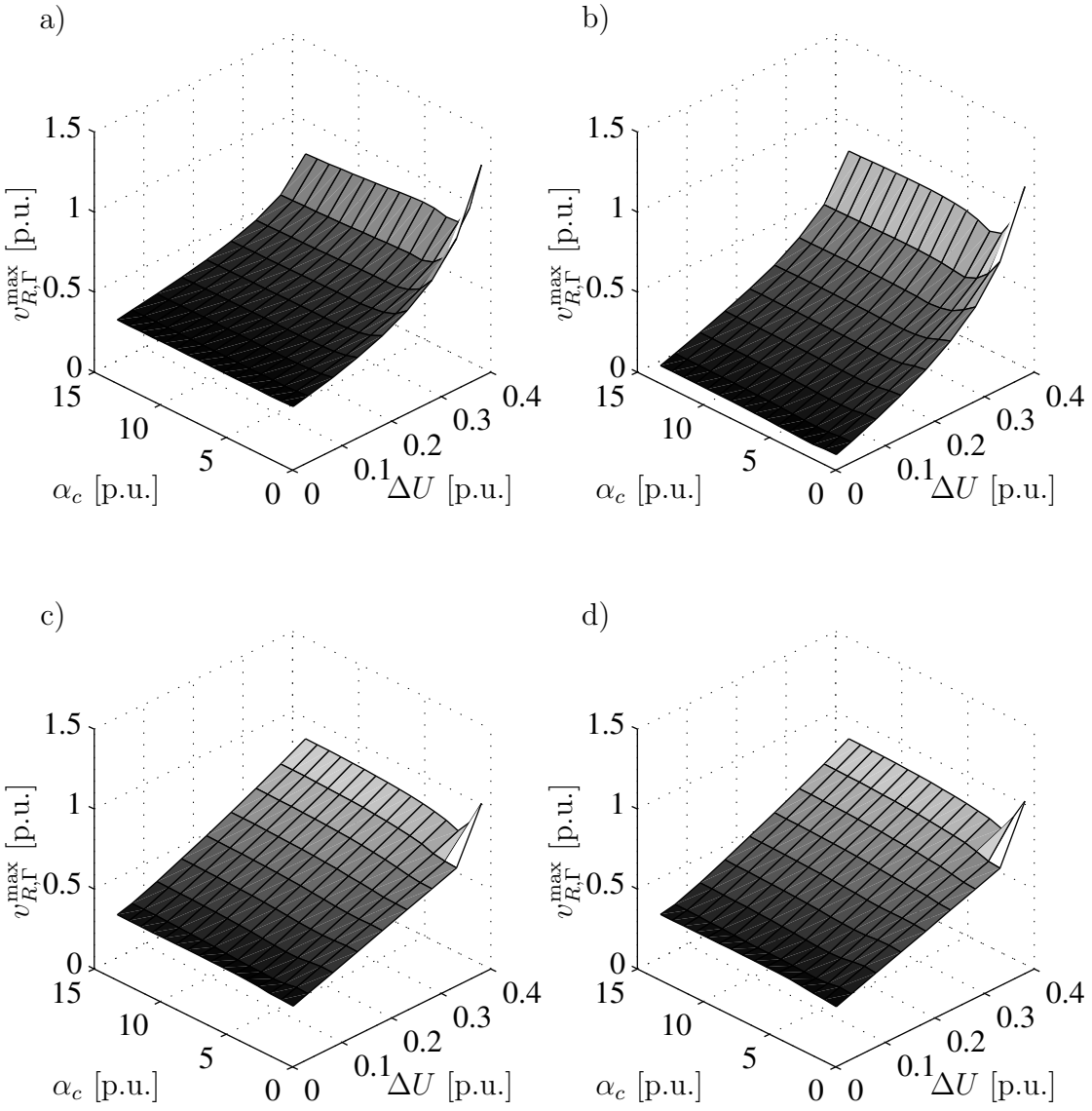

Figure 6.15: Maximum value of the rotor voltage, for current control Method B, after a voltage dip, and for different bandwidths of the current control loop, α_c. a) Case I. b) Case II. c) Case III. d) Case IV.

Figure 6.16 shows the corresponding maximum rotor voltage when Method C is used. Since, a voltage dip do not influence the rotor current for Method C, the rotor current is not shown. In the figure it can be seen that the maximum rotor voltage

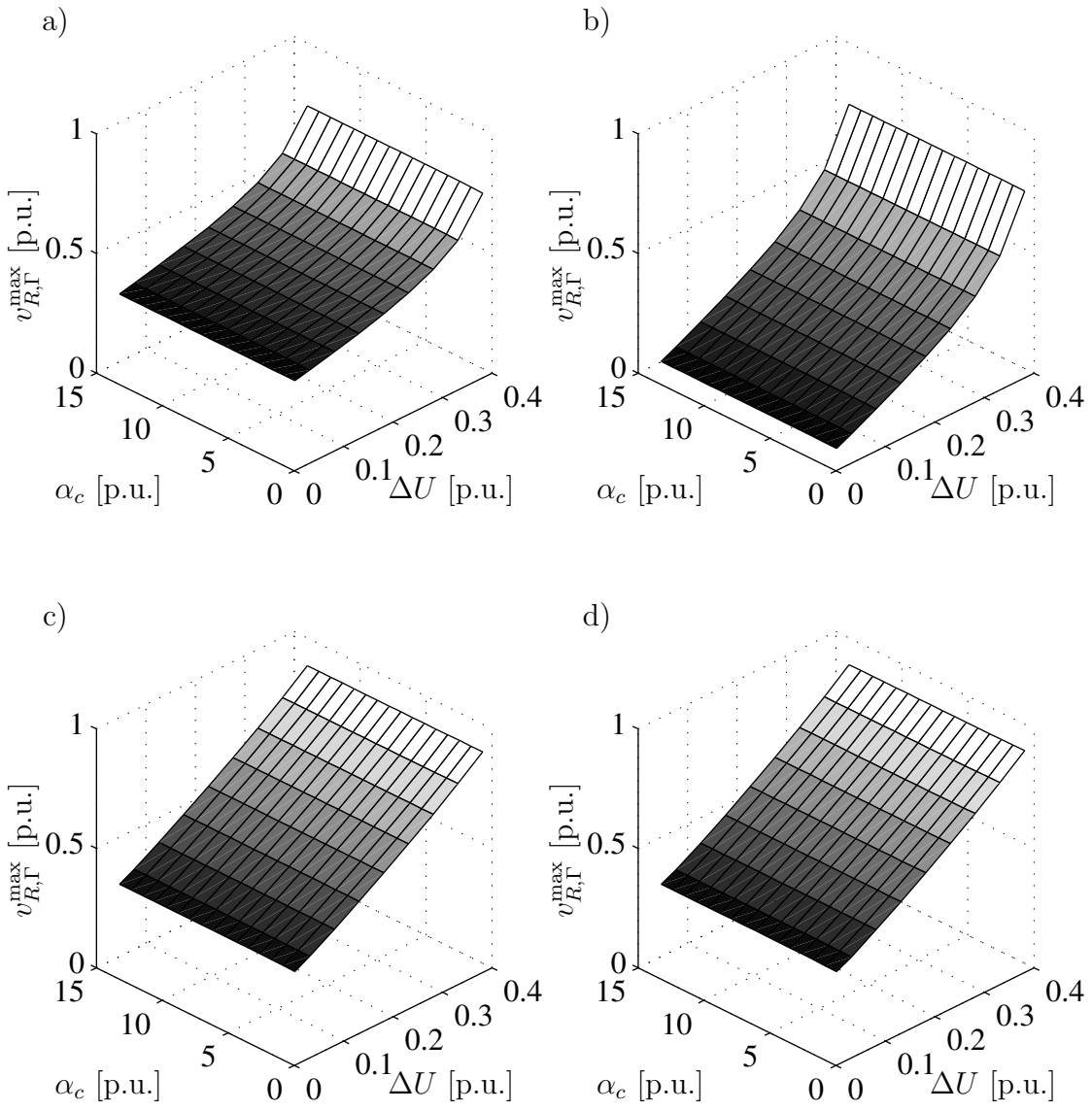

Figure 6.16: Maximum value of the rotor voltage, for Method C, after a voltage dip, and for different bandwidths of the current control loop, α_c. a) Case I. b) Case II. c) Case III. d) Case IV.

increases with the magnitude of the voltage dip, in a similar way as for Method B. The maximum rotor voltage, for large voltage dips, is similar between the different operating points investigated. It can also be seen that the maximum rotor voltage, due to a voltage dip, is independent of the bandwidth of the current control loop, α_c. Generally, the maximum rotor voltage for Method B is a couple percent lower than for Method C.

As could be seen in Figure 6.15 and Figure 6.16, for Cases I, II and IV the maximum rotor voltage is quite high even for a small voltage dip. The reason for this is that the rotor speed is either 0.7 p.u. or 1.3 p.u., i.e., the rotor voltage must be 0.3 p.u. in order to have a slip of 30 %. This is approximately the maximum needed rotor voltage in order control the doubly-fed induction machine with a maximum slip of ± 30 % (without considering grid disturbances). This means that if the inverter is designed according to the maximum desired slip, the rotor voltage is close to its maximum allowed value for Cases I, II and IV. Then, there is not "much" rotor voltage left to handle a grid disturbance, i.e., the rotor voltage must be limited and thereby the current controller loses control of the rotor currents.

It can also be noted, although not shown for all methods, that the maximum rotor current due to a voltage dip becomes quite similar for the different current control methods (A–C) when the bandwidth of the current control loop is high. The reason for this is that when the bandwidth of the current control loop increases, the need for feed-forward of the back emf vanishes, cf. the Bode plot in Figure 5.10.

If the doubly-fed induction machine was magnetized from the stator circuit instead of the rotor circuit, the maximum rotor voltage could be reduced from 0 up to 0.2 p.u. for Method C, depending on the size of the voltage dip, for the investigated system. Further, the "natural" damping of the system is also improved. The interested reader can find a small investigation of this in Appendix D.

Method C seems to be the best one suited to handle a voltage dip, since it has full control over the rotor currents, at least, as long as the rotor voltage is not limited. For Method C the flux oscillations is are worse damped than the other investigated methods. But, since we have full control of the rotor current, they can be used to damp out the flux oscillation.

6.4.3 With Flux Damping

Here, in this section, flux damping, as described in Section 6.2, will be introduced in the current control laws. In order to investigate the influence of the flux damping, on the rotor currents, the following current control laws will be used

Method D Method A with flux damping. Flux damping is performed according to Section 6.2.

Method E Method B with flux damping. Flux damping is performed according to Section 6.2.

Method F Method C with "active resistance" and with flux damping. Flux damping is performed according to Section 6.2.

Figure 6.17 shows a simulation of the response, for Methods D, E and F, caused by a voltage dip of 25 %. In the simulation, the doubly-fed induction machine is magnetized

from the rotor circuit, i.e., $i^{\text{ref}}_{Rd,\Gamma}$ is controlled according to (6.71). The bandwidth of the current control loop in the simulation was set to 7 p.u. and the flux damping, α_d, is set to 0.07 p.u. The response of the different methods performs almost the same, except

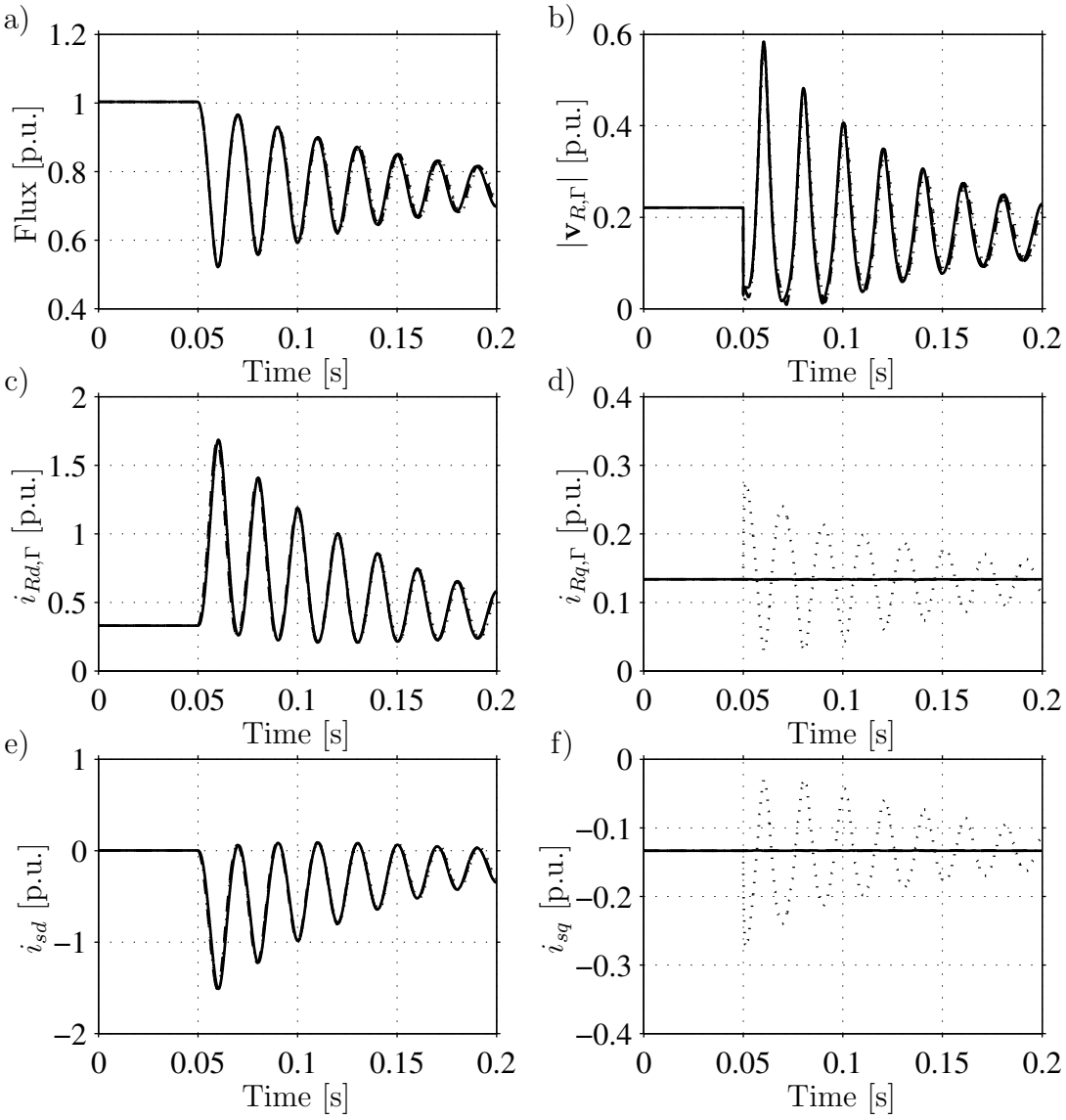

Figure 6.17: Responses due to a voltage dip, of 25 %, for current control Method D (dotted), Method E (dashed) and, Method F (solid). The doubly-fed induction machine is magnetized from the rotor circuit. The machine is running of 17 % of rated torque and at a rotor speed of 0.8 p.u. before the voltage dip. a) Flux, ψ_s. b) Rotor voltage, $|\mathbf{v}_{R,\Gamma}|$. c) d component rotor current, $i_{Rd,\Gamma}$. d) q component rotor current, $i_{Rq,\Gamma}$. e) d component stator current, i_{sd}. f) q component stator current, i_{sq}.

Method A which has oscillations in the q component of the rotor and stator current. These oscillations are caused by the back emf in the same way as described in previous section (without flux damping). It can be seen in the figure that the d components of the currents has large oscillations. The reason for the oscillations in the d component

of the rotor current is that it is used to damp out the oscillations. This method, with a flux differentiation to damp out the flux oscillations demands relatively high currents [37]. The maximum value of the rotor voltage is also relatively high. In comparison to the simulation in Figure 6.13, without flux damping, the maximum value of the rotor voltage is higher.

As could be seen in Figure 6.17 the maximum rotor current for the different methods are close to each other, therefore the response of the doubly-fed induction machine for different magnitude of the voltage dips will only be presented for Method F. Since the d component is used to damp out the flux oscillations, which therefore might be high, both the maximum rotor current and voltage will be shown. Figure 6.18 shows the maximum rotor current after a voltage dip for different bandwidths of the flux damping, α_d. The bandwidth of the current control loop is set to 7 p.u. and the doubly-fed induction machine is magnetized from the rotor circuit. In the figure it can be seen, that the rotor currents will reach a very high value for a relatively small voltage dip. It can also be seen that if the flux damping is increased the maximum value of the rotor current is also increased, especially when comparing to very low bandwidths of the flux damping, α_d. Of course, it is possible to limit the rotor current so it does not increase above the rated current of the inverter. If the rotor current has to be limited, the performance of the flux damping will be lower. Note, that the controller will not lose the control of the rotor currents as long as the rotor voltage is not limited. Therefore the maximum value of the rotor voltage is of great importance, if the system should withstand a voltage dip. Figure 6.19 shows the corresponding maximum rotor voltage, for Method F. In the figure it can be seen that the "needed" rotor voltage to damp the flux oscillations increases with the bandwidth of the flux damping, α_d, at least for larger voltage dips. The maximum rotor voltage is not that dependent on the bandwidth of the flux damping, α_d, for smaller voltage dips. It can also be noted that there exists a flux damping, α_d, where the maximum rotor voltage is minimum. However, the damping of the flux will be poor since the value of the flux damping, α_d, is small.

As for the case without flux damping it is possible to reduce the maximum rotor current and voltage if the doubly-fed induction machine is magnetized from the stator circuit instead of the rotor circuit. Further, the "natural" damping of the system is also improved. The interested reader can find a small investigation of this in Appendix D.

6.4.4 Conclusion and Discussion

It has been found out that in order to withstand a voltage dip, there are two important factors, namely the maximum allowed rotor current and voltage. For example, if the rotor voltage must be limited, then the current controller "loses" the control over the rotor currents and therefore the rotor currents might be larger than maximum allowed

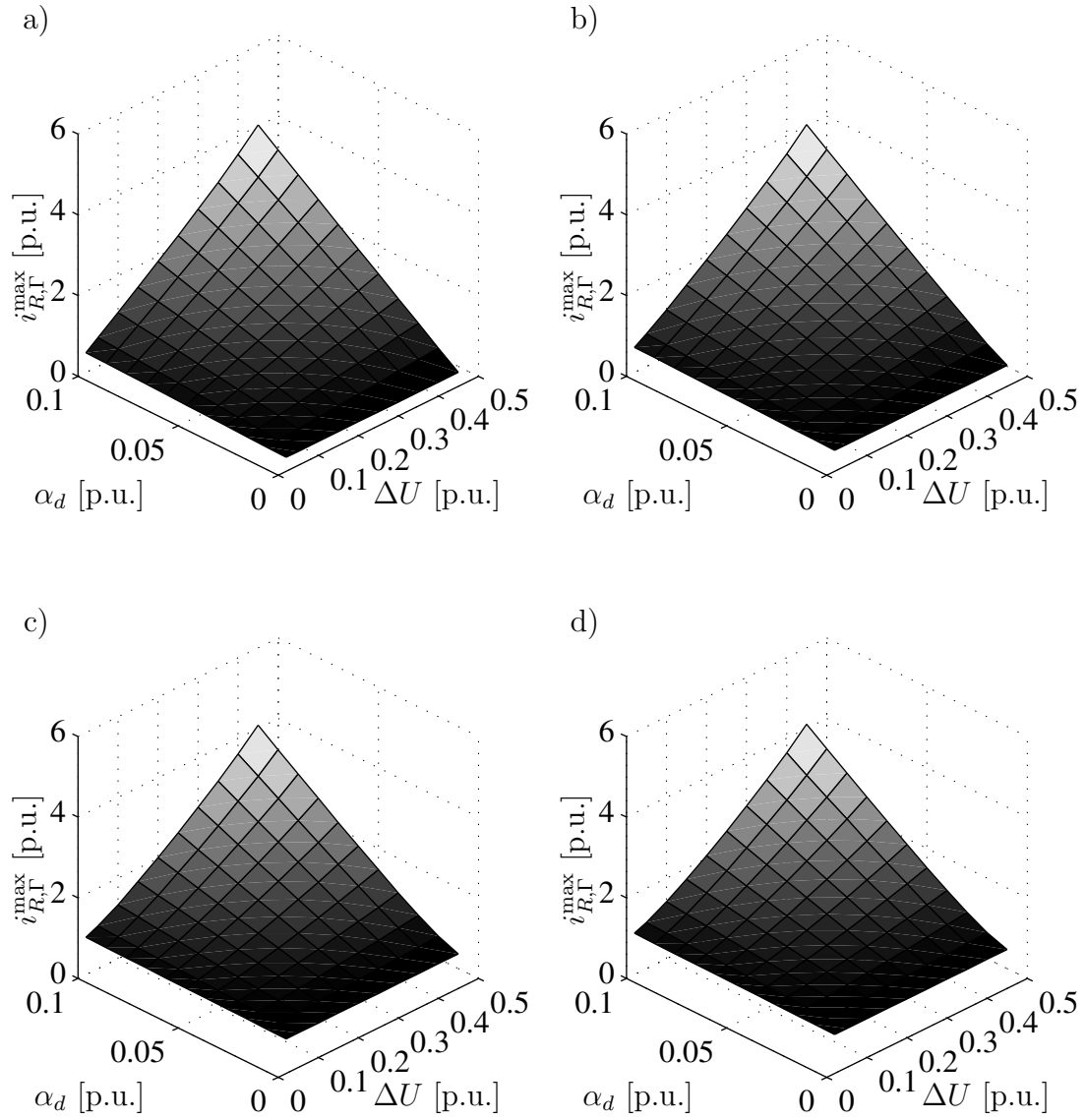

Figure 6.18: Maximum value of the rotor current, for current control Method F, after a voltage dip, and for different bandwidths of the current control loop, α_c. a) Case I. b) Case II. c) Case III. d) Case IV.

current. The choice of current control law can also be an important factor, if the bandwidth of the current control loop is low.

When flux damping is used, the rotor currents will reach their rated values for a relatively small voltage dip. However, the maximum rotor voltage is not affected as much as the rotor current. The difference between different methods of flux damping is small.

In the evaluation in this section, the control of the grid-side inverter has not been considered. Although, some interesting results can be noted. Which is, that it is not only necessary to dimension the inverter after the rated current of the machine and the

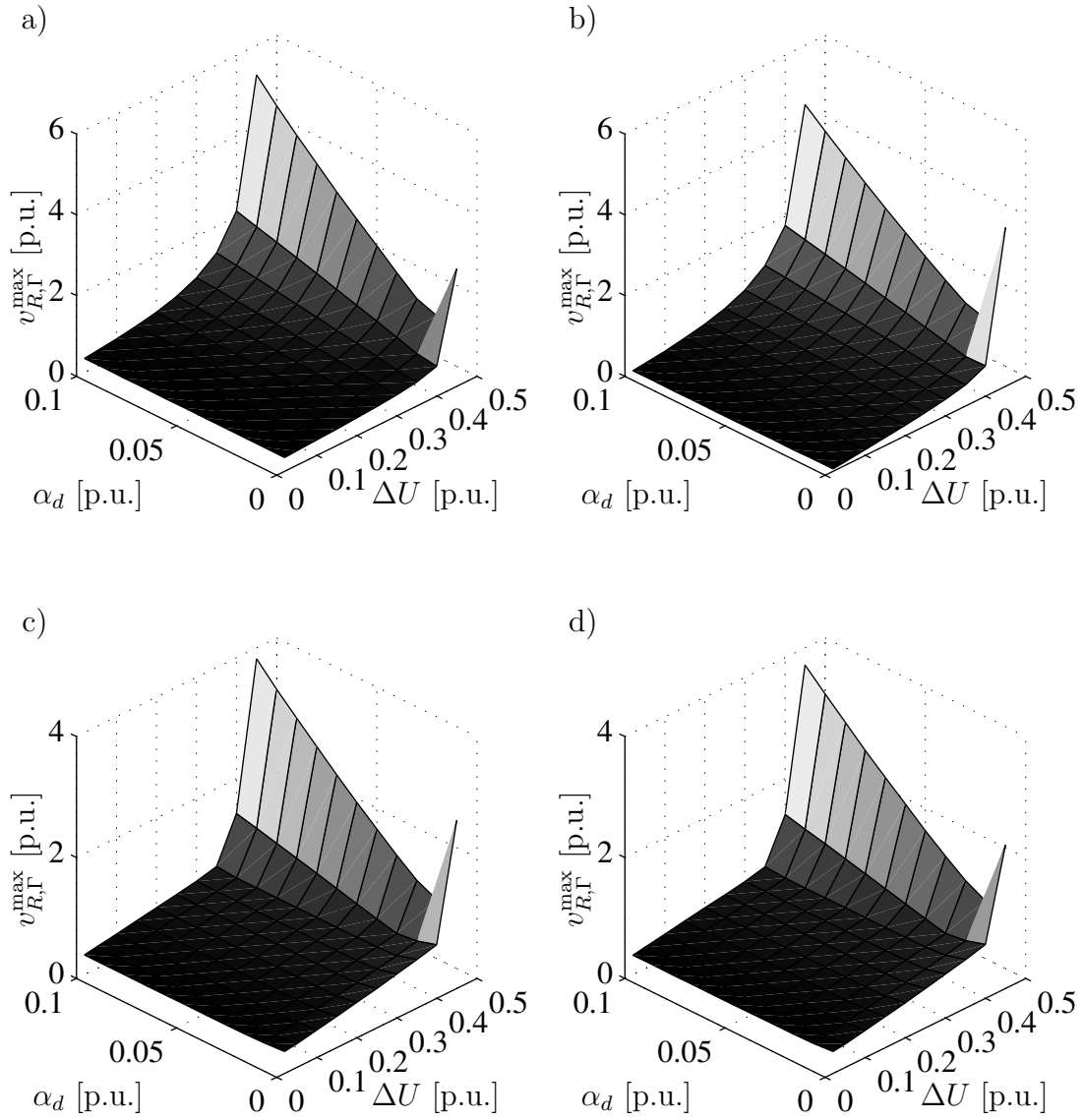

Figure 6.19: Maximum value of the rotor voltage, for current control Method F, after a voltage dip, and for different bandwidths of the current control loop, α_c. a) Case I. b) Case II. c) Case III. d) Case IV.

desired variable-speed range, but also so it can handle and damp out the flux oscillation of a specific voltage dip. If the doubly-fed induction machine is magnetized from the stator circuit instead of the rotor circuit the maximum rotor voltage and current, due to a voltage dip, can be reduced.

The method with feed-forward of the back emf and possibly an "active resistance" seems to be the best one suited to handle a voltage dip, since it has full control of the rotor currents. Using this method the flux oscillations are worse damped, but since the controller has full control of the rotor current, they can be used to damp out the flux oscillation. One disadvantage of using feed-forward of the back emf is that the stator

voltage and current have to be measured. This implies that offsets and noise in the measurements might influence the performance of the controller.

Chapter 7

Conclusion

The electrical energy efficiency of wind turbine systems equipped with doubly-fed induction generators in comparison to other wind turbine generator systems has been investigated. It was found that if the range of the variable speed is set properly, there is the possibility to gain a few percentage units (approximately 3 %) in energy efficiency compared to a variable-speed induction generator equipped with a full power inverter. In comparison to a direct-driven permanent-magnet synchronous generator, there might be a slight gain in the energy depending on the average wind-speed of the site. The stator-to-rotor turns ratio is an important design parameter for lowering the losses of the doubly-fed induction generator system. In comparison with the result obtained by Datta et al. in [9], there is a large difference in the gain in energy. Reasons for this might be that in [9], the electric and mechanical losses are neglected, the maximum power that can be produced of each turbine is different and that the result is only calculated with one simulated wind speed.

The flux dynamics of the doubly-fed induction machine consist of two poorly damped poles, which influence the current control loop. They will cause oscillations close to the line frequency in the flux and in the rotor currents. Different methods to reduce the influence of the flux oscillations in the rotor current have been investigated. The method with feed-forward compensation of the whole back emf manages to suppress the oscillations in the rotor currents. The method which only uses "active resistance" to damp out disturbances acting on the rotor current might be unstable, even though the method manages to suppress low-frequency disturbances very well, if the bandwidth of the current control loop is not set much higher than the back-emf dynamics. The method that combines the feed-forward compensation and the "active resistance" managed to suppress low-frequency disturbances and the oscillations caused by the flux very well. Further, it has been shown that, using this method, the analysis of the flux dynamics is reduced to a second-order system.

In case of a voltage dip, the flux in the doubly-fed induction machine will start to oscillate. It is then necessary that the controller can cope with the disturbance, since

otherwise the system must be disconnected from the grid. Important factors are the maximum allowed rotor current and voltage. Especially, if the rotor voltage must be limited, then the controller loses control of the rotor current, which then might be too high. Further, it has been found that the choice of current control law is of importance if the bandwidth of the current control loop is low.

When using flux damping, the rotor current will reach its rated value for a relatively small voltage dip. It has also been found out that the difference between different current control methods when using flux damping of the flux is small. There exists a value of the flux damping where the maximum rotor voltage is minimum. However, the damping of the flux will be poor since the value of the flux damping is small.

If the doubly-fed induction machine is magnetized from the stator circuit instead of the rotor circuit it is possible to reduce the maximum rotor current and voltage due to a voltage dip. The "natural" damping of the system is also improved, when the doubly-fed induction machine is magnetized from the stator.

The methods with feed-forward of the back emf and possibly an "active resistance" seems to be the best one suited, at least for low bandwiths of the current control loop, to handle a voltage dip, since it has full control of the rotor currents.

Chapter 8

Proposed Future Work

In this thesis the response of the doubly-fed induction generator to grid disturbances has been investigated. As always there are many more interesting aspect that can be considered, such as; unsymmetrical voltage dips, voltage harmonics, phase shifts and frequency dips in the grid voltage.

Means to counteract these disturbances could be improvements of the control laws as well as using the grid-side inverter, connected either in shunt or series to the grid, to improve the situation.

Other aspects that could be of interest is to use the wind turbine, equipped with a doubly-fed induction generator, to support the electrical grid statically or dynamically. Since the machine-side inverter is connected in shunt to the grid via the doubly-fed induction machine (which acts as a transformer) and if the grid-side inverter is connected in series with the grid, the system is close to a unified power quality conditioner (UPQC) [18]. Therefore an interesting aspect is to investigate the possibility to run the wind turbine equipped with a doubly-fed induction generator as a UPQC. The great advantage is that with little additional cost, the wind turbine also works as an UPQC, which most certainly increase the value of the wind turbine.

References

[1] F. Abrahamsen. *Energy Optimal Control of Induction Motor Drives*. Ph.D. Thesis, Aalborg University, 2000.

[2] T. Ackermann and L. Söder. An overview of wind energy-status 2002. *Renewable and Sustainable Energy Reviews*, 6(1-2):67–127, 2002.

[3] I. Boldea and S. A. Nasar. *Electric Drives*. CRC Press LCC, 1999.

[4] T. Burton, D. Sharpe, N. Jenkins, and E. Bossanyi. *Wind Energy Handbook*. John Wiley & Sons, Ltd, 2001.

[5] O. Carlson, J. Hylander and K. Thorborg. Survey of variable speed operation of wind turbines. In *1996 European Union Wind Energy Conference*, pp. 406–409. 20–24 May, 1996, Göteborg, Sweden.

[6] L. Congwei, W. Haiqing, S. Xudong, and L. Fahai. Research of stability of double fed induction motor vector control system. In *ICEMS 2001. Proceedings of the Fifth International Conference on Electrical Machines and Systems*, pp. 1203–6 vol. 2, 2001.

[7] R. L. Cosgriff. *Nonlinear Control Systems*. McGraw-Hill, 1958.

[8] R. Datta and V. T. Ranganathan. Decoupled control of active and reactive power for a grid-connected doubly-fed wound rotor induction machine without position sensors. In *Conference Record of the 1999 IEEE Industry Applications Conference. Thirty-Fourth IAS Annual Meeting (Cat. No.99CH36370)*, pp. 2623–2628.

[9] R. Datta and V. T. Ranganathan. Variable-speed wind power generation using doubly fed wound rotor induction machine-a comparison with alternative schemes. *IEEE Transactions on Energy Conversion*, 17(3):414–21, Sept. 2002.

[10] R. Datta and V.T. Ranganathan. A simple position-sensorless algorithm for rotor-side field-oriented control of wound-rotor induction machine. *IEEE Transactions on Industrial Electronics*, 48(4):786–93, Aug. 2001.

[11] F. B. del Blanco, M. W. Degner, and R. D. Lorenz. Dynamic analysis of current regulators for ac motors using complex vectors. *IEEE Transactions on Industry Applications*, 35(6):1424–1432, 1999.

[12] DeWind. D8 Series. Brochure. www.dewind.de.

[13] Elforsk. Driftuppföljning av vindkraftverk. www.elforsk.se/varme/varm-vind.html, December 2002. (in Swedish).

[14] www.enercon.de.

[15] Energimyndigheten. Climate report 2001. Technical Report ER 6:2002, Swedish National Energy Agency, www.stem.se, 2002. ISSN 1403-1892.

[16] Energimyndigheten. Elmarknad 2002. Technical Report ET 9:2002, Swedish National Energy Agency, www.stem.se, May 2002. (in Swedish).

[17] Energimyndigheten. Energiförsörjningen i Sverige. Technical Report ER 20:2002, Swedish National Energy Agency, www.stem.se, 2002. (in Swedish).

[18] H. Fujita and H. Akagi. The unified power quality conditioner: the integration of series- and shunt-active filters. *IEEE Transactions on Power Electronics*, 13(2):315–322, 1998.

[19] www.gewindenergy.com.

[20] T. Glad and L. Ljung. *Reglerteori: flervariabla och olinjära metoder*. Studentlitteratur, Lund, 1997. (in Swedish).

[21] A. Grauers. *Synchronous Generator and Frequency Converter in Wind Turbine Applications: System Design and Efficiency*. Licentiate Thesis, Chalmers University of Technology, 1994.

[22] A. Grauers. *Design of Direct-Driven Permanent-Magnet Generators for Wind Turbines*. Ph.D. Thesis, Chalmers University of Technology, 1996.

[23] L. H. Hansen, L. Helle, F. Blaabjerg, E. Ritchie, S. Munk-Nielsen, H. Bindner, P. Sørensen, and Bak-Jensen B. Conceptual survey of generators and power electronics for wind turbines. Technical Report Risø-R-1205(EN), Risø National Laboratory, Roskilde, Denmark, December 2001. ISBN 87-550-2743-8.

[24] L. Harnefors. *On Analysis, Control and Estimation of Variable-Speed Drives*. Ph.D. Thesis, Royal Institute of Technology, 1997.

[25] L. Harnefors. *Control of Variable-Speed Drives*. Applied Signal Processing and Control, Department of Electronics, Mälardalen University, Västerås, Sweden, 2002.

[26] L. Harnefors and H.-P. Nee. Model-based current control of ac machines using the internal model control method. *IEEE Transactions on Industry Applications*, 34(1):133–141, 1998.

[27] L. Harnefors and H.-P. Nee. A general algorithm for speed and position estimation of ac motors. *IEEE Transactions on Industrial Electronics*, 47(1):77–83, 2000. Copyright 2000, IEE.

[28] L. Harnefors, K. Pietiläinen, and L. Gertmar. Torque-maximizing field-weakening control: design, analysis, and parameter selection. *IEEE Transactions on Industrial Electronics*, 48(1):161–168, 2001.

[29] M. Heller and W. Schumacher. Stability analysis of doubly-fed induction machines in stator flux reference frame. In *Proceedings of 7th European Conference on Power Electronics and Applications*, pp. 707–710 vol.2, Brussels, Belgium, 1997. EPE Assoc.

[30] K. Hentabli, M. E. H. Benbouzid, and D. Pinchon. CGPC with internal model structure: Application to induction motor control. In *Proceedings of the 1997 IEEE International Conference on Control Applications*, IEEE Conference on Control Applications – Proceedings, pp. 235–237, Hartford Ct USA, 1997. IEEE Piscataway NJ USA. 9 Refs. IEEE.

[31] B. Hopfensperger and D. Atkinson. Doubly-fed a.c. machines: classification and comparsion. In *European Conference on Power Electronics and Applications (EPE)*, Graz, 2001.

[32] B. Hopfensperger, D. Atkinson, and R. A. Lakin. Stator flux oriented control of a cascaded doubly-fed induction machine. *IEE Proceedings: Electric Power Applications*, 146(6):597–605, 1999.

[33] B. Hopfensperger, D. J. Atkinson, and R. A. Lakin. Stator-flux-oriented control of a doubly-fed induction machine with and without position encoder. *IEE Proceedings Electric Power Applications*, 147(4):241–50, 2000.

[34] www.hornsrev.dk.

[35] M. G. Ioannides and J. A. Tegopoulos. Optimal efficiency slip-power recovery drive. *IEEE Transactions on Energy Conversion*, 3(2):342–8, 1988.

[36] G. L. Johnson. *Wind Energy Systems*. Prentice-Hall, Englewood Cliffs, New Jersey, 1985.

[37] C. R. Kelber. *Aktive Dämpfung der doppelt-gespeisten Dhrestrommaschine*. Ph.D. Thesis, Technishen Universität Carolo-Wilhelmina, 2000.

[38] C. R. Kelber and W. Schumacher. Active damping of flux oscillations in doubly-fed ac machines using dynamic variation of the system's structure. In *European Conference on Power Electronics and Applications (EPE)*, Graz, 2001.

[39] E. H. Kim, S. B. Oh, Y. H. Kim, and C. H. Kim. Power control of a doubly fed induction machine without rotational transducers. In *Proceedings of 3rd International Conference on Power Electronics and Motion Control. vol.2. 15 18 Aug. 2000*, Proceedings IPEMC 2000. Third International Power Electronics and Motion Control Conference (IEEE Cat. No.00EX435). Int. Acad, pp. 951–955, Beijing, China, 2000. Publishers Beijing China. China Electrotech. Soc. (CES); Nat. Natural Sci. Found. China (NSFC) Copyright 2001, IEE.

[40] P. K. Kovács. *Transient Phenomena in Electrical Machines*. Elsevier, 1984.

[41] Å. Larsson, P. Sørensen, and F. Santjer. Grid impact of variable speed wind turbines. In *European Wind Energy Conference and Exhibition (EWEC 99)*, Nice, France, 1999.

[42] W. Leonhard. *Control of Electrical Drives*. Springer-Verlag, 2nd Edition, 1996.

[43] M. Liwschitz-Garik and C. Whipple. *Electric Machinery*, volume II. D. van Nostrand Company, Inc., New York, 1946.

[44] L. Morel, H. Godfroid, A. Mirzaian, and J. M. Kauffmann. Double-fed induction machine: converter optimisation and field oriented control without position sensor. *IEE Proceedings Electric Power Applications*, 145(4):360–8, 1998.

[45] P. Mutschler and R. Hoffmann. Comparison of wind turbines regarding their energy generation. In *2002 IEEE 33rd Annual Power Electronics Specialists Conference (PESC)*, pp. 6–11. 23–27 Jun. 2002, Cairns, Australia.

[46] Nordex. N80/2500 kW N90/2300 kW. Brochure. www.nordex-online.com.

[47] R. Ottersten. *Vector Control of a Double-Sided PWM Converter and Induction Machine Drive*. Lic. Thesis, Chalmers University of Technology, 2000.

[48] M. P. Papadopoulos, S. A. Papathanassiou, N. G. Boulaxis, and S. T. Tentzerakis. Voltage quality change by grid-connected wind turbines. In *European Wind Energy Conference*, pp. 783–785, Nice, France, 1999.

[49] R. Pena, J. C. Clare, and G. M. Asher. Doubly fed induction generator using back-to-back pwm converters and its application to variable-speed wind-energy generation. *IEE Proceedings-Electric Power Applications*, 143(3):231–41, May 1996.

[50] S. Peresada, A. Tilli, and A. Tonielli. Robust output feedback control of a doubly-fed induction machine. In *IECON'99. Conference Proceedings. 25th Annual Conference of the IEEE Industrial Electronics Society (Cat. No.99CH37029)*, pp. 1348–1354.

[51] A. Petersson and S. Lundberg. Energy efficiency comparsion of electrical systems for wind turbines. In *2002 IEEE Nordic Workshop on Power and Industrial Electronics (NORpie/2002)*, Stockholm, Sweden, 2002.

[52] T. Petru and T. Thiringer. Active flicker reduction from a sea-based 2.5 MW wind park connected to a weak grid. In *2000 IEEE Nordic Workshop on Power and Industrial Electronics (NORpie/2000)*, pp. 7–11, Aalborg, Denmark, 2000.

[53] B. Rabelo and W. Hofmann. Optimal active and reactive power control with the doubly-fed induction generator in the MW-class wind-turbines. *Proceedings of International Conference on Power Electronics and Drives Systems (PEDS)*, pp. 53–8 vol.1, 2001.

[54] R. Richter. *Electrische Machinen*, Volume 4. Verlag Birkhäuser, Basel/Stuttgart, 1954.

[55] B. Schmidtbauer. *Analog och digital reglerteknik*. Studentlitteratur, Lund, 2nd edition, 1995. (in Swedish).

[56] Semikron. SKiiP 1203GB122-2DW. Data sheet, March 2001.

[57] Semikron. SKiiP 2403GB122-4DL. Data sheet, March 2001.

[58] Semikron. SKiiP 603GD122-3DUW. Data sheet, March 2001.

[59] G. R. Slemon. Modelling of induction machines for electric drives. *IEEE Transactions on Industry Applications*, 25(6):1126–31, 1989.

[60] J.-J. E. Slotline and W. Li. *Applied Nonlinear Control*. Prentice-Hall, Upper Saddle River, New Jersey, USA, 1991.

[61] D. A. Spera. *Wind Turbine Technology*. ASME, New York, 1994.

[62] K. J. Åström and B. Wittenmark. *Adaptive Control*. Addison-Wesley, 2nd Edition, 1995.

[63] Y. Tang and L. Xu. Flexible active and reactive power control strategy for a variable speed constant frequency generating system. *IEEE Transactions on Power Electronics*, 10(4):472–478, 1995.

[64] T. Thiringer and J. Linders. Control by variable rotor speed of a fixed-pitch wind turbine operating in a wide speed range. *IEEE Transactions on Energy Conversion*, 8(3):520–526, Sept. 1993.

[65] T. Thiringer and J. Luomi. Comparison of reduced-order dynamic models of induction machines. *IEEE Transactions on Power Systems*, 16(1):119–26, Feb. 2001.

[66] J. L. Thomas and M. Boidin. An internal model control structure in field oriented controlled vsi induction motors. In *EPE '91. 4th European Conference on Power Electronics and Applications*, pp. 202–7 vol.2, 1991.

[67] K. Thorborg. *Power Electronics – in Theory and Practice.* Studentlitteratur, Lund, 1993.

[68] R. Ueda, T. Sonoda, K. Koga, and M. Ichikawa. Stability analysis in induction motor driven by v/f controlled general-purpose inverter. *IEEE Transactions on Industry Applications*, 28(2):472–481, 1992.

[69] P. S. Veers. Three-dimensional wind simulation. Technical Report SAND88-0152, Sandia National Laboratories, Albuquerque, New Mexico, March 1998.

[70] Vestas. V52-850 kW. Brochure. www.vestas.com.

[71] A. K. Wallace, R. Spee, and G. C. Alexander. The brushless doubly-fed machine: its advantages, applications and design methods. In *Sixth International Conference on Electrical Machines and Drives (Conf. Publ. No.376)*, pp. 511–517. IEE London UK, 1993. 8–10 Sept. 1993; Oxford, UK.

[72] S. Wang and Y. Ding. Stability analysis of field oriented doubly-fed induction machine drive based on computer simulation. *Electric Machines and Power Systems*, 21(1):11–24, 1993.

[73] A. Williamson, A. C. Ferreira, and A. K. Wallace. Generalised theory of the brushless doubly-fed machine. Part 1: Analysis. *IEE Proc.–Electr. Power Appl.*, 144(2):111–122, March 1997.

[74] D. Winkelaar. Fast three-dimensional wind simulation and prediction of stochastic blade loads. In *10th ASME Wind Energy Symposium*, 1991.

[75] L. Xu, F. Liang, and T. A. Lipo. Transient model of a doubly excited reluctance motor. *IEEE Transactions on Energy Conversion*, 6(1):126–133, 1991.

[76] L. Xu and C. Wei. Torque and reactive power control of a doubly fed induction machine by position sensorless scheme. *IEEE Transactions on Industry Applications*, 31(3):636–42, 1995. Copyright 1995, IEE.

[77] D. S. Zinger and E. Muljadi. Annualized wind energy improvement using variable speeds. *IEEE Transactions on Industry Applications*, 33(6):1444–1447, 1997.

[78] D. Zhou and R. Spee. Field oriented control development for brushless doubly-fed machines. In *IAS '96. Conference Record of the 1996 IEEE Industry Applications Conference Thirty-First IAS Annual Meeting*, pp. 304–310 vol.1, 1996.

Appendix A

Nomenclature

Symbols

F_D	drag force
F_L	lift force
$\mathbf{I}$, I	current (steady state)
$\mathbf{i}$, i	current
k_i	integral gain
k_p	proportional gain
L	inductance
n_p	number of pole-pairs
P	active power
p	derivative operator
Q	reactive power
R	resistance
S	apparent power
$\mathbf{V}$, V	voltage (steady state)
$\mathbf{v}$, v	voltage
α	closed loop bandwidth
$\mathbf{\Psi}$, ψ	flux
ω_1	synchronous frequency
ω_2	slip frequency
ω_r	rotor angular speed (referred to the electrical system)

Superscripts

r	rotor oriented reference frame
ref	reference
s	stator oriented reference frame

Subscripts

d	real part of flux an oriented reference frame
r	rotor
m	mutual
M	mutual (Γ-representation)
R	rotor (Γ-representation)
s	stator
q	imaginary part of an flux oriented reference frame
λ	leakage
Γ	Γ-representation of Park-model
σ	leakage (Γ-representation)

Abbreviations

DFIG	doubly-fed induction generator
DFIM	doubly-fed induction machine
EMF	electro motive force
FSIG	fixed-speed induction generator
GSI	grid side inverter
IG	induction generator
IM	induction machine
IMC	internal model control
MSI	machine side inverter
PWM	pulse width modulation
SG	synchronous generator

Appendix B

Per-Unit Values

Table B.1: Base value definition.

Base value	Denomination	Definition
Base voltage	V_{base}	$V_n = \frac{V_{n,p-p}}{\sqrt{3}}$
Base current	I_{base}	I_n
Base impedance	Z_{base}	$\frac{V_{base}}{I_{base}}$
Base power	S_{base}	$3V_{base}I_{base}$
Base angular frequency	ω_{base}	$\omega_n = 2\pi f_n$
Base angular time	t_{base}	$\frac{1}{\omega_n}$
Base torque	T_{base}	$\frac{3V_{base}I_{base}}{\omega_{base}/n_p}$
Base flux	Ψ_{base}	$\frac{V_{base}}{\omega_{base}}$
Base inertia	J_{base}	$\frac{3V_{base}I_{base}}{\omega_{base}^3/n_p}$

The reason for choosing the phase voltage as base value instead of the main voltage is due to the fact that the p.u. values should be valid both for space vectors and for the jω-method.

Appendix C

Laboratory Setup and Induction Machine Data

C.1 Laboratory Setup

The laboratory setup consists of one slip-ringed wound rotor induction machine, one voltage source inverter, two measurement boxes, one digital signal processing (DSP) system and one measurement computer. Data of the induction machine is given in Section C.2. In Figure C.1 shows a principle sketch of the laboratory setup. The mea-

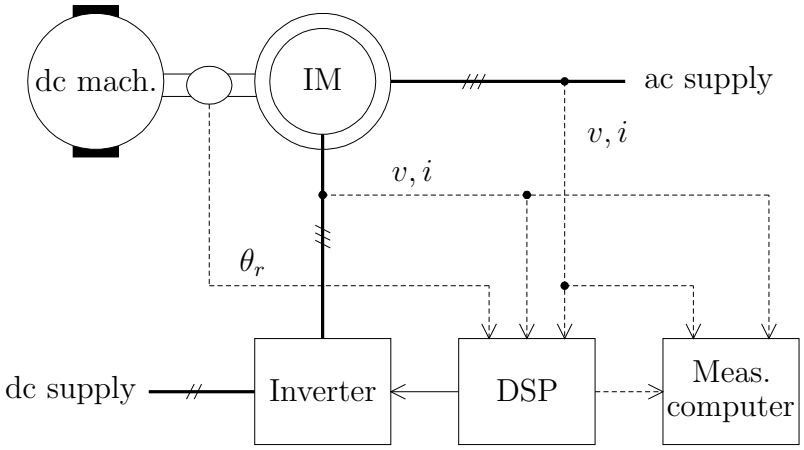

Figure C.1: Laboratory setup. Thick lines indicates cables with power while dashed lines implies measurements signals.

surement boxes measures voltages and currents. One measurement box is attached to the stator circuit while the other measure the rotor circuit. There is also a resolver that measure the rotor position, θ_r, of the induction machine. When running the machine as doubly-fed the stator circuit is directly connected to the grid (during the experiments in this thesis the stator circuit was connected to a 230-V, 50-Hz source, note that the nominal voltage of the induction machine is 380 V). Normally, the inverter operates as a back-to-back inverter, but during the experiments the inverter was directly fed by a

dc source of 450 V dc. Although the inverter here is fed directly from a dc source, it is possible to run it as a back-to-back inverter. The loading dc machine is fed through a thyristor inverter and could be both speed or torque controlled.

The control laws were all written in the C-language and downloaded to the DSP-unit (Texas TMS320c30). The DSP-unit has 16 analog input channels, for measurement signals, and 8 analog output channels, for signals that is desired to be fed to the measurement computer. The voltage references to the inverter are modulated digitally and via optic fibers sent to the inverter.

The measurement system consists of one filter box and one computer equipped with the LabView software. With this system it is possible to measure up to 16 channels, i.e., from the measurements boxes or from the DSP unit.

A more thorough description of the laboratory set up can be found in [47].

C.2 Data of the Induction Machine

Table C.1: Nominal values of the induction machine.

Rated voltage (Y)	$V_{n,p-p}$	380 V
Rated current	I_n	44 A
Rated frequency	f_n	50 Hz
Rated rotor speed	n_n	1440 rpm
Rated power	P_n	22 kW
Rated torque	T_n	145 Nm
Power factor		0.89

Table C.2: Parameters of the induction machine.

Stator resistance	R_s	0.115 Ω	⇔	0.0230 p.u.
Rotor resistance	R_r	0.184 Ω	⇔	0.0369 p.u.
Stator leakage inductance	$L_{s\lambda}$	1.65 mH	⇔	0.104 p.u.
Rotor leakage inductance	$L_{r\lambda}$	1.68 mH	⇔	0.106 p.u.
Magnitizing resistance	R_m	224 Ω	⇔	44.9 p.u.
Magnitizing inductance	L_m	46.6 mH	⇔	2.93 p.u.
Inertia	J	0.334 kgm^2	⇔	178 p.u.

Appendix D

Grid Disturbances — Difference Between Magnetizing from Rotor and Stator Circuit

In Section 6.4 it is assumed that the doubly-fed induction machine is magnetized from the rotor circuit. Here a small investigation of the difference in the maximum rotor current and voltage if the doubly-fed induction machine is magnetized from the stator circuit instead. For a description of the system and other details see Section 6.4.

When the doubly-fed induction machine is magnetized from the stator circuit the d component of the rotor current reference value is set to

$$i_{Rd,\Gamma}^{\text{ref}} = 0. \tag{D.1}$$

The torque is still controlled as described in Section 6.4.

D.1 Without Flux Damping

Figure D.1 shows the difference between the maximum rotor voltage, after a voltage dip, when the doubly-fed induction machine is magnetized from the rotor and the stator circuit. In the figure Method C is used. It can be seen that if the doubly-fed

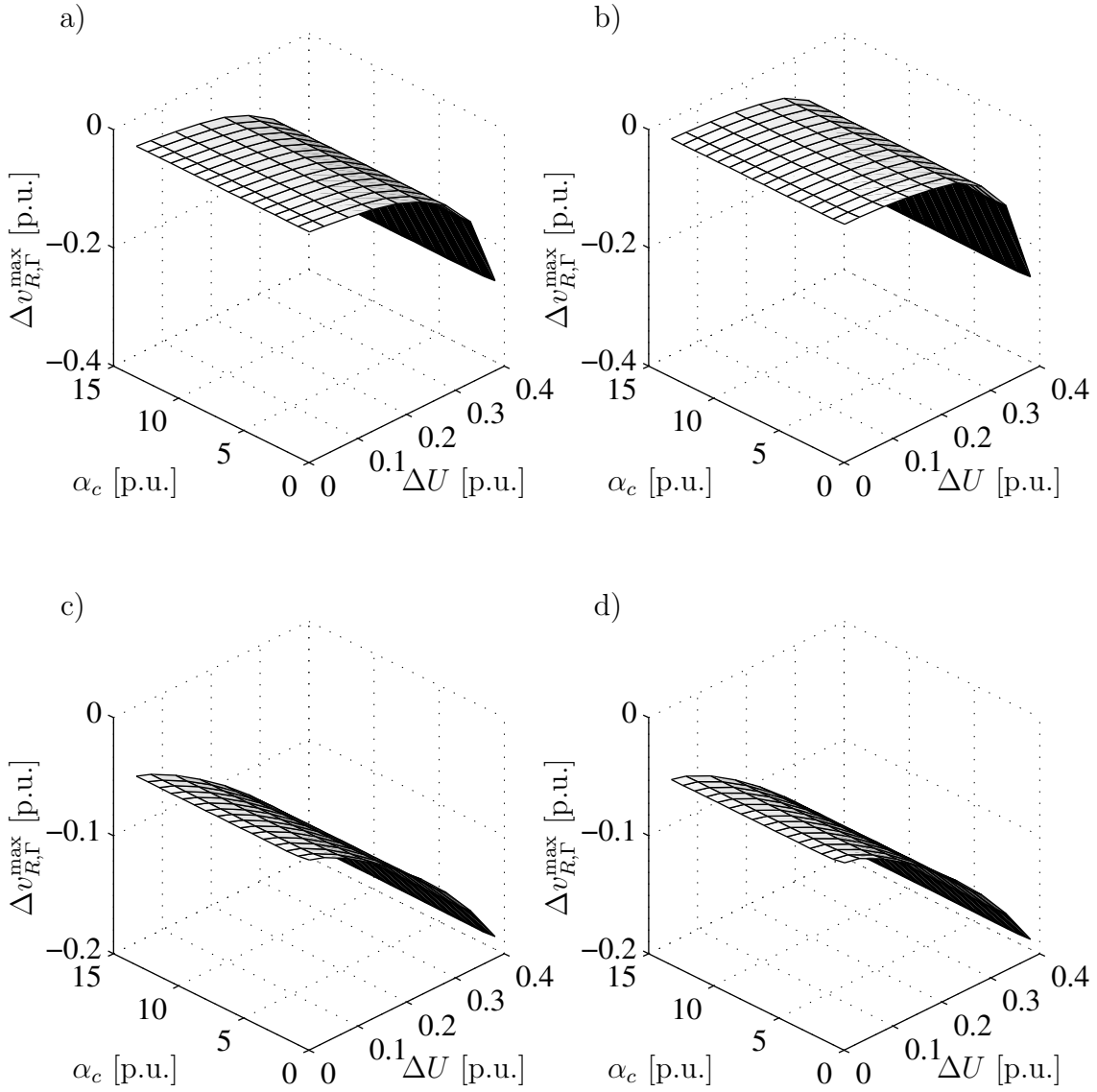

Figure D.1: Difference between the maximum value of the rotor voltage, after a voltage dip, when the doubly-fed induction machine is magnetized from the rotor and the stator circuit. Method C is used. a) Case I. b) Case II. c) Case III. d) Case IV.

induction machine is magnetized from the stator circuit, the maximum rotor voltage can be decreased with up to 0.2 p.u., depending on the size of the voltage dip. The "natural" damping of the system is also improved when the machine is magnetized from the stator circuit, i.e., $i_{Rd,\Gamma}^{\text{ref}} = 0$, cf. (5.59).

D.2 With Flux Damping

The difference between the maximum rotor voltage, due to a voltage dip, when the machine is magnetized from the rotor and the stator circuit, can be seen in Figure D.2. In the figure Method F is used. As shown in the figure the maximum rotor voltage,

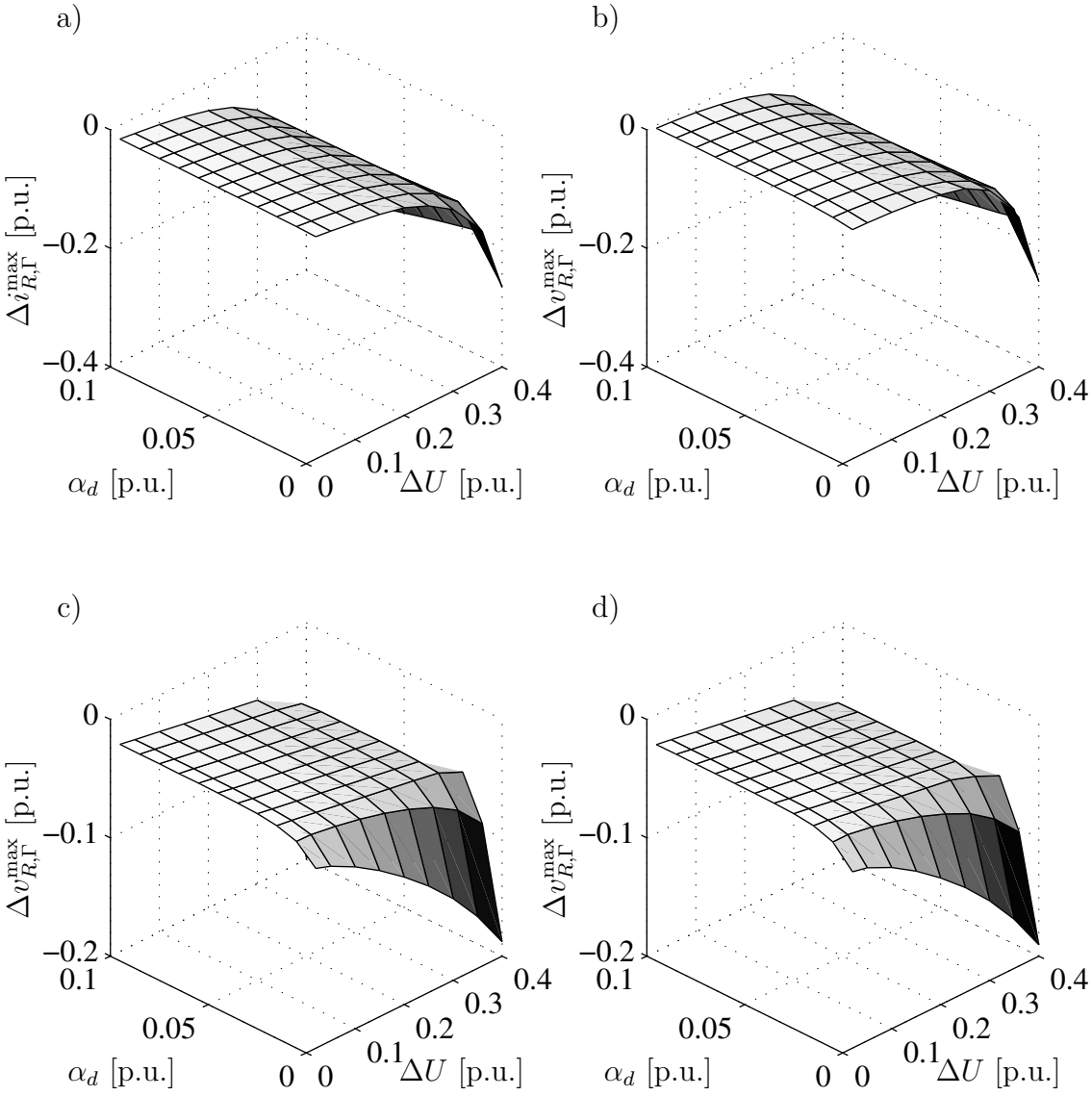

Figure D.2: Difference between the maximum value of the rotor voltage, after a voltage dip, when the doubly-fed induction machine is magnetized from the rotor and the stator circuit. Method F is used. a) Case I. b) Case II. c) Case III. d) Case IV.

due to a voltage dip, will decrease if the doubly-fed induction machine is magnetized from the stator circuit instead of the rotor circuit. Especially for large voltage dips.

The corresponding difference in the maximum rotor current, due to a voltage dip, is presented in Figure D.3. In the figure it can be seen that the maximum rotor current has significantly decreased when the machine is magnetized from the stator circuit instead of the rotor circuit. It can also be noted that when magnetizing from

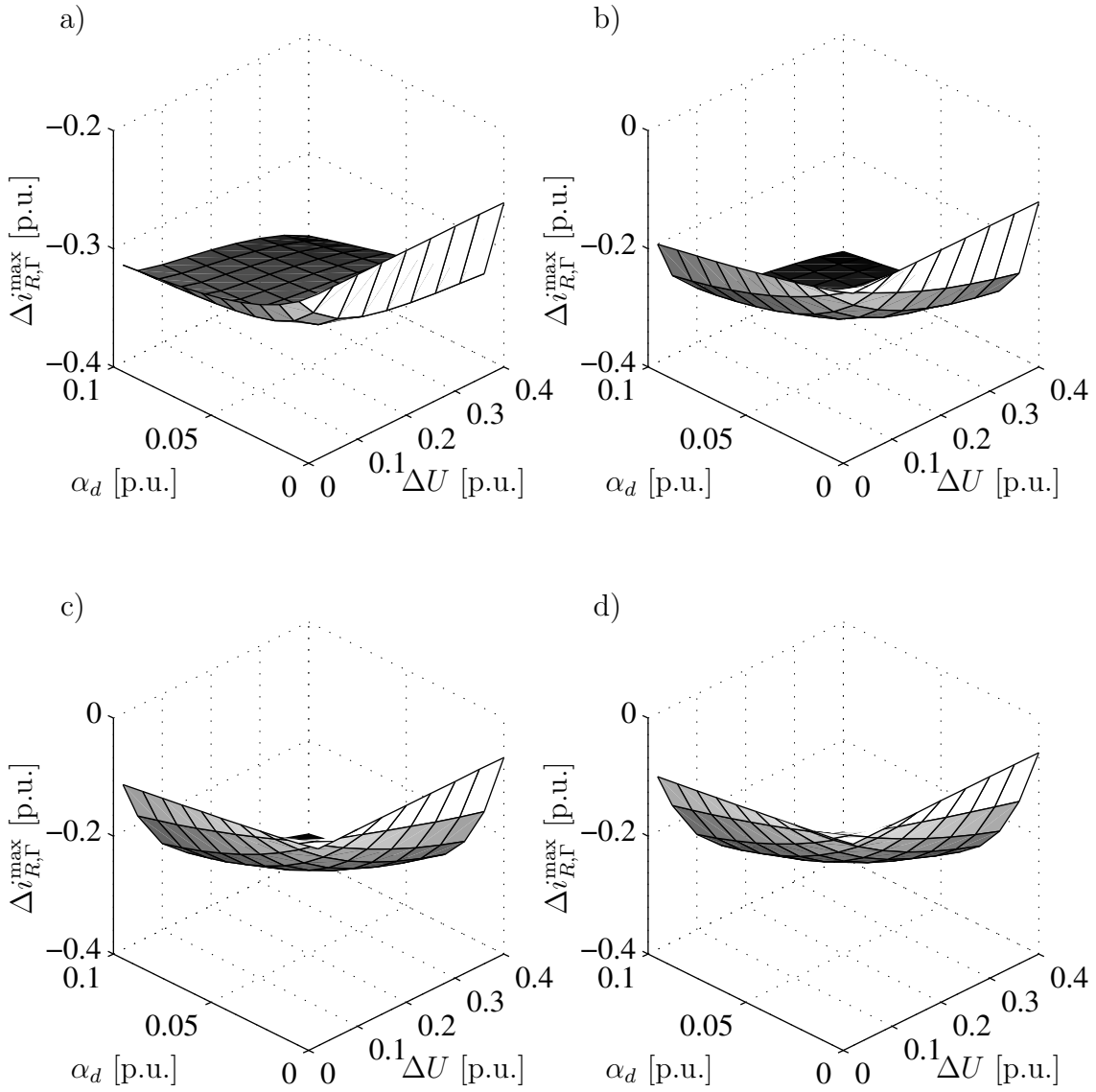

Figure D.3: Difference between the maximum value of the rotor current, after a voltage dip, when the doubly-fed induction machine is magnetized from the rotor and the stator circuit. Method F is used. a) Case I. b) Case II. c) Case III. d) Case IV.

the stator circuit, i.e., $i_{Rd,\Gamma}^{\text{ref}} = 0$, the "natural" damping of the system is improved, cf. (5.59).